الجمهورية الجزائرية الديمقراطية الشعبية
République Algérienne Démocratique et Populaire
وزارة التعليم العالي والبحث العلمي
Ministère de l'Enseignement Supérieur et de la Recherche Scientifique
جامعة فرحات عباس–سطيف1
Université Ferhat Abbas Sétif 1

THESE

Présentée à l'Institut d'Optique et Mécanique de Précision
Pour l'obtention du Diplôme de

DOCTORAT 3ème Cycle LMD

Spécialité: Optique et Photonique Appliquée

Par

Sara MAROUF

THEME

Propriétés Optiques des Nanostructures d'Oxyde de Zinc (ZnO)

Soutenu le : ///2017

Devant le jury composé de:

Mr. Smail Djabi	Prof.	Université de Sétif 1	Président
Mr. Abdelkrim Beniaiche	Prof.	Université de Sétif 1	Rapporteur
Mr. Nadir Bouarissa	Prof.	Univerite de M'sila	Examinateur
Mr. Abdelkader Nouiri	Prof.	Université d'O.E. Bouagui	Examinateur

الجمهورية الجزائرية الديمقراطية الشعبية
People’s Democratic Republic of Algeria
وزارة التعليم العالي والبحث العلمي
Ministry of Higher Education and Scientific Research
جامعة فرحات عباس–سطيف1
Ferhat Abbas-Setif1 University

THESIS

Submitted to the Institute of Optics and Precision Mechanics
in partial fulfillment of the requirements for the award of the Degree of

3rd CYCLE LMD DOCTORATE

Option: Optics and Applied Photonics

By

Sara MAROUF

Subject

Optical Properties of Zinc Oxide (ZnO) Nanostructures

Submited: ///2017

Members of the assessment committee:

Mr. Smail Djabi	Prof.	Setif 1 University	President
Mr. Abdelkrim Beniaiche	Prof.	Setif 1 University	Supervisor
Mr. Nadir Bouarissa	Prof.	M’sila University	Examiner
Mr. Abdelkader Nouiri	Prof.	O.E. Bouagui University	Examiner

To my beloved parents

Acknowledgements

This dissertation arose in part out of years of research that has been done. By that time, I have worked with many people whose contribution in different ways to the making of the thesis deserves special mention and sincere thanks. This is a wonderful opportunity for me to convey my gratitude to everyone helped me reach this point and complete my doctoral degree. Truly, words are not enough to express my thankfulness to all of them.

I greatly thank our Almighty Creator for being with me in every moment giving me the strength to overcome all the obstacles and for opening my mind to pursue this study. Without his blessing, it would not have been possible to complete this endeavor.

First of all, I would like to express my deepest appreciation to my supervisor Prof. Abdelkrim Beniaiche, of Ferhat Abbas Setif 1 University and Head of Mohamed El Bachir El Ibrahimi University. I feel extremely fortunate to have been blessed with such a great and funny person as my advisor, who helped me shape my scientific outlook in spite of being totally absorbed by his job. Your advices have been invaluable to me on both academic and personal level and have motivated at various times throughout this thesis. I extend my eternal thanks for your endless patience, enduring support and understanding, warm encouragement and raising my confidence up. You have been a source of inspiration for me, You gave me freedom to do what I wanted to do, You believed in my abilities, You have kept me on the path…Your talents never cease to amaze. I will never forget I will be forever grateful to you.

I would like to express my sincere thanks to Prof. Smail Djabi, of Ferhat Abbas Setif 1 University, Prof. Nadir Bouarissa, of M'sila University, and Prof. Abdelkader Nouiri, of Oum El Bouagui University, for their participation in the review panel of this thesis. I am grateful for their valuable and detailed comments.

I'm so thankful to Prof. Nouredine Fenineche and Dr. Michel Moliere, of UTBM University for their co-ordination and helps during the short stay I had in France. They provided countless hours to advise, guide, support and offer key insights that were essential to moving my research forward. It was a pleasure to work with you both in LERMPS. I'd like to thank especially Mrs. Frédérique Petithory and Mrs. Martine Coddet for their welcoming and help and Mr. Bruno Nicolas and Mrs. Emmanuel Arcens for their help with the XRD and FE-SEM measurements and the useful discussions.

I would also like to extend heartfelt thanks to Prof. Elvira Fortunato and Prof. Rodrigo Martins for kindly hosting me in I3N-Cenimat/Cemop Institute of the Nova De Lisboa University. I should definitely thank Dr. Manuel João Mendes for generously providing a strong technical support and for his useful comments and valuable suggestions during the progress of the short stay in Portugal. I have learned quite a lot from his extensive knowledge and many brilliant and creative ideas. Special thanks to the entire PhD students, namely; Kasra Kardarian, Andreia Araújo, Antonio Vicente and to post-doctors, Dr. Sónia Pereira, Ana Pimentel, Joana Pinto, Daniela Gomes, Andriy Lyubchyk and Dr. Ollala Sanchez-Sobrado for assistance with the measurements, fruitful discussions and valued hints. I wish to acknowledge with much appreciation the important role of the laboratory person's namely Dr. Alexandra Gonçalves for giving me such attention, time and permission to use all required equipment and necessary materials to complete the task. I not only learned from them the knowledge and methods, but also a rigorous educational philosophy.

The Ministry of Higher Education and Scientific Research of the Algerian Government is highly acknowledged for providing enough financial support during the short stay internship.

A huge 'thank you' to Prof. Amor Azizi, of Ferhat Abbas Setif 1 University, and his research group for their assistance and support.

Sincere appreciation to all members of staff at the IOMP institute, especially the ex-head Prof. Hocine Guessas as well as Prof. Smail Djabi for being so kind and helpful and for facilitating the administrative stuffs.

I would like to take the opportunity to thank Professors; D. Harzallah, S. Bouzid, S. Dahamna, B. Bouzerafa, A. Ourari and Dr. K. Reggad, of UFAS, for their unwavering help by borrowing me the necessary materials and apparatus during the synthesis and preparation of the samples.

Many thanks to my class mates and colleagues in the LSPONL laboratory; Dr. Bakhouche Belkacem and Nouri Abdelhak, especially my dearest friend Dr. Naima Khebbache who supported me with sincere friendship and encouragement right from the beginning of my thesis research.

The thesis was also a great opportunity to gain more friends from different countries who has supported and encouraged me, I especially enjoyed the insight I received from them

all, namely: the Chinese Dr.Yangzhou Ma, Huang Chunjie and Song Chen, the Tunisian Dr. Amel Masmoudi and Halima Ghorbel, the Portuguese João Campôa, Cátia Cagabushi and Daniela Ribeiro, the Palestinian Nezzal Felasteen and the sweetest Serbian Snezana Reljic.

I would like to acknowledge the crucial rule of all my family members, especially my sisters and brothers that I love so much and my lovely parents. Thank you, my DEAR parents, for the understanding, full moral and financial support, care and help and for being on my side during the completion of this research work. Without your efforts and sacrifices, I would never have been able to complete my PhD study. Your everlasting love and belief in my ability to succeed has been the 'wind beneath my wings'. This is for you.

I would like also to dedicate this work to the memory of my aunt, who always encouraged and gave me the motivation for pursuing higher education regardless the challenge and barriers involved. Unfortunately she will not witness my thesis defense.

I have an immeasurable amount of gratitude for all those who have contributed in my education.

I thank you all

Sara Marouf

Table of Contents

Chapter I. Theoretical background

Chapter II. Preparation and Characterization Methods

Chapter III. Experimental details, results and discussions

List of figures

List of tables

General introduction

Nanotechnology has developed a bridge among all the fields of science and technology for the purpose of manufacturing new materials at the nanoscale level. Materials and structures with low dimensions have excellent properties which enable them to play a crucial role in the rapid progress of the fields of science. The investigation of materials at the nanoscale has gained a great deal of interest as it fills the gap between bulk and atoms or molecules, thus improving our understanding of fundamental properties and providing new physical effects. This has been one of the hottest areas of research in the last twenty years, fueled by the shrinking approach in device fabrication for optoelectronics and electronics [1-3].

Semiconductors are materials that have intermediate conductivity between a conductor like aluminium and an insulator like a glass. Semiconductors are especially important because varying conditions like temperature and impurity (dopant) content can easily alter their properties. Their attractions arises from their low synthetic cost, their solution processing ability and the dependence of their optoelectronic properties as a function of size, shape, doping and surface chemistry [4,5].

The global research interest in wide band gap semiconductors has been significantly focused to zinc oxide (ZnO) due to its excellent properties which make it suitable for wide range of uses in optoelectronics and transparent electronics [6-9].

In recent years, rare-earth (RE) and group III elements doped semiconductors nanostructured materials have attracted great attention in both fundamental studies and applications, thus here we aim to study the effect of the impurity doping on the properties of ZnO thin films that may creates a material with enhanced features.

The thesis can be broadly grouped into two categories; relevant theory of the materials involved and experimental study of the behavior of these materials regarding impurity doping. It is outlined accordingly with chapters one and two dealing with material properties, applications, preparation and characterization, while chapter III discusses the experimental results of undoped and RE or Al doped zinc oxide.

The layout of the three chapters is as follows:

Chapter 1: ***Theoretical background***. This chapter provides a brief discussion on the properties and importance of zinc oxide materials and the potential device applications in optoelectronic fields. An introduction of the main dopants used in this study is also presented.

Chapter 2: ***Preparation and Characterization Methods for ZnO***. This chapter describes the growth mechanism of zinc oxide thin films, namely sol gel and ultrasonic spray pyrolysis. The core apparatus for zinc oxide nanostructure growth and characterization are discussed in detail. The chapter is divided into two main sections; basic nanostructure growth equipment, and description of the equipment used to characterize zinc oxide.

Chapter 3: ***Experimental details, results and discussions***. In this chapter a study of growth of ZnO thin films by sol gel and ultrasonic spray pyrolysis is presented and the issues affecting growth control are discussed. The chapter is divided into three principal sections. The main goal of the first part is to find the optimal deposition conditions. Secondly, the findings of the former section are applied to prepare a series of nominally pure and intentionally doped ZnO thin films with trace amounts of rare earth ions by means of the sol gel technique. Thirdly, ZnO and Al-doped ZnO were ultrasonically sprayed on glass substrates with different Al concentrations and annealed by RTA under vacuum or forming gas in order to study the possibility of deposition at low temperature to allow patterning on flexible substrates.

At the end some general conclusions are given in order to summarize the main points of the subject.

References

[1] A. L. Rogach, A. Eychmuller, S. G. Hickey, and S. V. Kershaw, *Small*, 3(4) 536–557, 2007.

[2] A. P. Alivisatos, *Sci*, 271(5251) 933–937,1996.

[3]M. Rai, A. Yadav, A. Gade, Silver nanoparticles as a new generation of antimicrobials. *Biotechnol. Adv.* 27(1) (2009) 76-83.

[4] A. P. Alivisatos, *J. Phys. Chem*, 100 (1996) 13226-13239.

[5] S. C. Erwin, L. Zu, M. I. Haftel, A. L. Efros, T. A. Kennedy, D. J. Norris, *Nature*, 43 (2005) 91-94.

[6] A. Janotti and C. G. Van de Walle, *Rep. Prog. Phys.* 72 (2009) 126501:1-126501:30

[7] M. Willander, O. Nur, Q. X. Zhao, L. L. Yang, M. Lorenz, B. Q. Cao, J. Zúñiga Pèrez, C. Czekalla, G. Zimmermann, M. Grundmann, A. Bakin, A. Behrends, M. Al-Suleiman, A. El-Shaer, A. Che Mofor, B. Postels, A. Waag, N. Boukos, A. Travlos, H. S. Kwack, J. Guinard and D. Le Si Dang, *Nanotechnology*, 20 (2009) 33200:1-332001:41

[8] Z. L. Wang, *Materials Today*, 7, 26-33, 2004.

[9] Ü. Özgür, Ya. I. Alivov, C. Liu, A. Teke, M. A. Reshchikov, S. Doğan, V. Avrutin, S. -J. Cho and H. Morkoç, *J. Appl. Phys*. 98 (2005) 041301:1-041301:104.

Chapter I. Theoretical background

The present chapter envelops a brief introduction to nanotechnology and its importance in various fields along with a combined portrait and elucidations of zinc oxide and related properties as well as some of its areas of application. The emphasis is also on doping with rare earth (RE) ions which are seen as the most accurate luminescent centers due to their high color purity emission lines and Al which is going to be a valuable replacement of ITO in most TCO applications. All in all, focus will be on the targeted dopants and their principal characteristics. References are provided in the chapter wherever necessary.

I.1 Introduction

Nanostructured materials research is nowadays a rapidly growing field of science due to the consistent efforts and significant contributions of the scientific community across the globe. Nanotechnology, which deals with features as small as a 1 billionth of a meter, is defined as the creation and utilization of materials, systems, and devices through control of matter on the nanometer-length scale. This field is expected to become one of the main driving forces in materials research for the 21st century as it is emerging as a rapidly growing field with its application in science and technology for the purpose of manufacturing new materials at the nanoscale level [1-3]. On a global scale, investment in nanostructured materials dwarfs those in many other important fields of scientific enterprise [4] because their novel properties and functions differ drastically from their bulk counterparts. Particularly, their high volume/surface ratio, surface tailorability, improved solubility, and multifunctionality open a large number of new opportunities that could be realized by down-sizing currently existing structures into the nanometer scale, or by making new types of nanostructures [5, 6]. For instance, the surface area to volume ratio increases as the radius of a particle decreases. If we consider a 1 cm^3 block of material, it has a total surface area of 6 cm^2. However, if we break this block up into smaller cubes of 1 nm wide, these cubes together would have a combined surface area of 60000000 cm^2. This has direct consequences for a nanoparticle since their small size means that a larger proportion of its atoms are located on its surface than is the case for a larger particle [7].

There are different types (fig.I.1) of dimensionality confinement for nanostructure systems, which are described as zero dimensional when they are uniform (clusters), mono dimensional when they are elongated (nanowires) and two dimensional when they are planar (films). Besides of three types of nanomaterials that are commonly used for nanotechnology, another new class of material that has fascinating properties and not confined to the nanoscale in any dimension is the three-dimensional (3D) nanomaterials in which the 0D, 1D and 2D structural elements are in close contact with each other and form interfaces [8, 9].

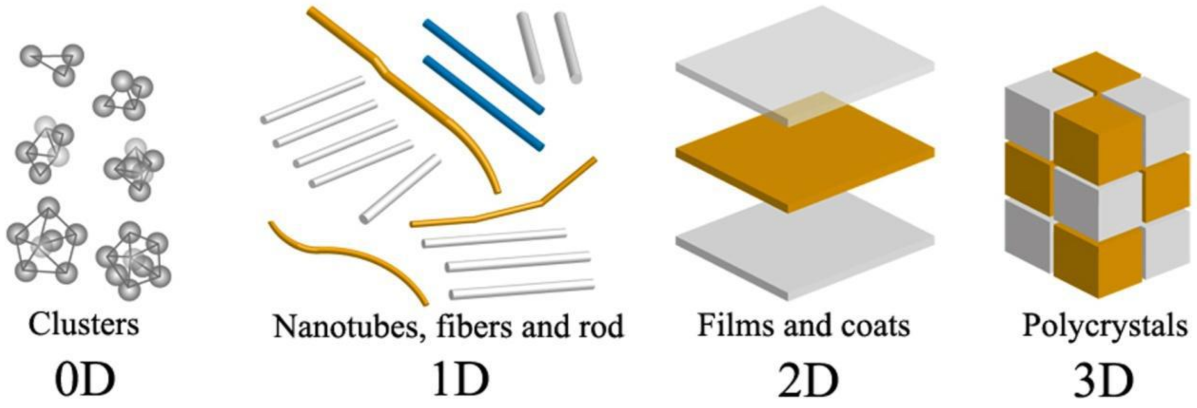

Figure I.1. *Pictorial representation of different types of nanostructures.*

I.2 Zinc oxide as a fascinating material

An intensive research area currently and one of the major focuses of contemporary nanotechnology is the extensive investigations into the control and manipulation of nanostructured metal oxide materials and their application within devices [10, 11]. Metal oxide nanostructures have attracted a great deal of attention for both fundamental size-dependent optoelectronic properties and wide range of applications. Nano-sized zinc oxide, as a versatile material and one of the II–VI compound semiconductors, is the most frequently studied due to its interest in fundamental study and also its applied aspects in a variety of practical applications such as in solar cells, varistors, electrostatic dissipative coating, transparent UV protection films, chemical sensors, piezoelectric transducers, transparent electrodes and electroluminescent devices [12, 13].

Investigations on the synthesis and modification of nanosized ZnO have attracted tremendous attentions for many decades [14]. Recently, fundamental and applied research on ZnO experienced a renaissance due to its prospective use as an optoelectronic material. Moreover, ZnO thin films belong to the class of transparent conducting oxides (TCO) which makes them important components in most thin film solar cells. The cost-effective large-scale production of these films on the one hand and their development with improved properties on the other hand are key challenges in many fields.

ZnO is an oxidic inorganic compound naturally occurring as a mineral *zincite* in the earth crust, which was discovered in 1810 by Bruce in Franklin (New Jersey, USA). As shown in Fig.I.2, *Zincite* is usually colored red or orange by manganese impurities while synthetic ZnO crystal is white. Most commercially used ZnO is produced synthetically which appears as a white powder almost insoluble in water but soluble in any alcohol solvent, such as ethanol and methanol.

Figure I.2. *Photographs of (a) An orange zincite crystal and (b) a synthetic zinc oxide crystal*

Normally, at ambient temperature and pressure, ZnO crystallizes in a wurtzite structure which belongs to the hexagonal system with lattice parameters a = 0.325 nm and c = 0.521 nm. The ZnO structure (Fig.I.3) can be simply described as a number of alternating planes composed of tetrahedrally coordinated O^{2-} and Zn^{2+} ions stacked alternately along the c-axis. The wurtzite-structure lattice is fourfold coordinated. That is, each atom has four nearest neighbor atoms, the zinc ion surrounded by tetrahedral oxygen ions and vice versa. It’s stated that the tetrahedral coordination of ZnO is responsible of a number of physical and chemical properties of ZnO, including piezoelectricity [15-17].

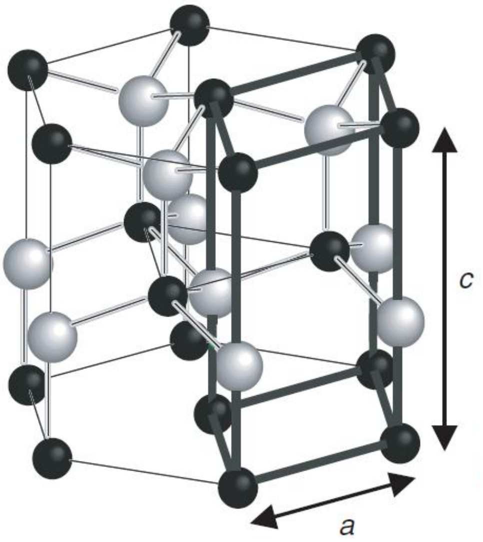

Figure I.3. *Primitive cell (heavy lines) of the ZnO wurtzite structure lattice placed within a hexagonal prism where a and c are the lattice constants. White and black spheres represent O and Zn atoms respectively.*

In fact, different types of nanomaterials like copper, zinc, titanium, magnesium, gold and silver have come up but ZnO have proved to be most effective as it has good features. ZnO is a direct wide bandgap semiconductor with an energy gap of 3.37 eV at room temperature (RT) [18-20] which makes it transparent in visible light and promising material for photonic applications in the UV or blue spectral range. In addition, the excitons in ZnO are thermally stable at room temperature due to the extremely large exciton binding energy (~ 60 meV), even higher than other semiconductor materials like GaN (25 meV), GaAs (4 meV) and ZnSe (22 meV) and is 2.4 times the thermal energy at room temperature (25meV). Such a high binding energy ensures the survival of excitons and a more efficient optical emission and detection even at room temperature. Moreover, ZnO has excellent stability (or resistance) under high-energy radiation (one order higher than that of GaN) and large breakdown strength which makes it a potential material for high-temperature and high-power electronics. Furthermore, it can be easily processed by wet chemical methods on commercially available native substrate growing a variety of nanostructured morphologies by low cost and low temperature methods.

All of these potential advantages motivate intense interest in ZnO, so that several reviews of various aspects about this interesting material have been published in recent years, including a comprehensive overview of ZnO properties, growth methods, and applications. Thus ZnO whilst already possessing a wide application base, has enormous opportunities for society and industry alike due to its unique properties which are now being explored and applied [21-28].

I.3 Doping of ZnO materials

The last decade has witnessed an enormous growth of ZnO related research, largely because of the possibilities of new or improved types of electronic and photonic devices [27]. One of the effective methods for manipulating the physical properties of semiconductors is doping the impurity ions. It has been proved that the physical and chemical properties are greatly influenced by doping of the foreign metals in ZnO lattice [29]. The doping of ZnO is a research topic of considerable interest in its own right. It can be in the form of impurities or native defects in the lattice.

I.3.1Native defects

Doping forms the basis of much of semiconductor technology, however, it can be drastically affected by native point defects. The control of defects and associated charge carriers is of paramount importance in applications that exploit the wide range of materials properties since the defects greatly affect the doping and luminescence efficiency, and may be directly involved in the diffusion mechanisms related to growth, processing and devices degradation. In ZnO, specific native defects have long been believed to play an even more important role. As-grown ZnO frequently exhibits high levels of unintentional *n*-type conductivity, and native point defects have often been invoked to explain this behavior [30,31]. There are a number of intrinsic defects in ZnO with different ionization energies. The electronic energy levels of native imperfections are illustrated in Fig. I.4 where it can be seen that there are several defect states within the band gap and the defect ionization energies vary from ~0.05-2.8 eV. The donor defects are: $Zn_i^{\bullet\bullet}$, $Zn_i^{\bullet}$, $Zn_i^{\times}$,$V_o^{\bullet\bullet}$,$V_o^{\bullet}$, V_o and the acceptor defects are: $V_{Zn}^{''}$,$V_{Zn}^{'}$. The Kröger Vink notation is adopted where Zn, O, i and V designate respectively, zinc, oxygen, interstitial and vacancy. The terms indicate the atomic sites, and superscripted terms indicate charges, where a dot indicates positive charge, a prime indicates negative charge, and a cross indicates zero charge, with the charges in proportion to the number of symbols.

Zn interstitials and oxygen vacancies are known to be the predominant ionic defect types and have most often been mentioned as sources of *n*-type conductivity in ZnO. Because of the different ionization energies, the relative concentrations of the various defects depend strongly on temperature. Under very reducing conditions and at high temperatures, oxygen vacancies may predominate while Zn interstitials are the predominant defects under Zn vapor rich environments.

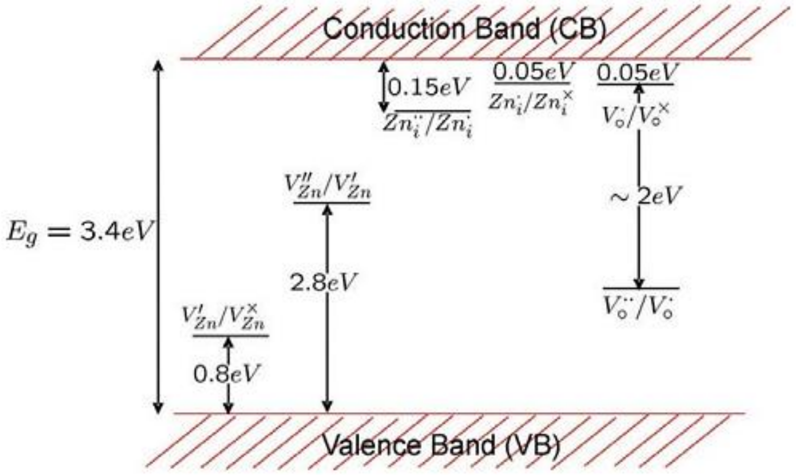

Figure I.4. *Energy levels of native defects in ZnO.*

I.3.2 Impurity doping

It is important to realize that ZnO has a relatively open structure, with a hexagonal close packed lattice where Zn atoms occupy half of the tetrahedral sites. All the octahedral sites are empty. Hence, there are plenty of sites for ZnO to accommodate intrinsic defects and extrinsic dopants. Selective element doping offers a method to adjust ZnO properties which is important for its applications [32]. Principally, there are four main topics of interest in doping ZnO:

1) Doping with donor impurities to achieve n-type conductivity,

2) Doping with acceptor impurities to achieve p-type conductivity,

3) Doping with rare-earth elements to achieve desired optical properties, and

4) Doping with transition metals to achieve desired magnetic properties.

Many types of dopants have been introduced. For instance, group III elements are typically used to dope ZnO with donor impurities. Al-doped ZnO (AZO) films are commonly proposed as a transparent conductive oxide, which can replace for indium tin oxide electrodes in optoelectronic devices. ZnO nanostructures have also been doped with different rare-earth elements. Therefore, when doping with rare-earth elements, it is possible that their emission will be masked by ZnO defect emission, and thus the excitation wavelength must be carefully chosen to establish the effects of doping on optical properties. One of the common problems with doped nanostructures is that the introduction of dopant during growth often results in the change of morphology. The effectiveness of doping will depend on the ease of incorporation of these heteroatoms into zinc substitutional sites in the ZnO lattice [21,22,33,34].

I.3.2.1 Aluminium doped zinc oxide

Indium tin oxide (ITO) is the current most successful transparent conductive oxide, given its remarkable optical and electrical properties. However, the scarcity of indium carries an important drawback for the long-term application due to its intensive use in many optoelectronic devices. Impurity-doped ZnO-based binary compounds, such as Al-doped ZnO are emerging as an alternative potential candidate to ITO since they are inexpensive, nontoxic and much abundant materials in Earth's crust. The abundance of Zn is 75 parts per million (ppm), while Sn is 2.2 ppm and In is only 0.16 ppm. Additionally, the indium of ITO layer can diffuse into the organic materials, leading to degradation of device performance. Besides, the toxic nature of indium could be hazardous to human and environment. The other drawback of ITO films is the chemical instability in a reduced ambient. In comparison to ITO, ZnO:Al films are more stable in reducing ambient (hydrogen plasma and atmosphere), as used for instance in the deposition of hydrogenated silicon thin films.

It has been recognized that a small amount of Al doping in a ZnO matrix (Fig.I.5) is known to enhance the charge carrier density and thereby reduce the resistivity of the material. The Al $^{3+}$ ions are incorporated in Zn $^{2+}$ tetrahedral sites of the ZnO matrix, donating charge carriers and forming a degenerate semiconductor with reduced resistivity. Optically, this blueshifts the absorption edge of the film in accordance with the Burstein–Moss effect [35-37].

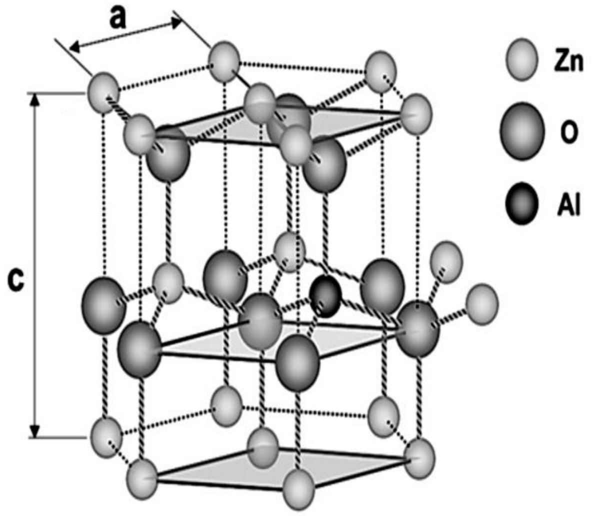

Figure I.5. *Schematic representation of the ZnO wurtzite structure doped by Al.*

AZO films are also wide band gap semiconductors, which show good optical transmittance in the visible and near-infrared regions [38,39]. It was shown that the surface roughness decreases as the Al doping concentration increases. The surface would become smoother due to the enhanced nucleation sites [34]. Due to these unique properties, AZO films have been used as transparent conducting electrodes in solar cells [38,40].

I.3.2.2 Rare earth elements doped Zinc oxide

Rare earth elements have been called the ‘‘vitamin’’ of metals meaning that a small amount of RE elements greatly enhance the properties of metals. They have an important influence on their electrical, magnetic, mechanical and optical properties [41,42]. Basically, the rare earths are not really rare in nature and the term “*rare earth”* is a misnomer. The early Greeks thought that all matter was made up of four elements: air, earth, fire and water, and the *earths* were those materials that could not be changed further by sources of heat, and these oxides seemed to fit that definition. In addition, in the 18th and 19th Century, they were found as a mixture of oxides which have proved to be particularly difficult to separate from each other to obtain the pure elements and there was only one deposit of these elements in the Swedish town Ytterby. Therefore they were thought to be rare. All of the RE elements are actually more abundant than silver, and some are more abundant than lead and even the rarer elements, europium and lutetium are much more abundant than the platinum group elements [43- 45].

In fact, the RE elements occur in two groups known as lanthanides and actinides. Actinides are characterized by the progressive filling of the 5*f* shell [46] while the lanthanides, which are the focus of this study, comprise the series of seventeen elements, outlined in red in the periodic table (Fig.I.6), stretching from Lanthanum to Lutetium, including yttrium and scandium since they have similar properties. Lanthanides are characterized by a partially filled *4f* shell that is shielded from external fields by the outer 6s, 5p, and 5d orbitals which weakens its coupling with the surrounding ligands. Because electronic transitions within their 4*f* subshell are parity forbidden, the energy levels of elements in this series are therefore largely insensitive to the environment in which they are placed, i.e. RE radiative transitions in solid hosts resemble those of the free ions thus leading to a stable and sharp luminescence. When incorporated in crystalline or amorphous hosts, the RE exist as 3+, or occasionally 2+, ions. The 3+ ions all exhibit intense narrow-band intra-4f luminescence in a wide variety of hosts [47-49].

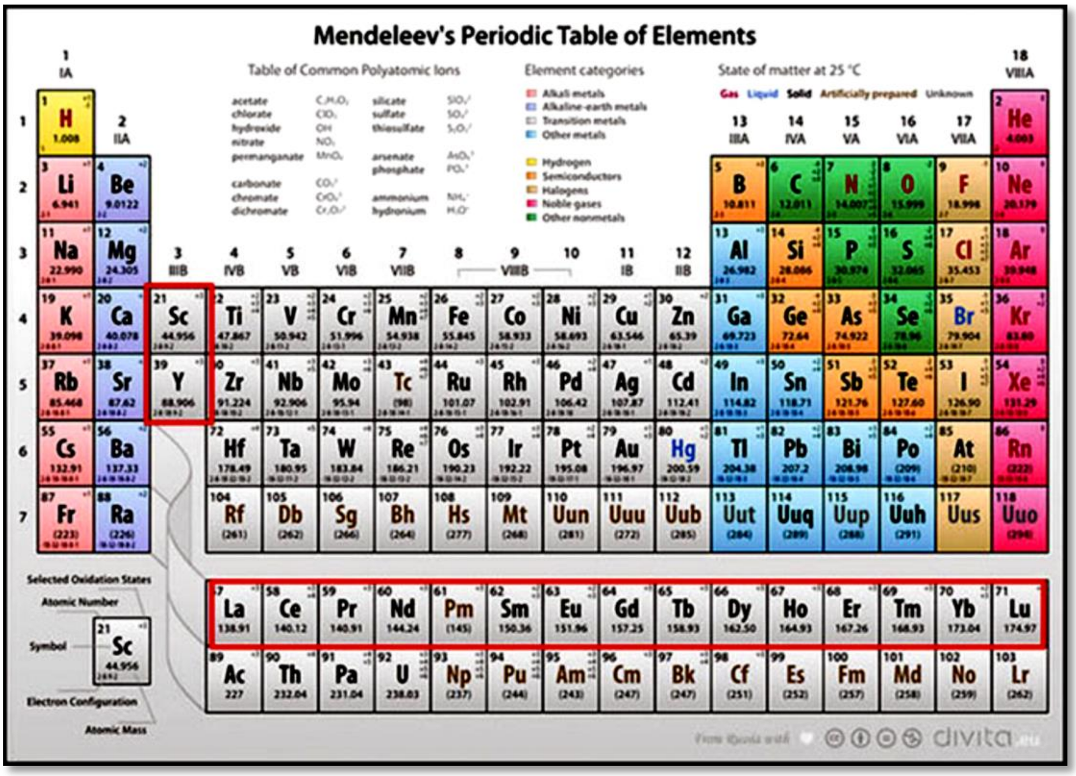

Figure I.6*. The periodic table of elements (Lanthanides are outlined in red).*

Table I.1. Structural and electronic properties of rare earth.

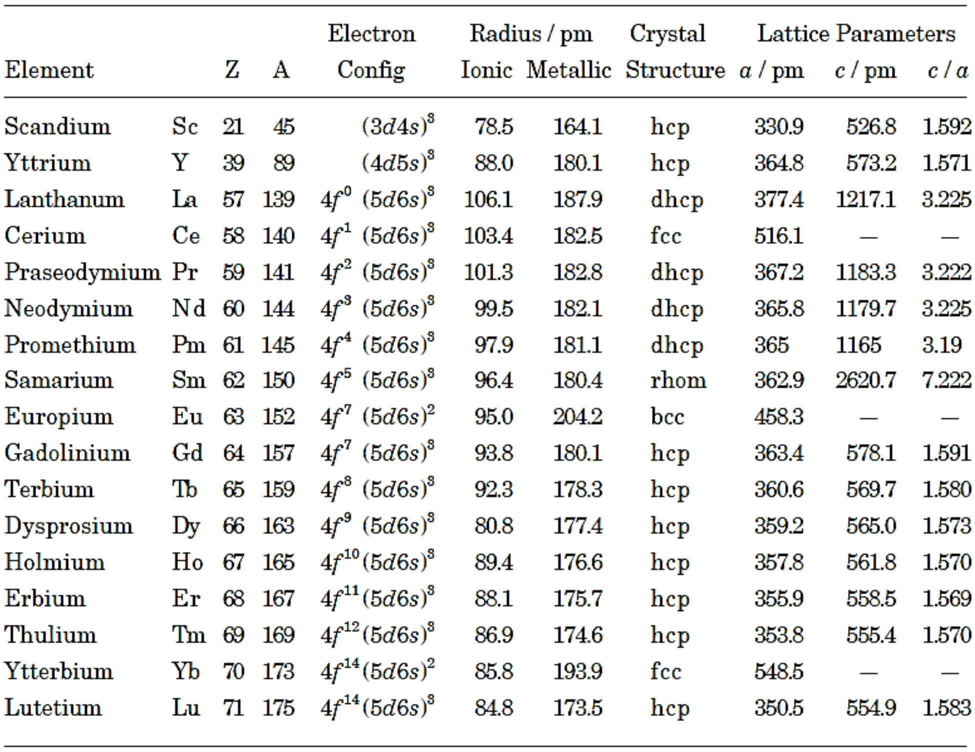

Element		Z	A	Electron Config	Radius / pm Ionic	Radius / pm Metallic	Crystal Structure	Lattice Parameters a / pm	Lattice Parameters c / pm	Lattice Parameters c/a
Scandium	Sc	21	45	$(3d4s)^3$	78.5	164.1	hcp	330.9	526.8	1.592
Yttrium	Y	39	89	$(4d5s)^3$	88.0	180.1	hcp	364.8	573.2	1.571
Lanthanum	La	57	139	$4f^0\ (5d6s)^3$	106.1	187.9	dhcp	377.4	1217.1	3.225
Cerium	Ce	58	140	$4f^1\ (5d6s)^3$	103.4	182.5	fcc	516.1	—	—
Praseodymium	Pr	59	141	$4f^2\ (5d6s)^3$	101.3	182.8	dhcp	367.2	1183.3	3.222
Neodymium	Nd	60	144	$4f^3\ (5d6s)^3$	99.5	182.1	dhcp	365.8	1179.7	3.225
Promethium	Pm	61	145	$4f^4\ (5d6s)^3$	97.9	181.1	dhcp	365	1165	3.19
Samarium	Sm	62	150	$4f^5\ (5d6s)^3$	96.4	180.4	rhom	362.9	2620.7	7.222
Europium	Eu	63	152	$4f^7\ (5d6s)^2$	95.0	204.2	bcc	458.3	—	—
Gadolinium	Gd	64	157	$4f^7\ (5d6s)^3$	93.8	180.1	hcp	363.4	578.1	1.591
Terbium	Tb	65	159	$4f^8\ (5d6s)^3$	92.3	178.3	hcp	360.6	569.7	1.580
Dysprosium	Dy	66	163	$4f^9\ (5d6s)^3$	80.8	177.4	hcp	359.2	565.0	1.573
Holmium	Ho	67	165	$4f^{10}(5d6s)^3$	89.4	176.6	hcp	357.8	561.8	1.570
Erbium	Er	68	167	$4f^{11}(5d6s)^3$	88.1	175.7	hcp	355.9	558.5	1.569
Thulium	Tm	69	169	$4f^{12}(5d6s)^3$	86.9	174.6	hcp	353.8	555.4	1.570
Ytterbium	Yb	70	173	$4f^{14}(5d6s)^2$	85.8	193.9	fcc	548.5	—	—
Lutetium	Lu	71	175	$4f^{14}(5d6s)^3$	84.8	173.5	hcp	350.5	554.9	1.583

The electronic configurations, crystal structures and lattice constants of the RE elements are listed in table I.1. Belonging to a common group, it is not surprising to find that many of the RE metals have similar properties. However, the similarities in their chemical properties that are a result of their atomic structure, and hence a part of their definition, are not necessarily reflected in other properties. The RE metals exist in one of five crystal structures. At room temperature, nine exist in the hexagonal close–packed (hcp) structure, four in the double *c*-axis hcp (dhcp) structure, two in the face–centred cubic (fcc), and one in each of the body–centred cubic (bcc) and rhombic (Sm-type) structures. This distribution changes with temperature and pressure as many of the elements go through a number of structural phase transitions [43]. Additionally, there is a considerable progressive decrease in atomic and ionic radii when going from lower to higher atomic numbers in the lanthanide series. This phenomenon is called the lanthanide contraction. The lanthanides show contraction of the atomic and ionic radii, due to the imperfect shielding of the valence f-orbitals [45]. The 5s and 5p orbitals penetrate the 4f subshell and are not shielded from increasing nuclear charge, and hence because of the increasing effective nuclear charge they contract as the atomic number increases [50].

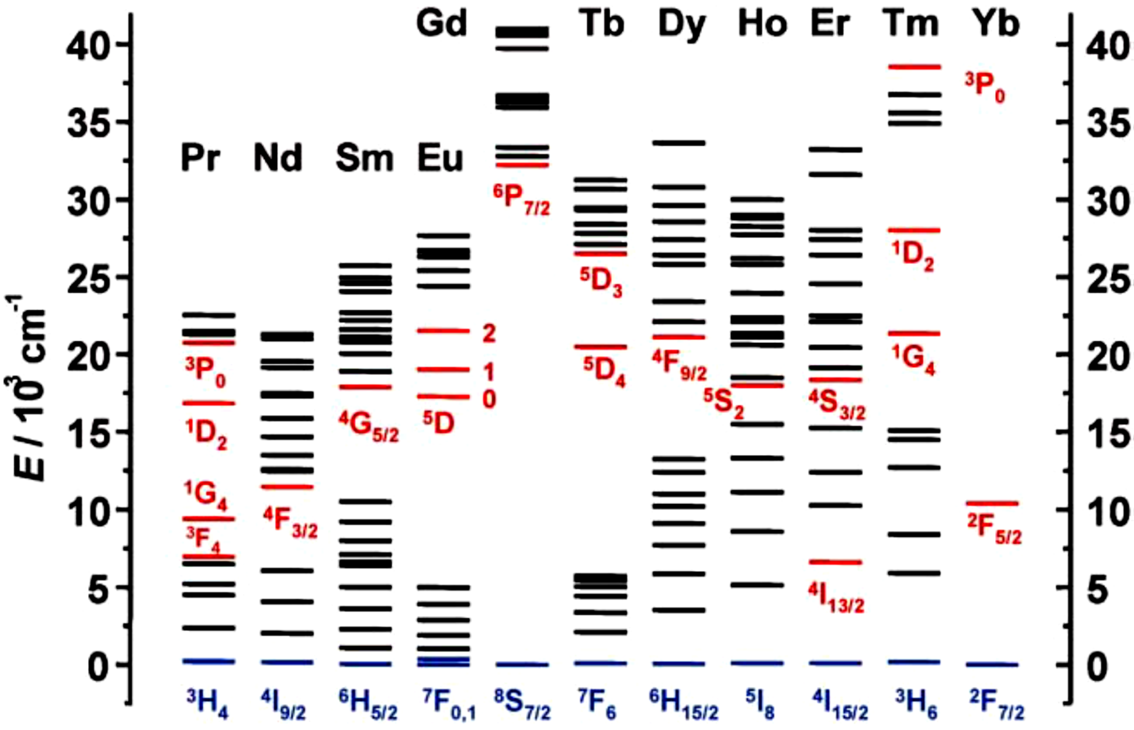

Figure I.7. *Partial energy diagrams for the trivalent lanthanide. The main luminescent levels are drawn in red, while the fundamental level is indicated in blue.*

Most trivalent lanthanides are luminescent, but some are more emissive than others. The emissive properties of a lanthanide ion are governed by the facility of populating the excited state and minimizing non-radiative de-activation paths. The optical properties of lanthanide ions are dominated by the radiative transitions within the 4f manifolds. Therefore, much attention has been paid by many scientists to investigate the RE-related transitions to make a valuable energy level diagram (Fig.I.7) which shows the energy of the different states for several RE^{3+} ions [51]. Depending upon excitation, lanthanide doped luminescent materials can exhibit emission from ultraviolet (UV) to near infrared light region [52]. Depending on the chemical environment of the ion, the shape of the emission spectra may differ substantially, but the energy of the transitions remains relatively insensitive; in addition vibronic transitions as well as emission from other levels may also show up [53].

The host is regarded as the “home” of optically active ions. Since dopant ions in a solid host are impurities embedded in the host lattice, the host ions are substitutionally replaced by dopant ions. Therefore, the host lattice determines the distance between the dopant ions as well as their relative spatial position.

In recent years, the conversion of infrared radiation into visible light in RE ion implanted solid-state nanocrystals has been a focus of intensive research. Their potential application covers broad areas, including color displays and in optoelectronics as emitters at visible wavelength. Researchers are attempting to seek the potentials of metal-ion doped functional hosts as multifunctional systems, which combine light emission with other intrinsic properties of the host such as piezoelectricity and electro-optic properties. Therefore, wide band-gap semiconductors, such as ZnO, have extensively been utilized as promising hosts for optical and electronic applications. Due to the remarkable excitonic properties of ZnO, many significant exciton effects may be expected in low-dimensional ZnO nanostructures [54-57].

Considering the unique optical properties, along with the tunable emission wavelengths, Nd^{3+} and Pr^{3+} ion, a well-known activators dopants have been opted for the current study. We believe the sharp and narrow intense emissions (in the visible range) of this RE metals in their trivalent form could be enhanced.

a) Praseodymium

In 1841, *Mosander* extracted the rare earth *didymia* that was separated later into two others, *praseodymia* and *neodymia*. Praseodymium (*Gr. prasios, green, and didymos, twin)* was not prepared in its pure metallic form until 1931. It is a soft, silvery, malleable, and ductile element (Fig.I.8) occurring along with other RE elements in a variety of minerals. Monazite and bastnasite are the two principal commercial sources of the RE metals. The element is somewhat more resistant to corrosion in air than europium, lanthanum, cerium, or neodymium and is usually kept sealed in plastic or covered with oil because it does develop a green oxide coating that spalls off when exposed to air.

As with other REs, compounds of these elements in solution have distinctive sharp spectral absorption bands or lines, some of which are only a few Angstroms wide. The RE oxides, including Pr_2O_3 are among the most refractory substances known. Along with other REs, it is widely used to fabricate the electrodes of the high-intensity carbon arc lamps used in searchlights and motion-picture projectors. In addition, small quantities of the metal are added to magnesium to form an alloy that is both stronger and more corrosion-resistant than the original metals for making automobile and aircraft parts. Praseodymium salts are often used to color glasses and enamels; when mixed with certain other materials, praseodymium produces an intense and unusually clean yellow color in glass [58,59]. Further coloring effects are obtainable by combining REs with other elements, for example, Neodymium colors glass bright red, praseodymium colors glass green, and their mixture colors glass blue [60].

The Pr^{3+} ion shows a number of different emissions (Fig. I.7), both in visible and NIR (Near Infrared Region), depending on the host lattice in which it is incorporated, such as; red emission from the $^1D_2$ level, green emission from the $^3P_0$ level, blue from the $^1S_0$ level and ultraviolet from the 4f5d state[61].

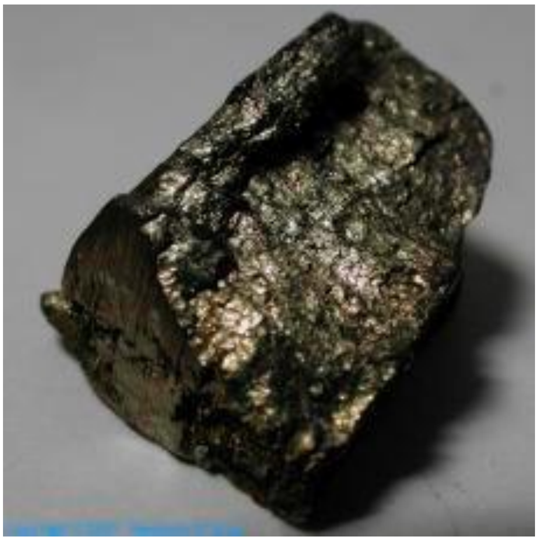

Figure I.8. *Praseodymium element photograph.*

b) Neodymium

In 1841, Mosander extracted from cerite a new rose-colored oxide, which he believed contained a new element. The element was named didymium, as it was an inseparable twin brother of lanthanum. Later didymium was separated into two new elemental components, neodymia and praseodymia. Neodymium (*Gr. neos, new, and didymos, twin*) is one of the RE elements in the group of Lanthanides has been the focus of numerous investigations because of its unique optical properties and promising applications in optoelectronic and magnetic devices. Pure neodymium metal was not isolated until 1925. It has a bright silvery metallic luster. It is one of the more reactive RE metals that quickly tarnishes in air, forming an oxide which spalls off exposing metal to oxidation. Therefore it is usually stored in a plastic wrapping or covered with mineral oil. Neodymium, as with other REs, should be handled with care since it has a low-to-moderate acute toxic rating. The metal can be found chiefly in the monazite and bastnasite ores. It is present in misch metal to the extent of about 18%, long known and used as a pyrophoric alloy for light flints. Neodymium and its oxides, which tend to be rose colored, are used to color glass delicate shades ranging from pure violet through wine-red and warm gray, for special purposes. Light transmitted through such glass shows unusually sharp absorption bands. Some examples of such glass are the colored glass in welders' and glassblowers' goggles because it blocks infrared radiation and the "artificial ruby" used as a substitute for real rubies in certain types of lasers. Glass containing neodymium can be used as a laser material to produce coherent light [58,59]. For instance, Yttrium–aluminum–garnet (YAG) solid-state lasers utilize neodymium because it has optimal absorption and emitting wavelengths.

Most famous of the primary applications include neodymium–iron–boron ($Nd_2Fe_{14}B$) permanent magnets, indispensable and extensively used in every area of modern technology (both civilian and defense) that relies on superior performance, reliability, and miniaturization. Neodymium was also used in displays to enhance contrast between reds and greens [60].

Neodymium ion presents an interesting emission in the near infrared region which is widely used for laser operation. The three NIR luminescence emission peak at 880 nm, 1060 nm and 1330 nm corresponds to ${}^4F_{3/2} \rightarrow {}^4I_{9/2}$, ${}^4F_{3/2} \rightarrow {}^4I_{11/2}$ and ${}^4F_{3/2} \rightarrow {}^4I_{13/}2$. In addition, five major absorption bands Nd^{3+} in the visible and NIR range can be observed at 520nm, 580nm, 745nm, 800nm, 880nm. [62].

Figure I.9. *Neodymium element photograph.*

I.4 ZnO as a multifunctional material

Transparent conducting oxides are a unique class of materials, combining the properties of near-metallic conductivity, high optical transmittance in the visible region of electromagnetic radiation and high reflectance in the NIR. Due to this remarkable combination of properties TCO materials are essential in many optoelectronic devices such as flat panel displays, smart windows, light-emitting diodes and photovoltaic cells, where they are used to either apply or collect electrical signals without reducing optical transmission [63,64]. ZnO related research, has been largely reported lately driven by specific optical or electrical characteristics of this semiconductor [65]; It is a remarkable multifunctional and biocompatible direct-,wide-bandgap semiconductor, with a distinctive property set and a unique potential for nanostructuring [66]. Recent research efforts have been focused on the application of ZnO-based thin films as TCO. ZnO films could be doped with aluminum, indium, or gallium to achieve high conductivity even when stored in a high-temperature or uncritical environment. High thermal stability is a necessary condition since most device process procedures consist of a series of heat treatments [67].

I.4.1 Light emitting diodes (LEDs)

LEDs have been reported both for homojunctions and heterojunctions with different materials. Very wide ranges of device performances have been reported in the literature, in terms of the turn-on voltages, I–V curves, and emission colors [68]. ZnO-based light emitters have been considered as a potential candidate for the next generation of high efficiency blue/near-UV light sources, due to the direct wide band gap energy and the large exciton binding energy at room temperature which are important factors in the design of LEDs. A variety of light emitting devices based on ZnO nanostructures have been reported to date. It’s used as an active layer in homojunction and heterojunction LEDs for the enhancement of light extraction and thus improvement of the overall efficiency by minimizing the losses due to light trapped within the device due to total internal reflections. Different dopants and doping methods have been reported for the achievement of p–n junctions. Reports on homojunction LEDs based on ZnO have been less common compared to various heterojunction devices. It was shown that in ZnO film-based homojunction LEDs that LED performance is significantly affected by the passivation layer. Compared to thin film devices, LEDs based on nanostructures are expected to show some advantages. It was proposed that nanowire based devices may exhibit higher efficiency compared to thin film based devices due to possibility to achieve increased light extraction. Obviously, from the differences in the reported results in the literature in terms of turn-on voltage and emission spectra, the device performance is strongly dependent on the device architecture and ZnO nanomaterial properties, which are in turn affected by native defects and fabrication conditions. More often in LEDs, heterojunctions of n-ZnO and other p-type materials have been used, of which p-GaN is of particular interest considering it has similar crystallographic and electronic properties to ZnO. In addition, it has been suggested that the ZnO nanowire/GaN substrate heterojunction has higher carrier injection efficiency and a higher recombination rate than other junctions [18, 21,65]. ITO or close variants such as indium zinc oxide is currently also the anode of choice for organic light emitting devices OLEDs. White OLEDs have been demonstrated with high power efficiency at a brightness level suitable for general lighting. This makes them a potential high efficiency, low cost, solid state replacement for fluorescent lighting. In the context of the triple market requirements of cost effectiveness, reliability, and scalability, the TCO/substrate combination becomes an important factor in the viability of OLEDs for lighting applications. Several studies have examined OLEDs employing ZnO substitutionally doped with aluminum (AZO) which is a promising class of indium-free TCOs for OLED applications. This system has the advantages of zinc being significantly less expensive than indium having an engineerable band gap via magnesium inclusion and tailorable conductivity by doping [69].

I.4.2 Solar cells

The photovoltaic technology of converting sunlight into electricity has been acknowledged as a promising way to meet the growing energy needs and the increasing concerns about carbon dioxide emission from the consumption of fossil fuels. Thin film solar cells are one of the attractive technologies for generating electrical energy by absorbing photons from sunlight. ZnO is a material of considerable interest for applications in low cost photovoltaics. Devices with a variety of ZnO morphologies have been reported to date, such as dye-sensitized solar cells and hybrid organic–inorganic nanostructure solar cells.

ZnO has a role in two disparate aspects of photovoltaic technology. First, use of transparent conductive ZnO in the front electrodes of solar cells can eliminate the shadow effect related to metal-finger contacts. Secondly, n-type ZnO films may also be used within the photovoltaic structure itself, for example as a tunnel junction in amorphous silicon cells or as part of the p/n junction in some solar cells.

Moreover, polymer solar cells have attracted considerable attention due to their combined advantages of high power conversion efficiency, good stability, rapid energy payback time, low-cost, and compatible with flexible substrate. For the polymer solar cells, the device performance critically relies on the optical and electrical properties of cathode buffer layers as well as the condition of the interface between cathode buffer layers and the active layer. Engineering the cathode buffer layers and the interface thereof has been considered as an essential issue for the next-stage development of polymer solar cells towards high efficiency and good long-term stability. Among many materials, ZnO is the most extensively investigated one for cathode buffer layer in the polymer solar cells, mainly due to its suitable energy levels, high electron mobility, good transparency, environmental stability and low cost. These include cells with different ZnO morphologies and different cell preparation procedures. Another merit of ZnO as the cathode buffer layer material is that it can be easily processed via a solution method with subsequent thermal treatment at relatively low temperatures. Also, in the polymer solar cells with inverted geometry, a ZnO film inserted between the active layer and the cathode can function as a cathode buffer layer to extract and transport electrons, and simultaneously block the reverse flow of holes from the donor polymer to the cathode.

Thus, although solar cells with ZnO nanostructures have been demonstrated, considerable improvements in the efficiency are still needed in order to achieve fast electron injection, fast electron transport, and low recombination losses at the same time. Possible methods to improve the performance included improvements in absorption, exciton dissociation, and charge collection (either by improved transport or reduced recombination) [21,65,68,70,71].

I.4.3Flat screen displays

Transparent electronics has gained special attention in recent years due to their wide range of device applications for information display and information storage. Especially, high-performance thin-film transistors (TFTs) have been receiving strong attention since they are the fundamental building blocks in realizing the potential applications of the next-generation displays [72]. The fabrication of next-generation displays, which require a large size, high resolution, and a fast response time, faces challenges such as achieving high mobility, large-area uniform deposition, and a precise patterning process [73].

The implementation of transparent electronic devices requires the use of material components that could be formed using controlled deposition in the appropriate orientation onto a transparent flexible substrate. The most important electrical parameters in quantifying TFT performance are the active channel mobility, turn-on gate voltage, and the drain current on-to-off ratio. High performance transparent TFTs for displays or other optoelectronic applications should have high electron mobility and a high on/off current ratio. The key issues for further development are related to achieving higher mobility, lowering the background electron concentration, and a good control on the carrier concentration. In order to achieve transparent TFTs with high mobility and high stability, oxide-based semiconductors are the most feasible material as a channel layer.

ZnO shows great promise as an active layer in TFTs due to its exceptional electronic and optoelectronic properties. The high mobility and transparency of ZnO combined with a low temperature deposition process make ZnO a potential candidate for use in flexible and transparent display applications. Except being transparent, ZnO-based transparent TFTs have been shown to exhibit higher channel mobilities and on-to-off ratios compared to their Si counterparts [74,75].

I.5 References

[1] A. L. Rogach, A. Eychmüller, S. G. Hickey, S. V. Kershaw, Infrared‐emitting colloidal nanocrystals: synthesis, assembly, spectroscopy, and applications. *Small* 3(4) (2007) 536-557.

[2] W. H. Suh, K. S. Suslick, G. D. Stucky, Y. H. Suh, Nanotechnology, nanotoxicology, and neuroscience. *Prog. Neurobiol*. 87(3) (2009) 133-170.

[3]M. Rai, A. Yadav, A. Gade, Silver nanoparticles as a new generation of antimicrobials. *Biotechnol. Adv*. 27(1) (2009) 76-83.

[4] S. Bandyopadhyay, Electrochemically Self-Assembled Nanoarrays, Encyclopedia of Nanoscience and Nanotechnology, Marcel Dekker, Inc., (2004). pp1073-1085

[5] J. Gao, B. Xu, Applications of nanomaterials inside cells. *Nano Today* 4(1) (2009) 37-51.

[6] X. Fang, T. Zhai, U. K. Gautam, L. Li, L. Wu, Y. Bando, D. Golberg, ZnS nanostructures: from synthesis to applications. *Prog. Mater. Sci. 56*(2) (2011) 175-287.

[7] Matthew Shortell, PhD thesis, Zinc Oxide Quantum Dot Nanostructures, Queensland University of Technology, (2014).

[8] J. Gangwar, B. K. Gupta, S. K. Tripathi, A. K. Srivastava, Phase dependent thermal and spectroscopic responses of Al_2O_3 nanostructures with different morphogenesis. *Nanoscale* 7(32) (2015) 13313-13344.

[9] E. Comini, C. Baratto, G. Faglia, M. Ferroni, A. Vomiero, G. Sberveglieri, Quasi-one dimensional metal oxide semiconductors: Preparation, characterization and application as chemical sensors. *Prog. Mater. Sci*. 54 (1) (2009) 1-67.

[10] K. Keis, E. Magnusson, H. Lindström, S. E. Lindquist, A. Hagfeldt, A 5% efficient photoelectrochemical solar cell based on nanostructured ZnO electrodes. *Sol. Energ. Mat. Sol. Cells* 73 (1) (2002) 51-58.

[11] A. M. Peiró, P. Ravirajan, K. Govender, D. S. Boyle, P. O'Brien, D. D. Bradley, J. Nelson, J. R. Durrant, Hybrid polymer/metal oxide solar cells based on ZnO columnar structures. *J. Mater. Chem.* 16 (21) (2006) 2088-2096.

[12] L. Tang, B. Zhou, Y. Tian, F. Sun, Y. Li, Z. Wang, Synthesis and surface hydrophobic functionalization of ZnO nanocrystals via a facile one-step solution method. *Chem. Eng. J.* 139 (3) (2008) 642-648.

[13] C. Chen, P. Liu, C. Lu, Synthesis and characterization of nano-sized ZnO powders by direct precipitation method. *Chem. Eng. J*. 144(3) (2008) 509-513.

[14] R. Hong, T. Pan, J. Qian, H. Li, Synthesis and surface modification of ZnO nanoparticles. *Chem. Eng. J.* 119(2) (2006) 71-81.

[15] K. Ellmer, A. Klein, B. Rech, *Transparent Conductive Zinc Oxide: Basics and Applications in Thin Film Solar Cells*. Springer Series in Materials Science, 104, Springer, (2008).

[16] S. K. Arya, S. Saha, J. E. Ramirez-Vick, V. Gupta, S. Bhansali, S. P. Singh, Recent advances in ZnO nanostructures and thin films for biosensor applications: review. *Anal. Chim. Acta* 737 (2012) 1-21.

[17] S. S. Alias, A. A. Mohamad, *Synthesis of zinc oxide by sol-gel method for photoelectrochemical cells*. Springer Briefs in Materials. (2014).

[18] S. Xu, Z. L. Wang, One-dimensional ZnO nanostructures: solution growth and functional properties. *Nano Res*. 4(11) (2011) 1013-1098.

[19] N. Mir, M. Salavati-Niasari, F. Davar, Preparation of ZnO nanoflowers and Zn glycerolate nanoplates using inorganic precursors via a convenient rout and application in dye sensitized solar cells. *Chem. Eng. J*. 181 (2012) 779-789.

[20] N. Han, L. Chai, Q. Wang, Y. Tian, P. Deng, Y. Chen, Evaluating the doping effect of Fe, Ti and Sn on gas sensing property of ZnO. *Sensor. Actuat. B-Chem*. 147(2) (2010) 525-530.

[21] A. B. Djurišić, A. M. C. Ng, X. Y. Chen, ZnO nanostructures for optoelectronics: material properties and device applications. *Prog. Quant. Electron.* 34(4) (2010)191-259.

[22] A. B. Djurišić, Y. H. Leung, Optical properties of ZnO nanostructures. *Small* 2(8-9) (2006) 944-961.

[23] R. Wahab, I. H. Hwang, Y. S. Kim, H. S. Shin, Photocatalytic activity of zinc oxide micro-flowers synthesized via solution method. *Chem. Eng. J.* 168 (1) (2011) 359-366.

[24] P. Uthirakumar, H. G. Kim, C. H. Hong, Zinc oxide nanostructures derived from a simple solution method for solar cells and LEDs. *Chem. Eng. J.*155 (3) (2009) 910-915.

[25] J. Zhong, PhD thesis, Optical Properties of Zinc Oxide Nanotips and their Device Applications, the State University of New Jersey, (2007).

[26] F. C. Tsao, PhD thesis, Growth Mechanism and Characterizations of ZnO Nanowires, Tsing-Hua National Central University, (2007).

[27] C. Jagadish, S. J. Pearton, *Zinc oxide bulk, thin films and nanostructures: processing, properties, and applications*. Elsevier. Eds., (2011).

[28] M. Willander, *Zinc Oxide Nanostructures: Advances and Applications*. Pan Stanford Publishing. (2014).

[29] M. Subramanian, P. Thakur, S. Gautam, K. H. Chae, M. Tanemura, T. Hihara, S. Vijayalakshmi, T. Soga, S. S. Kim, K. Asokan, R. Jayavel, Investigations on the structural, optical and electronic properties of Nd doped ZnO thin films. *J. Phys. D: Appl. Phys.* 42(10) (2009) 105410.

[30] A. Janotti, C. G. Van de Walle, Native point defects in ZnO. *Phys. Rev. B*, 76(16), (2007) 165202.

[31] J. C. Fan, K. M. Sreekanth, Z. Xie, S. L. Chang, K. V. Rao, p-Type ZnO materials: theory, growth, properties and devices. *Prog. Mater. Sci.* 58 (6) (2013) 874-985.

[32] L. Schmidt-Mende, J. L. MacManus-Driscoll, ZnO–nanostructures, defects, and devices. *Mater. Today*. 10(5) (2007) 40-48.

[33] C. G. Granqvist, Transparent conductors as solar energy materials: A panoramic review. *Sol. Energ. Mat. Sol. Cells* 91(17) (2007) 1529-1598.

[34] Z. C. Feng, *Handbook of Zinc Oxide and Related Materials: Volume Two, Devices and Nano-Engineering*. Taylor & Francis, CRC Press, 2012.

[35] A. Lyubchyk, A. Vicente, B. Soule, P. U. Alves, T. Mateus, M. J. Mendes, H. Águas, E. Fortunato, R. Martins, Mapping the electrical properties of ZnO-based transparent conductive oxides grown at room temperature and improved by controlled postdeposition annealing, *Adv. Electron. Mater.* 2 (2016) 1500287.

[36] X. Jiang, F. L. Wong, M. K. Fung, S. T. Lee, Aluminum-doped zinc oxide films as transparent conductive electrode for organic light-emitting devices. *Appl. Phys. Lett.* 83(9) (2003) 1875-1877.

[37] M. M. Khan, S. Kumar, M. N. Khan, M. Ahamed, A. S. Al Dwayyan, Microstructure and blueshift in optical band gap of nanocrystalline $Al_xZn_{1-x}O$ thin films. *J. Lumin.*155 (2014). 275-281.

[38] H. Kim, C. M. Gilmore, J. S. Horwitz, A. Pique, H. Murata, G. P. Kushto, R. Schlaf, Z. H. Kafafi, D. B. Chrisey, Transparent conducting aluminum-doped zinc oxide thin films for organic light-emitting devices. *Appl. Phys. Lett.* 76(3) (2000) 259-261.

[39] A. V. Singh, R. M. Mehra, N. Buthrath, A. Wakahara, A. Yoshida, Highly conductive and transparent aluminum-doped zinc oxide thin films prepared by pulsed laser deposition in oxygen ambient. *J. Appl. Phys*. 90 (11) (2001) 5661-5665.

[40] O. Szabo, S. Kováčová, V. Tvarožek, I. Novotný, P. Šutta, M. Netrvalova, D. Rossberg. P. Schaaf, Nanocolumnar growth of sputtered ZnO thin films. *Thin Solid Films* 591 (2015) 230-236.

[41] C. M. L. Wu, D. Q. Yu, C. M. T. Law, L. Wang, Properties of lead-free solder alloys with rare earth element additions. *Mater. Sci. Eng. R-Rep.* 44 (1) (2004) 1-44.

[42] P. Liang, J. Cao, R. Liu, Y. Liu, Determination of trace rare earth elements by inductively coupled plasma optical emission spectrometry after preconcentration with immobilized nanometer titanium dioxide. *Microchim Acta* 159(1-2) (2007) 35-40.

[43] S. D. Barrett, S. S. Dhesi, *The structure of rare-earth metal surfaces*, World Scientific, (2001).

[44] K.A. Gschneidner Jr., L. Eyring, *Handbook on the Physics and Chemistry of Rare Earths*, Vol. 1, *North-Holland Publishing Co.*, Amesterdam, (1978).

[45] J. H. L. Voncken, *The Rare Earth Elements: An Introduction*, Springer, (2015).

[46] M. Marceddu, PhD thesis, Photoluminescence Properties of Lanthanide doped Wide Gap Compounds of Interest in Photonics, University Degli Studi di Cagliari, (2007).

[47] A. J. Kenyon, Recent developments in rare-earth doped materials for optoelectronics. *Prog. Quant. Electron.* 26 (4) (2002) 225-284.

[48] D. Geskus, S. Aravazhi, S. M. García-Blanco, M. Pollnau, Giant optical gain in a rare-earth-ion-doped microstructure. *Adv. Mat.* 24 (10) (2012)19-22.

[49] D. Wang, G. Xing, M. Gao, L. Yang, J. Yang, T. Wu, Defects-mediated energy transfer in red-light-emitting Eu-doped ZnO nanowire arrays. *J. Phys. Chem. C* 115(46) (2011) 22729-22735.

[50] S. Cotton, *Lanthanide and actinide chemistry*, John Wiley & Sons Ltd, (2006).

[51] J. C. G. Bünzli, C. Piguet, Taking advantage of luminescent lanthanide ions. *Chem. Soc. Rev.* 34(12) (2005)1048-1077.

[52] P. Kumar, S. Singh, B. K. Gupta, Future prospects of luminescent nanomaterial based security inks: from synthesis to anti-counterfeiting applications. *Nanoscale,* 8(30) (2016) 14297-14340.

[53] P. Hänninen, H. Härmä, *Lanthanide luminescence: photophysical, analytical and biological aspects* (Vol. 7). Springer Science & Business Media. (2011).

[54] Y. Zhang, J. Hao, Metal-ion doped luminescent thin films for optoelectronic applications. *J. Mater. Chem. C* 1(36) (2013) 5607-5618.

[55] F. Gu, S. F. Wang, M. K. Lü, G. J. Zhou, D. Xu, D. R. Yuan, Structure evaluation and highly enhanced luminescence of Dy3+-doped ZnO nanocrystals by Li+ doping via combustion method. *Langmuir,* 20(9) (2004) 3528-3531.

[56] X. Wang, X. Kong, Y. Yu, Y. Sun, H. Zhang, Effect of annealing on upconversion luminescence of ZnO: Er3+ nanocrystals and high thermal sensitivity. *J. Phys. Chem. C* 111(41) (2007) 15119-15124.

[57] E. Matei, M. Enculescu, I. Enculescu, Single bath electrodeposition of samarium oxide/zinc oxide nanostructured films with intense, broad luminescence. *Electrochimi. Acta* 95 (2013) 170-178.

[58] W. M. Haynes, *CRC Handbook of Chemistry and Physics*, 96th Ed, CRC Press-Taylor and Francis, (2016).

[59] A. Stwertka, *A Guide to the Elements*,2nd ed, Oxford University Press, (2002).

[60] N. Krishnamurthy, C. K. Gupta, *Extractive Metallurgy of Rare Earths*, 2nd Ed, CRC Press/Taylor and Francis, (2016).

[61] B. Di Bartolo, V. Goldberg, D. Pacheco, *Luminescence of inorganic solids*. Plenum Pub Corp, New York, (1978).

[62] R. Pandiyan, PhD thesis, Growth by radio frequency sputtering and characterization of rare earth doped wide bandgap oxides, University of Trento- UPMC-Sorbonne University, (2013).

[63] T. O. L. Sunde, PhD thesis, Aqueous sol-gel processing of transparent conducting rare earth doped indium tin oxide, Norwegian University of Science and Technology, (2013).

[64] R. A. Maniyara, V. K. Mkhitaryan, T. L. Chen, D. S. Ghosh, V. Pruneri, An antireflection transparent conductor with ultralow optical loss (< 2%) and electrical resistance (< 6 Ω sq^{-1}). *Nat. Commun*. 7 (2016) 13771.

[65] A. Moezzi, A. M. McDonagh, M. B. Cortie, Zinc oxide particles: Synthesis, properties and applications. *Chem. Eng. J.* 185 (2012).

[66] D. J. Rogers, F. H. Teherani, P. Bove, R. McClintock, M. Razeghi, Improved LEDs and photovoltaics by hybridization and nanostructuring. *SPIE Newsroom*, 10(2.1201206), 004238. (2012).

[67] J. K. Sheu, M. L. Lee, Y. S. Lu, K. W. Shu, Ga-doped ZnO transparent conductive oxide films applied to GaN-based light-emitting diodes for improving light extraction efficiency. *IEEE J. Quant. Electron*. 44(12) (2008) 1211-1218.

[68] A. B. Djurišić, X. Chen, Y. H. Leung, A. M. C. Ng, ZnO nanostructures: growth, properties and applications. *J. Mater. Chem.* 22(14) (2012) 6526-6535.

[69] J. J. Berry, D. S. Ginley, P. E. Burrows, Organic light emitting diodes using a Ga: ZnO anode. *Appl. Phys. Lett.* 92(19) (2008)170.

[70] Y. C. Wang, B. Y. Lin, P. T. Liu, H. P. D. Shieh, Photovoltaic electrical properties of aqueous grown ZnO antireflective nanostructure on Cu (In, Ga) Se $_2$ thin film solar cells. *Opt.express* 22(101) (2014) A13-A20.

[71] Z. Liang, Q. Zhang, L. Jiang, G. Cao, ZnO cathode buffer layers for inverted polymer solar cells. *Energy Environ. Sci.* 8(12) (2015) 3442-3476.

[72] C. H. Ahn, K. Senthil, H. K. Cho, S. Y. Lee, Artificial semiconductor/insulator superlattice channel structure for high-performance oxide thin-film transistors. *Sci. Rep.* 3, 2737; DOI:10.1038/srep02737 (2013).

[73] S. W. Cho, D. E. Kim, W. J. Kang, B. Kim, D. H. Yoon, K. S. Kim, H. K. Cho, Y. H. Kim, Y. Kim, Chemical durability engineering of solution-processed oxide thin films and its application in chemically-robust patterned oxide thin-film transistors. *J. Mater. Chem. C* 5(2) (2017) 339-349.

[74] H. Morkoç, Ü. Özgür, *Zinc Oxide*. Wiley-VCH Verlag GmbH & Co. KGaA, (2009).

[75] J. S. Meena, M. C. Chu, Y. C. Chang, H. C. You, R. Singh, P. T. Liu, H. P. D. Shieh, F. C. Chang, F. H. Ko, Effect of oxygen plasma on the surface states of ZnO films used to produce thin-film transistors on soft plastic sheets. *J. Mater. Chem. C* 1(40) (2013) 6613-6622.

Chapter II. Preparation and Characterization Methods

Thin Films play an important role in any multilayered thin film devices. The defect free, uniform and high quality films are required to get high performance thin film devices. Thin films used in the semiconductor industry are deposited by a variety of techniques. This chapter presents a brief description of the two specific techniques, i.e. sol gel and ultrasonic spray pyrolysis that have been used for the synthesis of various undoped and doped nanomaterials explored in this study. The rest of the chapter is devoted to the physical and electrical characterization techniques used to analyze the deposited films.

II.1 Synthesis of ZnO thin film

The dependence of the properties of nanostructured materials on both the size and shape of the nanocrystal is a phenomenon of both fundamental scientific interest and technological applications. In order to advance the basic understanding of the principles that determine the shape and to provide tailored building blocks for nanodevices, several methods have been developed to control the shape, dimensionality, and assembly of nanostructures into organized patterns which provide valuable routes to the design of functional materials and to a variety of device applications [1]. Thin films are extremely important systems that are used in many domains of application, including microelectronics, solar cells, and glass windows, since they bring an additional function at the surface of any kind of materials [2, 3] Thin films of elements, alloys and chemical compounds can be formed on solid substrates by various wet and dry chemical and physical deposition methods. Depending on the applied process, depositions are performed in air or in environmentally controlled atmosphere, under reduced pressure or in vacuum [4].

Among those processes, physical deposition methods typically require high temperature and pressure as well as particular substrates and result in low product yield. These methods produce high quality ZnO thin films; however, they are energy and cost intensive. Therefore, they are less likely to be able to integrate the large scale production so they have been less widely adopted. Comparatively speaking, wet chemical methods are low cost, less hazardous, and thus capable of easy scaling up, compatible with most of substrates and occur at lower temperature for the fabrication of the desired ZnO. In addition, there are a variety of parameters that can be tuned to effectively control the morphologies and properties of the final products and thus have been demonstrated as a very powerful and versatile technique for growing ZnO nanostructures [5, 6].

Recently, sol gel and ultrasonic spray pyrolysis techniques have gained much interest compared to other techniques for ZnO thin films growth. In this approach, morphological and structural characteristics of the grown ZnO nanostructures can be controlled by adjusting the growth process parameters, such as the reagent of interest, stoichiometry and temperature.

II.1.1 Sol gel method

The sol–gel method is one of the most widely used in the synthesis of ZnO nanostructures. Also known as chemical solution deposition, Sol Gel is a wet-chemical method commonly used in the field of materials science. This interdisciplinary science explores the synthesis and properties of different materials, covering the entire size scale encountered during processing, from the earliest stages through to the final desired product [7]. There is a recent trend in sol–gel deposition of different types of films such as transparent conducting oxide, ferroelectric, and light reflecting films as it has many advantages, for instance, the easy control over the film composition, sub-micron sized particles, low processing temperature and easy fabrication of a large area thin film at low cost [8,9].

In essence, the sol–gel process transforms the metal acetate or metal alkoxide based precursors into a gel and then converts it into the desired final product. Meanwhile, ZnO can be synthesized from diverse types of raw materials, which can affect the characteristics of the final product. Alkoxides, normally used as a precursor in the sol–gel process, are expensive and explosive materials. The metal salt zinc acetate dihydrate $[Zn(CH_3COO)_2.H_2O]$ is used as an alternative to alkoxides because its hydrolysis is easier to control. The process generally involves a succession of transformations, namely, hydrolysis of the molecular precursor, polymerization via successive bimolecular additions of ions, condensation by dehydration, nucleation and growth. The conversion of the wet, as-deposited film into the desired crystalline film is induced through controlled thermal processes. Typically hot plates in combination with a conventional furnace or a rapid thermal annealing (RTA) oven are employed for this transformation process for further densification or microstructure manipulation.

The properties of a particular sol–gel network are related to a number of factors that affect the rate of hydrolysis and condensation reaction, such as [10-12]:

- Nature of the precursor and its concentration,
- Type of solvent and the acidity of the medium,
- Type of additive species and their concentrations,
- Aging temperature and time of the early mixture,
- Method of coating of substrates and its speed,
- Nature of the substrate,
- Pre- and post-heat treatment of the materials.

A survey of the literature shows that all these parameters play a key role on the evolution of texture of zinc oxide films [13].

Generally coating solution can be deposited by a number of methods. *Spin* and *dip coating* in various modifications are the by far most frequently applied techniques. The *dip coating* represents the oldest commercially applied coating process and is an ideal method to prepare thin layers from chemical solutions since it is a low cost and waste-free process that is easy to scale up with a good control on thickness. In addition, it offers simplicity, low processing temperature, and the ability to coat complex shapes and patterns. The coating amount and thickness can be controlled by adjusting the concentration of suspension, the number of dips and the withdrawal speed. Heat treatment of coated substrate is often required to densify the coating layer, to increase coating-implant bonding, and eliminate porosity. For such reasons, it is becoming more and more popular not only in research and development laboratories, but also in industrial production. At first glance this coating method is rather simple, however a more detailed understanding of the microscopic processes during dip coating enables tailoring of the final film. The schematic of the dip coater used during this study is displayed in figure (II.1).

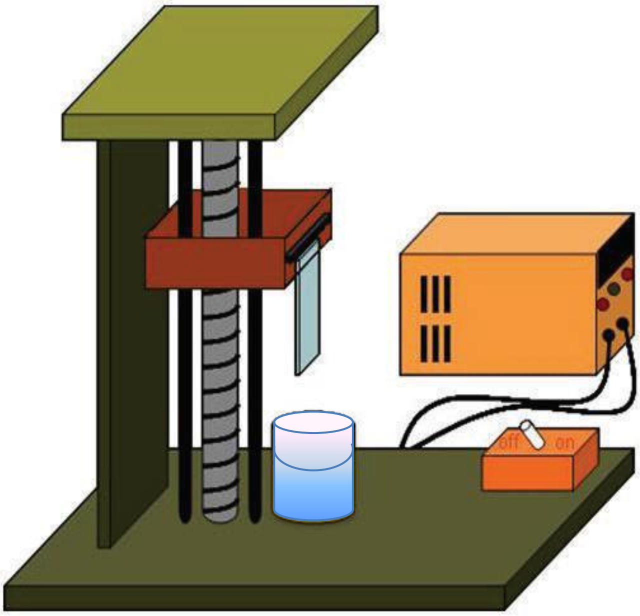

Figure II.1. *The schematic presentation of the dip-coater set up.*

Basically the dip coating process may be separated into three important technical stages (Fig.II.2):

1. Immersion and dwell time: The substrate is immersed into the precursor solution at a constant speed followed by a certain dwell time in order to leave sufficient interaction time of the substrate with the coating solution for complete wetting.

2. Deposition and Drainage: By pulling the substrate upward at a constant speed a thin layer of precursor solution is entrained and the excess liquid will drain from the surface.

3. Evaporation: The solvent evaporates from the fluid, forming the as-deposited thin film, which can be promoted by heated drying. Subsequently the coating may be subjected to further heat treatment in order to burn out residual organics and induce crystallization of the functional oxides [2, 14-16].

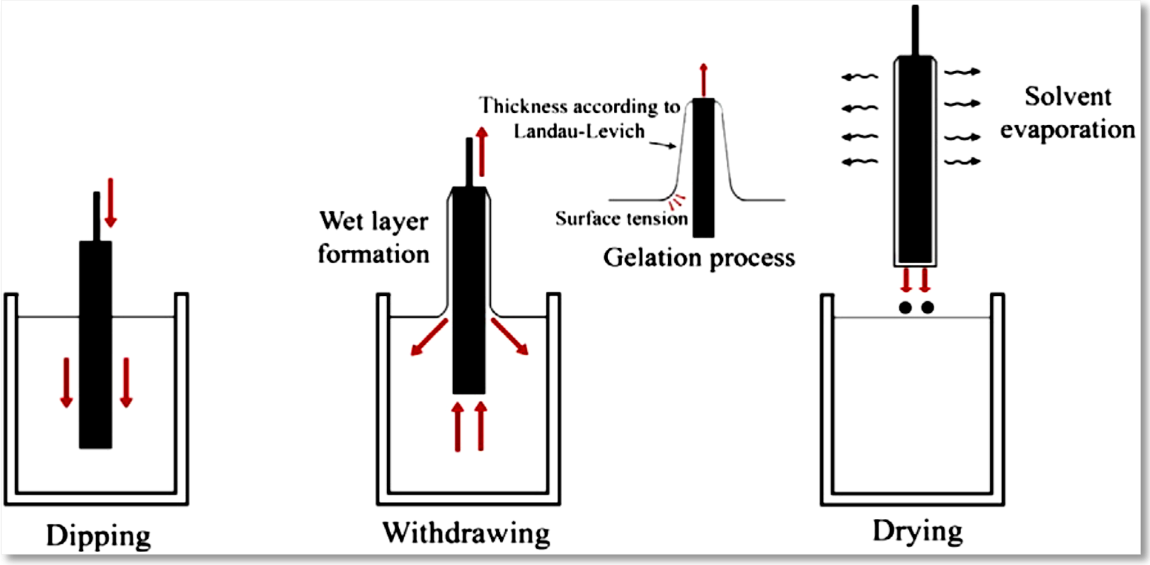

Figure II.2.*The main stages of the dip coating process.*

Figure II.3 shows schematically the microscopic processes which occur within the thinning film. Normally, the substrate is withdrawn vertically from the coating solution at a constant speed U_o. According to the streamlines in Fig.II.4, the moving substrate entrains the liquid in a fluid viscous boundary layer carrying some of the liquid toward the deposition region where the boundary layer splits in two. The inner layer moves upward with the substrate, while the outer layer is returned to the bath. Since the solvent is evaporating and draining, the entrained film acquires an approximate wedge-like shape that terminates in a well-defined drying line (x = 0). Above this vapor-liquid-solid three-phase boundary (drying line) the non-volatile species form the as-deposited layer which may be subjected to further drying.

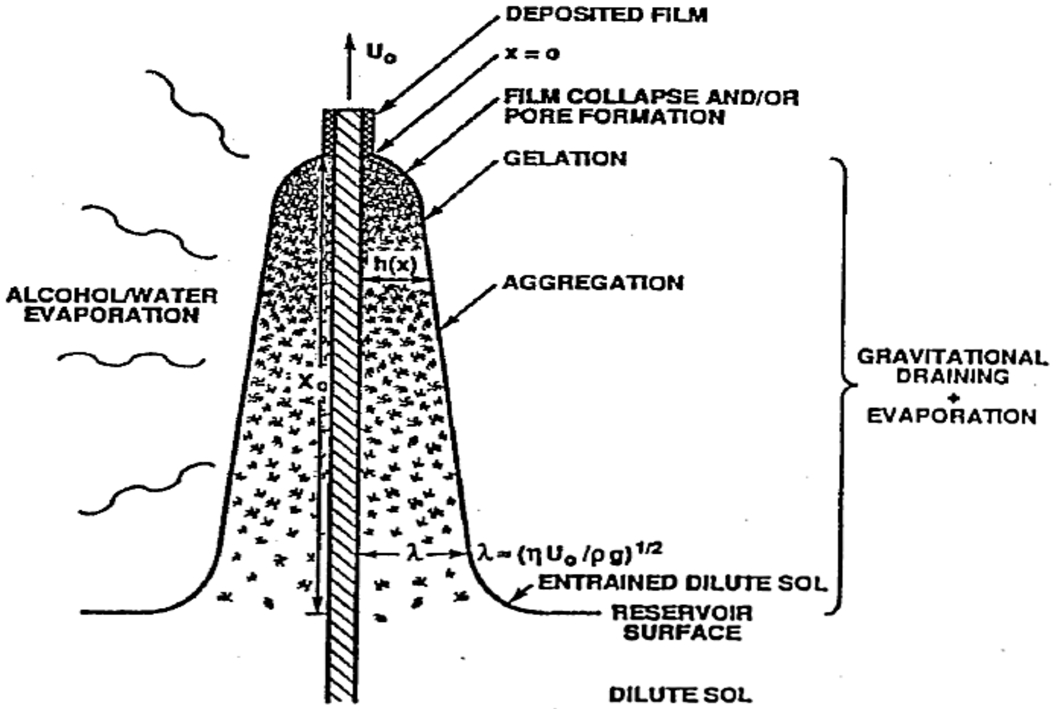

Figure II.3. *Mechanisms of a thin layer formation during dip-coating process.*

In order to model the thickness evolution during dip-coating several regimes have been taken into account. According to *Scriven* the entrained thickness h_0 of the deposited film is related to the position of the streamline dividing the upward and downward moving layers. In principle a competition between various forces in the film deposition region governs the film thickness and the position of the stream line; (1) viscous drag, (2) force of gravity, (3) capillary force (resultant force of surface tension in the concavely curved meniscus), (4) inertial force of the boundary layer liquid arriving at the deposition region, and (5) surface tension gradient. The viscous drag is the force moving liquid upward with the substrate and is proportional to liquid viscosity and withdrawal speed. Gravity acts to drive the liquid downwards. Surface curvature induced by surface tension at the base of the fluid capillary force lowers the pressure in the liquid beneath the curved meniscus near the solution bath and produces a driving force in the same direction as gravity.

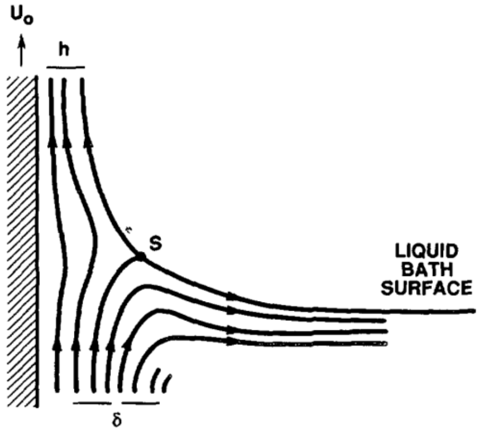

Figure II.4. *Detail of the flow patterns (streamlines) during the dip-coating process.*

- When the liquid viscosity η and withdrawal speed U_0 are high enough to lower the curvature of the meniscus, then the deposited film thickness h_0 is that which balances the viscous drag (ηU_0) and gravity force (ρg) according to:

$$h_0 = c_1(\eta U_0 / \rho g)^{1/2} \qquad \text{(II.1)}$$

where ρ is the liquid density, g is the acceleration of gravity and the constant c_1 is about 0.8.

- When the substrate speed and liquid viscosity η are not high enough, as is often the case for sol-gel film deposition, this balance (Eq.II.1) is modulated by the ratio of viscous drag to liquid-vapor surface tension γ_{LV}, according to the relationship derived by *Landau* and *Levich* [17-20]:

$$h_0 = 0.94\frac{(\eta U_0)^{2/3}}{\gamma_{LV}^{1/6}(\rho g)^{1/2}} \qquad \text{(II.2)}$$

II.1.2 Ultrasonic spray pyrolysis method

For large-scale production, spray pyrolysis could be a useful alternative to the traditional methods for obtaining thin films of pure and doped oxides. This process combines simplicity, low cost and minimal waste production which could be of particular interest to the photovoltaic industry [21]. Spray pyrolysis is a simple non-vacuum technique that can be applied at ambient pressure and can be easily scaled up for large area deposition.

In a typical thin film deposition process, salts of zinc are dissolved in water or organic solvents with the addition of small amount of acetic acid which was found to be beneficial for the film formation as it increases the solubility of Zn salt, suppresses hydrolysis reactions causing insulating hydroxides $Zn(OH)_2$, and promotes the formation of zinc acetate complexes. The solution is then sprayed with an inert carrier gas onto a heated substrate. Droplets impact on the substrate surface, spread into a disk shaped structure, and undergo thermal decomposition. The shape and size of the disk depends on the volume of the droplet as well as the substrate temperature. Consequently, the film is usually composed of overlapping disks of metal salt being converted to oxide [22, 23]. Standard spray pyrolysis equipment consists of an atomizer, solution container, gas supplier, substrate heater, and temperature controller (Fig.II.5).

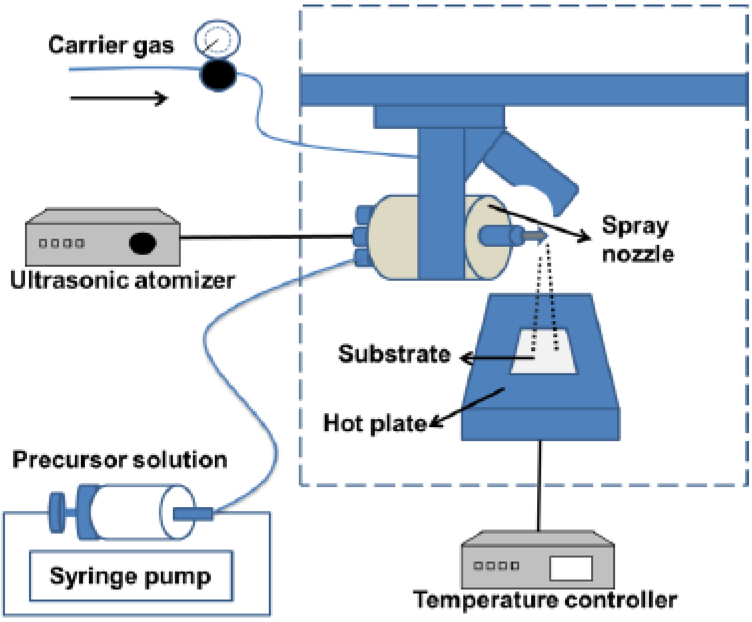

Figure II.5. *Schematic of the spray pyrolysis equipment.*

Two major disadvantages of conventional spray pyrolysis are related to particle morphology and phase homogeneity. This has largely been remedied by the introduction of ultrasonic nebulizers which are operated at a specific resonance frequency determined by the length of the nozzle thus producing a fine and homogeneous mist.

Ultrasonic spray pyrolysis (USP) is a thermal deposition based on droplet generation from liquids by ultrasound waves using an ultrasonic nozzle. It involves materials deposition by carrying the so-produced liquid droplets into a heated zone where the droplets undergo evaporation, decomposition, reaction into new products, and condensation of the new product onto a substrate. Ultrasonic atomization has the advantages of low cost, simple and continuous operation, high purity, narrow drop size distribution and hence uniform particle size distribution, controllable size from micrometer to submicrometer and excellent control of chemical uniformity and stoichiometry in a mixed oxide system [11, 24-27].

Many processes occur either sequentially or simultaneously, when a droplet hits the surface of the substrate, for these to be modelled in a straightforward manner. Many models exist for the decomposition of a precursor. Most of the authors suggest that only a kind of Chemical Vapor Deposition (CVD) process gives high quality films by spray pyrolysis [23,28]. This is because according to the CVD definition, chemical precursor must be in the form of chemical vapor that undergo chemical reactions. Whether or not the process can be classified as CVD depends on whether the liquid droplets vaporize before reaching the substrate or react on it after splashing. Mainly, the generated droplets will undergo four possible deposition mechanisms depending on the deposition/substrate temperature as shown in Fig. II.6:

- *Process I*, the lowest temperature regime, the droplet splashes on the substrate, vaporizes, and leaves a dry precipitate in which decomposition occurs.
- *Process II*, at higher temperatures, the solvent evaporates completely during the flight of the droplet, before the droplet reaches the surface, and dry precipitate impinges upon the surface and undergoes chemical reactions to yield the desired materials.
- *Process III*, at even higher temperatures, the solvent vaporizes while the droplet approaches the substrate, then the solid precipitate melts and vaporizes (or sublimes) and the vapor diffuses to the substrate to undergo a chemical reaction there. This mechanism is similar to the CVD deposition process, which tends to produce dense films with excellent coating adhesion.
- *Process IV*, as the deposition/substrate temperature is very high, the decomposition and/or chemical reaction occur in the vapor phase, the metallic compound vaporizes before it reaches the substrate and consequently the solid particles are formed after the chemical reaction in the vapor phase leading to homogeneous nucleation, and hence, formation of stable fine particles in the gas phase, which are then deposited and sintered onto the heated substrate leading to the formation of porous films, with poor adhesion. Alternatively, the powders can be collected in the gas phase for the production of ultrafine powders [29-31].

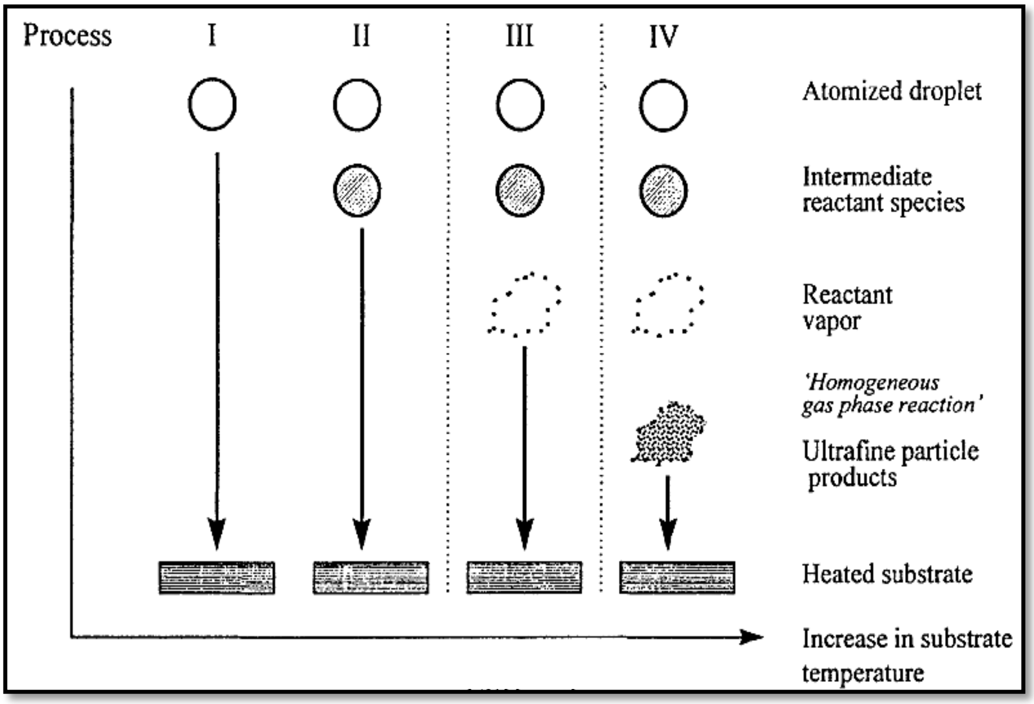

Figure II.6. *Description of the deposition processes initiated with increasing substrate temperature.*

In fact, the prime requisite for obtaining good quality sprayed thin film is the optimization of preparative conditions. These are: substrate temperature, spray rate, concentration of solution, type and pressure of the carrier gas, the geometric characteristics of the spray system etc. Generally, in a spray pyrolysis process, reaction temperature is a basic operating variable and as such optimization of the substrate temperature during the spray cycle is paramount. In addition, solution properties such as precursor composition and concentration may be crucial to achieve the desired product composition and morphology [32, 33].

II.2 Characterization techniques

Nanoscale characterization is a key field in nanoscience and technology as it provides fundamental understanding of the properties and functionalities of materials down to the atomic and molecular scale [34]. In general, characterization is based on the observation of materials' response to external excitation such as applying electrical bias, illuminating light, changing temperature, and so on [35]. In this work, a number of characterization techniques were employed to investigate the morphological, structural, electrical and optical properties of the grown samples. A brief description of the physical basis, usefulness and the experimental set-up of each technique are presented.

II.2.1 Atomic Force Microscope

Atomic force microscopy (AFM) is a crucial part of nanoscience. It has a great advantage in that almost any sample can be imaged in both air and liquids, such as the surface of a ceramic material, semiconductors, thin films, composites or a dispersion of metallic nanoparticles, or very soft, such as highly flexible polymers. The AFM, also referred to as the scanning force microscope (SFM), is part of a larger family of instruments termed the scanning probe microscopes (SPMs). The common factor in all SPM techniques is the use of a very sharp probe, which is scanned across a surface of interest, with the interactions between the probe and the surface being used to produce a very high resolution image of the sample, potentially to the sub-nanometer scale, depending upon the technique and sharpness of the probe tip.

In the case of the AFM (Figure II.7) a flexible cantilever with a sharp tip is moved over a sample surface probing the repulsive and attractive forces which exist between the atoms of the probe and the sample surface leading to the cantilever deflection. A highly position sensitive photodetector monitor the change in the path of a beam of laser light deflected from the upper side of the end of the cantilever and converts the signal to a three-dimensional topographic image of the surface [36-38].

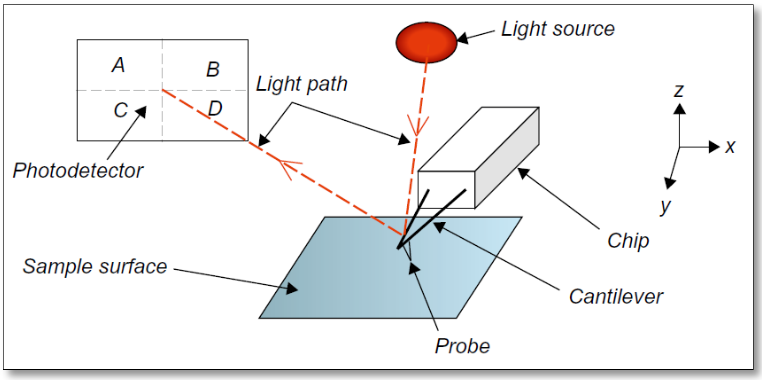

***Figure II.7**. Basic AFM set-up.*

Two scanning modes are commonly used in AFM measurements; the contact mode and the non-contact mode. In the case of the contact mode, where the probe remains in constant contact with the sample, the magnitude of the cantilever deflection can be precisely measured by shining a laser beam on the back of the tip and continuously monitoring the reflected beam changes which can be directly related to the deflection magnitude. Therefore, the cantilever displacements can be converted into electrical signals and then processed for creating an image. However, for the non-contact mode, where the cantilever may be oscillated, the cantilever is mechanically vibrated utilizing a piezoelectric crystal. The oscillated tip is systematically scanned over the surface of the sample and the oscillation is monitored where any change in the oscillation wave properties such as frequency, amplitude or phase is attributed to the surface features and hence topographical images can be created [39, 40].

In this work, the surface topography images and roughness values of the studied samples were determined using an AFM (Fig.II.8), MFP-3D Asylum Research with a Herzan TS-150 active vibration isolation table with lateral resolution of ~ 0.1 nm which is available at the Department of Process Engineering of the Algerian university Ferhat Abbas-Setif 1.

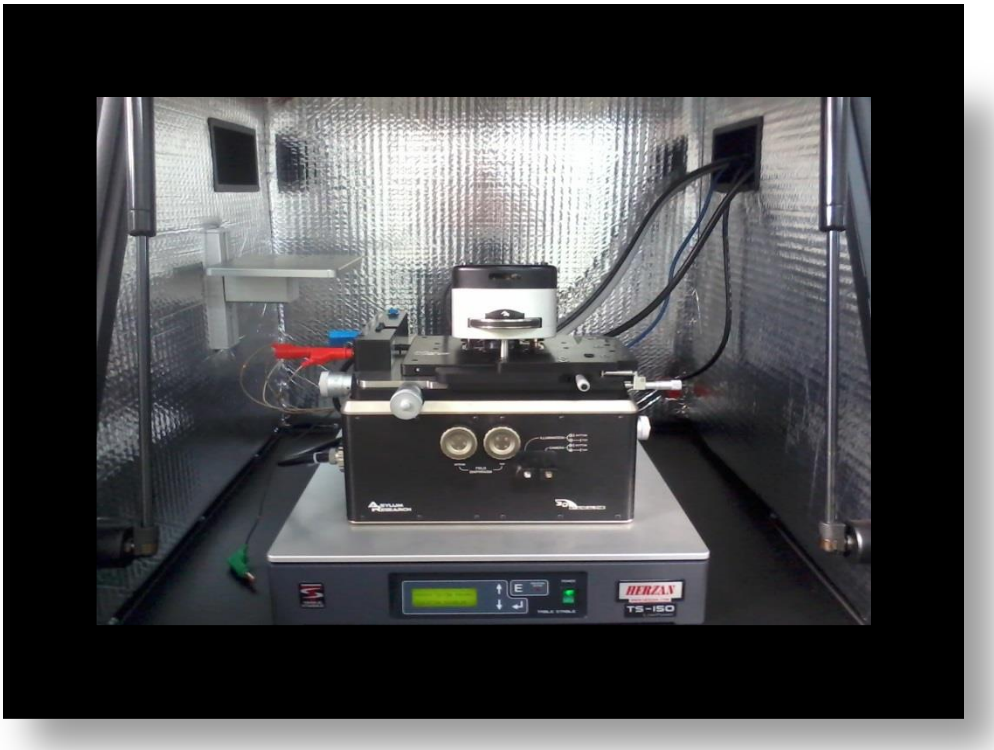

Figure II.8. *The AFM equipment.*

II.2.2 Scanning Electron Microscope

Morphology characterization techniques vary in both cost, resolution and the type of the obtained information. When higher resolution is required, advanced microscopic techniques can be used [4]. The electron microscope is a basic tool in several branches of science. The desire for greater spatial, temporal, and energetic resolution requires that the point electron source of the electron microscope generate a brighter, more temporally coherent and stable electron beam for illumination [41]. The scanning electron microscope (SEM) is undoubtedly one of the most useful and versatile instruments for the investigation of surface topography and morphology images producing high resolution with magnification extending to the nanoscale. The SEM must be operated under high vacuum conditions to reduce the number of collisions between the electron beam and the atmosphere in the sample chamber. Figure II.9 depicts a cross-section view for an SEM set-up showing its important components.

To create SEM image, the incident electron beam, known as primary electrons, is scanned across the sample surface and interaction between the electrons and the sample gives rise to different signals (the emission of electrons and photons). In fact, when a beam of electrons impinges the surface of a specimen each individual incident electron will go through a scattering effect. Secondary electrons are produced due to the interaction of the primary electron beam and the imaged area of the specimen. The emitted electrons are detected at each position in the scanned area by an electron detector which when gathered and analyzed bring together the image of the surface of the observed sample. There are two modes of imaging either by using Secondary Electrons or Backscattering Electrons. Secondary electron imaging provides high resolution imaging of fine surface morphology and for this the samples must be electrically conductive [42,43]. SEM typically requires the sample to be modified by depositing a conductive layer on the thin film to prevent charging effects, although significant advances have been made in low-voltage SEM to image dielectric surfaces without sample preparation [4,39].

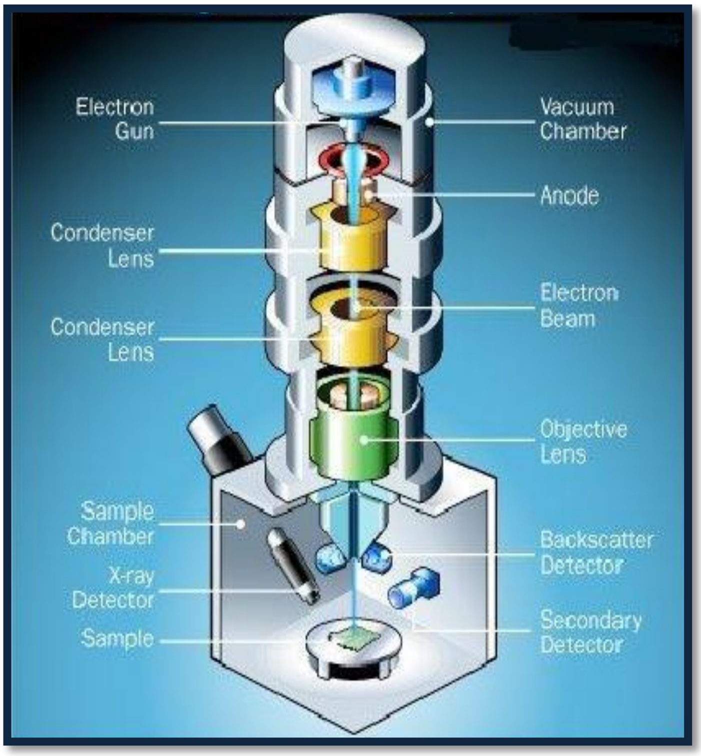

Figure II.9. *Schematic cross-section of a typical scanning electron microscope.*

The surface morphology and cross-sectional images of the thin films synthesized in this investigation were examined in Cenimat institute of Portugal using an SEM (Carl Zeiss AURIGA CrossBeam workstation) at an accelerating voltage ranging from 2 to 5 kv. This SEM (Fig.II.10) has a precise focused ion beam (FIB) feature which is valuable in etching and cutting cross-sections of the sample.

Figure II.10. *The scanning electron microscope equipment.*

II.2.3 Energy Dispersive Spectroscopy

Energy-dispersive spectroscopy (EDS or EDX) is an analytical technique, mostly incorporated in electron column instruments, used for the elemental analysis or chemical characterization of a sample. Its characterization capabilities are due in large part to the fundamental principle that each element has a unique atomic structure allowing X-rays that are characteristic of the element's atomic structure to be identified uniquely from one another. During EDS analysis, the specimen is bombarded with an electron beam inside the SEM. The bombarding electrons collide with the specimen atoms own electrons. A position vacated by an ejected inner shell electron is eventually occupied by an electron from one of the higher energy shells releasing an X-ray photon with energy equal to the energy difference between the two levels involved. The X-ray released by the electron is then detected by a solid state detector and converted into signals which are processed into an X-ray energy spectrum. Thus, by measuring the amounts of energy present in the X-rays being released by a specimen during electron beam bombardment, the identity of the atom from which the X - ray was emitted can be established. Characteristic x-rays from each element are used to determine the concentrations of the different elements in the specimen. Each of these peaks is unique to an atom and therefore corresponds to a single element. The higher a peak in a spectrum, the more concentrated the element is in the specimen [44].

In the present investigation, elemental analysis of the films was carried out using an X-MAX 150 energy dispersive X-ray spectrometer incorporated in the SEM column.

II.2.4 X-ray diffraction (XRD)

Structural characterization plays an essential role for growth-correlated properties of low-dimensional semiconductor structures [45]. Materials are made of atoms. Knowledge of how atoms are arranged into crystal structures and microstructures is important for understanding of the synthesis, structure and properties of materials. There are many different methods for measuring structure, but the more powerful experimental techniques involve diffraction. To date, most of our knowledge about the spatial arrangements of atoms in materials has been gained from diffraction experiments.

Diffraction experiment involves probing a crystal with x-ray radiation having a wavelength (λ) close to the crystal lattice spacing, as shown in fig.II.11 [46]. An incident wave is directed into a material and a detector is typically moved about to record the directions and intensities of the outgoing diffracted waves. Constructive or destructive interference then occurs along different directions as scattered waves are emitted by atoms of different types and positions [47]. An x-ray diffractive peak will only be detected if the following equation is satisfied:

$$n\lambda = 2d\sin\theta \tag{II.3}$$

This is the basis of *Bragg's law*, which relates the spacing between the 'planes' of atoms from which diffraction is occurring (d) to the angle (θ) at which the incident beam must probe the plane to give constructive interference.

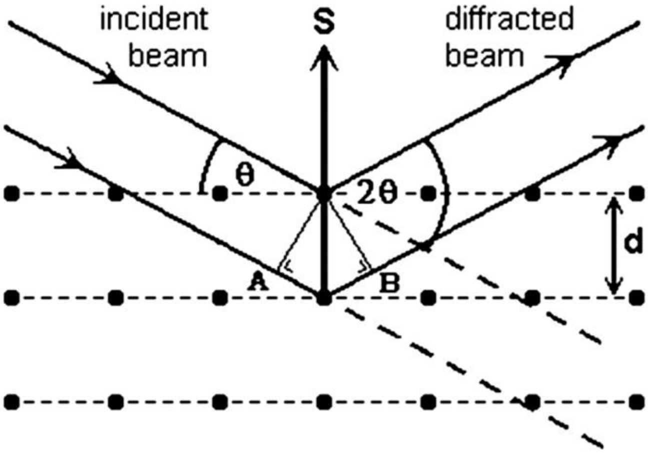

Figure II.11. *Schematic of x-ray diffraction illustration of the conditions required for Bragg diffraction to occur.*

Experimentally the generated XRD pattern of the sample is compared with a standard XRD powder pattern 'Joint Council Powder Diffraction Standards (JCPDS)' which gives information of different crystallographic phases and preferred orientations. From the width of the diffraction peak, average crystallite size in the film can also be estimated using the Scherrer's formula [48]:

$$D = \frac{0.9\lambda}{\beta\cos\theta} \tag{II.4}$$

Where D, θ and λ are the mean crystallites size, the Bragg angle and the wavelength of the incident X-ray, respectively. β, in radians, is the Full-Width at Half Maximum (FWHM) of the diffraction peak.

The lattice parameters *a* and *c* of the hexagonal systems can be calculated using the following relation:

$$\frac{1}{d_{hkl}^2} = \frac{4}{3}\frac{h^2 + k^2 + hk}{a^2} + \frac{l^2}{c^2} \tag{II.5}$$

where the Miller indices (*h k l*) are identified from the standards [47].

The samples studied in this work were crystallographically analysed using a BRUKER D8 FOCUS X-ray diffractometer of the UTBM University of France operating at 35 kV and 40 mA using Co-Kα radiation (1.78897 Å). The diffraction patterns were collected over 25–100° with a step size of 0.02°. In addition a PANalytical X'Pert PRO MPD (Fig.II.12) X-ray diffractometer fitted with an X'Celerator detector available at CEMOP/CENIMAT institute of Nova De Lisboa university of Portugal was also used to assess the crystallographic analysis of the samples. In this case, diffraction data were acquired by exposing samples to Cu-K_α X-ray radiation, which has a characteristic wavelength (λ) of 1.54060 Å. X-rays were generated from a Cu anode supplied with a voltage of 45 kV and current of 40 mA. The data were collected over a 2θ range of 10–89° with a step size of 0.03°.

Figure II.12. *The X-ray diffractometer.*

II.2.5 UV –Visible spectroscopy

UV-visible spectrophotometry is simple, fast and relevant mature analytical technique, from which numerous procedures have been developed [49] devoted to an optical characterization of a material for its application. The optical characterization is mainly of three kinds: absorption, transmittance and photoluminescence. Optical transmission measurements are generally performed to determine and evaluate some optical constants (such as absorption coefficients and bandgap energy) of materials which are considered important in the fabrication and analysis of devices. During transmission measurement the comparative photometry principle is used where a beam of light is systematically passed alternately through a reference compartment and a sample compartment and the intensity ratio of the sample-to-reference gives the sample’s transmittance.

The transmitted light is continuously recorded as a function of the incident wavelength thus a transmission spectrum is generated by plotting the relative intensity of the transmitted light to the incident light as a function of the wavelength. From the transmission data the optical bandgap *Eg* can be easily determined using the Tauc relation which is given by [39]:

$$(\alpha h\nu)^2 = B(h\nu - E) \tag{II.6}$$

where h is Planck’s constant, ν is the frequency of the incident photons and B is a constant which depends on the electron–hole mobility. Optical band gap can be determined using the $(\alpha h\nu)^2$ versus hν plot by extrapolating the linear portion of the curve to hν axis[43].

In this work, transmission spectra were obtained at room temperature using the Lambda 950 UV/VIS/NIR high-performance double-beam dual monochromator spectrometer (Fig.II.13) at the CEMOP/CENIMAT institute and the UV–vis–NIR double beam spectrophotometer (UV-1800 PC, Shimadzu) at the Department of Process Engineering of UFAS of Algeria. The sample was placed in the sample beam path and a reference sample was placed in the reference compartment. The sample and the reference were aligned so that the light passed through the centers of the apertures into the detectors (photodiodes).

Figure II.13. *Double-beam UV-Vis spectrophotometer.*

II.2.6 Photoluminescence (PL)

Optical measurement can be described as the study of the interaction between material and radiated energy in the form of light which can be observed in various phenomena. Among diverse optical phenomena, luminescence, radiation of light by external excitation, is the subject of luminescence characterization.

Luminescence characterization is nondestructive, nonintrusive, versatile and sensitive to the presence of defects or impurities in materials. Additionally, it can provide superior spatial, spectral, and temporal resolution. There have been many kinds of luminescence measurements. Generally the method of excitation, the prerequisite of luminescence, has been used for classification of luminescence measurement [35]. In case the excitation source is light, typically laser or monochromatic beam, the process is called photoluminescence (PL). It is a result of incident-photon absorption that generates electron–hole pairs and produces emission of a photon of a different wavelength [50]. The generated electron and hole tend to return to their ground state by giving up the excess energy through recombination. Before recombination, the generated carriers (electrons and holes) experience various processes such as diffusion, drift, scattering, exciton formation, and so on. If the generated carriers give up their energy in the form of light, the recombination is called radiative recombination (Fig.II.14). Otherwise, if the generated carriers lose the excess energy in the form of heat, the process is called nonradiative recombination. Luminescence measurement investigates radiative recombination in materials. This emitted light is detected as photoluminescence, and the spectral dependence of its intensity provides information about the properties of the materials.

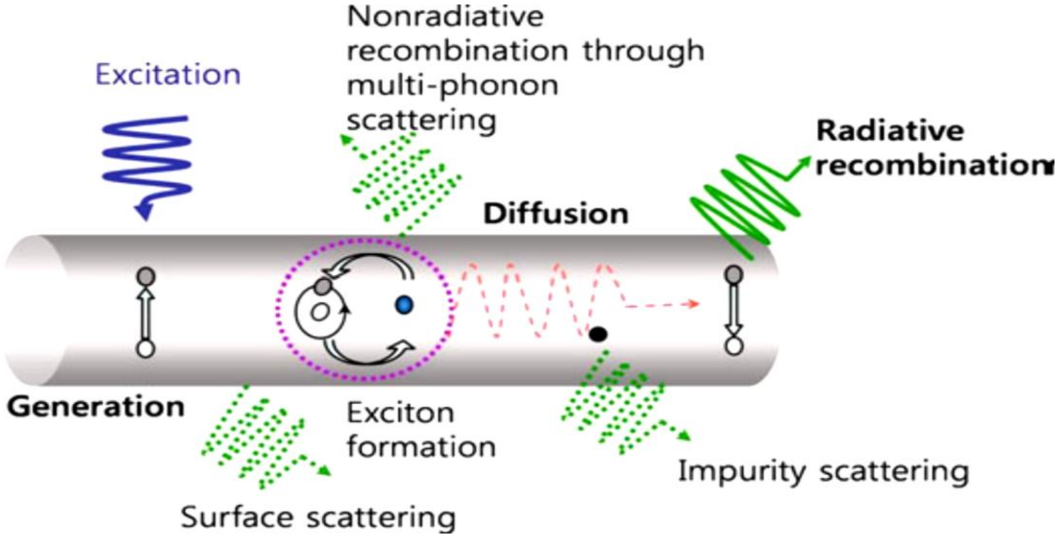

Figure II.14. *Optical processes in a semiconductor nanostructure*.

Luminescence is not only the basic principle of light emitting diodes, but also contains essential information on electronic band structure and carrier dynamics in semiconductors. Since electronic band structure and carrier dynamics are affected by structures and defects of semiconductors, luminescence spectroscopy is very useful to study the energy levels within band gap, formed by defects and external excitation [35].

Emissions are mainly intrinsic and extrinsic. Intrinsic luminescence is further divided into *band to band luminescence*, *exciton luminescence* and *cross luminescence*. In *band-to-band luminescence*, the emission occurs when an electron in the conduction band recombines with a hole in the valence band. This emission can be observed in very pure crystal at higher temperatures while at lower temperature this gets transformed in to *exciton luminescence*. If there are some impurities having their levels in the forbidden gap, electrons or holes are trapped by them and these recombine with each other via such levels, either radiatively or nonradiatively. *Cross luminescence* is usually observed in alkaline and alkaline earth halides. Luminescence caused by intentionally incorporated impurities (in most cases metallic impurities) is classified as *extrinsic luminescence*. In semiconductors, most important impurities are donors and acceptors that control semiconductor property and these can also act as luminescence activators [43]. A typical PL apparatus is shown in Fig.II.15. Generally the

Pl apparatus is composed of a light source for excitation, a sample holder, a dispersive element (grating monochromator), an optical detector sensitive to the dispersed light, optical cryostat, filters, and collecting lenses [50].

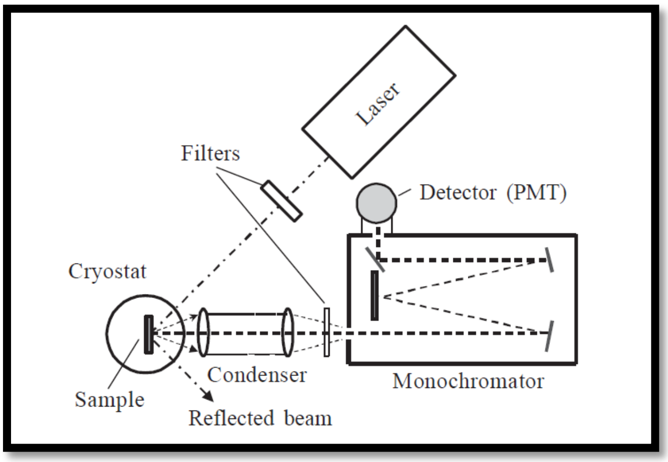

Figure II.15. *Schematic representation of a typical PL setup.*

In this study, photoluminescence spectra were measured at room temperature using a PerkinElmer LS 55 Luminescence spectrometer, available at the CEMOP/CENIMAT institute, which offers flexibility, versatility, reliability and ease-of-use. The monochromator based LS 55 uses a high energy pulsed Xenon source for excitation.

Figure II.16. *PerkinElmer LS 55 Luminescence spectrometer.*

II.2.7 Electrical characterization

When the resistance of a device is low, cable resistances may distort the measurement. In that case it is best to revert to a four-point probe (Figure II.17). The *van der Paw* four-point measurement is a popular technique which eliminates the effect of cable resistances. The current (I) passes by the outside two electrodes *A* and *D* and currents are not altered by cable resistance and this makes the value of the current well known. Since the current cannot disperse anywhere, it also passes between any two cross-sections in between *A* and *D*, for instance the points *B* and *C*. A voltage probe connected to these points does not tap the current, and no voltage drop occurs inside the cables connected to *B* and *C*. The voltage (V) drop between *B* and *C* is therefore accurately known. Since also the current between *B* and *C* is accurately known, the resistance (R) can be calculated with high precision, namely:

$$R = (V_B - V_C) / I_{AD} \qquad \text{(II.7)}$$

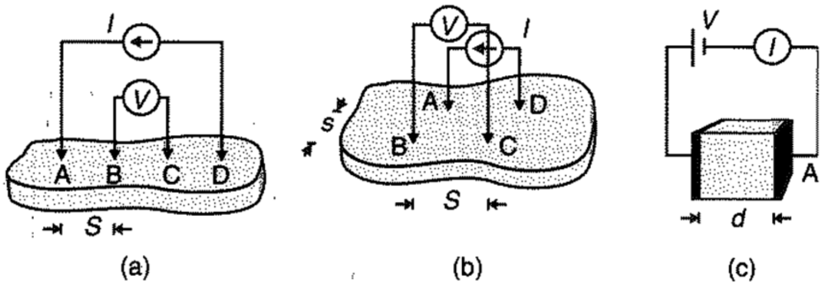

Figure II.17. *Four-point measurement of conductivity.*

To convert this to the material parameters resistivity (ρ, unit : Ω cm) or conductivity (σ, unit: S cm^{-1}) for a slab of material with infinite dimensions, the following relation can be used:

$$\rho = R \times 2\pi s \qquad \text{(II.8)}$$

Where *s* is the distance between two adjacent (equidistant) in-line electrodes. The electrodes can also be placed in a square configuration (Fig.II.18) in which case the relation between resistance and resistivity is:

$$\rho = R\frac{2\pi s}{2-\sqrt{2}} \qquad \text{(II.9)}$$

For finite samples a correction factor has to be introduced. In case the film is very thin and effectively two-dimensional conductivity takes place, the finite-sample correction factor for the square configuration, with the distance between the electrodes *s* much larger than the film thickness *d,* becomes:

$$\rho = \frac{\pi}{\ln 2} R d \qquad \text{(II.10)}$$

Reversing this equation shows that the measured resistance R is independent of the inter-electrode distance *s*. It is customary to express the resistance of a thin film in units Ω/□, which is read as Ω per square, the "square" being a dimensionless unit but indicating that the resistance was measured in a square configuration. The product *R* and *d* is referred to as sheet resistance and Eq.II.10 can be used to convert sheet resistance to resistance and resistivity.

Moreover, when a current-carrying conductor is placed in a magnetic field, a voltage is generated in a direction perpendicular to both the current and the magnetic field. This observation, known as *Hall Effect*, arises from the deflection of charge carriers to one side of the conductor to produce an electrical surface charge as a result of the magnetic (Lorentz) force they experience. Therefore, a potential drop across the sample called Hall voltage is formed. The induced Hall electric field develops to oppose the Lorentz force. The carriers tend to be deflected by the Lorentz force, since no current is allowed in the transversal direction. Measuring this potential V_y yiels the Hall mobility:

$$\mu_H = \frac{V_y d}{B_z V_x b} \qquad \text{(II.11)}$$

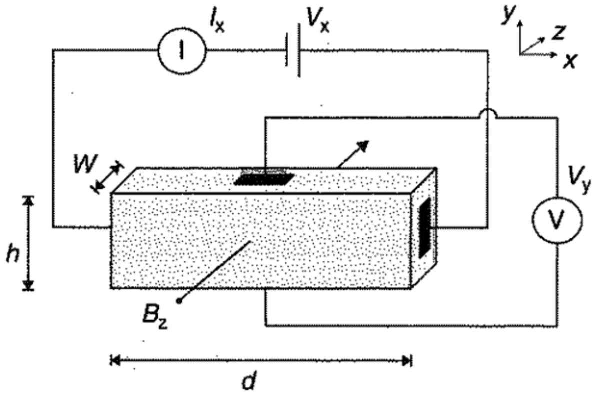

Figure II.18.*The Hall measurement principle.*

Where *b* is the height of the sample, the size in the y-dimension, perpendicular to the current and magnetic field, and *d* its length, the size in the current direction x.

The problem with Hall measurements is that for small mobilities, like most amorphous materials, the quantity V_y becomes very small, up to the point of being immeasurable. As such, Hall measurements are only adequate for high-mobility materials [51, 52].

In this study, a HL5500PC Hall System with a 0.5 permanent magnet (Fig.II.2.5) was used to perform Hall measurements on the samples at room temperature. The van der Pauw method was applied for the measurements. The samples have square geometry with contact size to sample periphery ratio as low as possible. It enables measurement of resistivity, carrier concentration and mobility on a wide range of semiconductors and with minimum effort in sample preparation. It is designed as a modular system and the basic instrument can measure sheet resistivities up to a few MOhm/square and Hall voltages of a few μV. Before electrical measurement, samples were cut into squares and silver metal ohmic contacts performed and tested prior to any measurement.

Figure II.19. *HL5500PC Hall Effect System.*

II.3 References

[1] A. B. Panda, G. Glaspell, M. S. El-Shall, Microwave synthesis and optical properties of uniform nanorods and nanoplates of rare earth oxides. *J. Phys. Chem. C* 111(5) (2007) 1861-1864.

[2] D. Grosso, How to exploit the full potential of the dip-coating process to better control film formation. *J. Mater. Chem.* 21(43) (2011) 17033-17038.

[3] R. Zhang, H. A. Andersson, M. Andersson, B. Andres, H. Edlund, P. Edström, S. Edvardsson, S. Forsberg, M. Hummelgård, N. Johansson, K. Karlsson *et al*. Soap-film coating: High-speed deposition of multilayer nanofilms. *Sci. Rep*, 3. 1477; DOI: 10.1038/srep01477 (2013).

[4] N. Kaiser, H. K. Pulker, *Optical interference coatings*, Springer-Verlag Berlin Heidelberg, (2003).

[5] S. Xu, Z. L. Wang, One-dimensional ZnO nanostructures: solution growth and functional properties. *Nano Res*. 4 (11) (2011)1013-1098.

[6] S. K. Arya, S. Saha, J. E. Ramirez-Vick, V. Gupta, S. Bhansali, S. P. Singh, Recent advances in ZnO nanostructures and thin films for biosensor applications: review. *Anal. Chim. Acta* 737 (2012) 1-21.

[7] L. Spanhel, M. A. Anderson, Semiconductor clusters in the sol-gel process: quantized aggregation, gelation, and crystal growth in concentrated zinc oxide colloids. *J. Am. Chem. Soc.* 113 (8) (1991) 2826-2833.

[8] S. Bandyopadhyay, G. K. Paul, S. K. Sen, Study of optical properties of some sol–gel derived films of ZnO. *Sol. Energ. Mat. Sol. Cells* 71 (1) (2002) 103-113.

[9] R. Thirunakaran, A. Sivashanmugam, S. Gopukumar, R. Rajalakshmi, Cerium and zinc: dual-doped $LiMn_2O_4$ spinels as cathode material for use in lithium rechargeable batteries. *J. Power Sources* 187 (2) (2009) 565-574.

[10] M. Lin, Y. Zhao, S. Wang, M. Liu, Z. Duan, Y. Chen, F. Li, F. Xu, T. Lu, Recent advances in synthesis and surface modification of lanthanide-doped upconversion nanoparticles for biomedical applications. *Biotechnol. Adv*. 30 (6) (2012) 1551-1561.

[11] J. C. Fan, K. M. Sreekanth, Z. Xie, S. L. Chang, K. V. Rao, p-Type ZnO materials: theory, growth, properties and devices. *Prog. Mater. Sci.* 58 (6) (2013) 874-985.

[12] S. S. Alias, A. A. Mohamad, *Synthesis of zinc oxide by sol-gel method for photoelectrochemical cells*. Springer Singapore, (2014).

[13] L. Znaidi, Sol–gel-deposited ZnO thin films: a review. *Mater. Sci. Eng. B* 174 (1) (2010). 18-30.

[14] T. Schneller, R. Waser, M. Kosec, D. Payne, *Chemical solution deposition of functional oxide thin films,* Springer- Verlag Wien, (2013).

[15] M. F. M. Yusoff, M. R. A. Kadir, N. Iqbal, M. A. Hassan, R. Hussain, Dipcoating of poly (ε-caprolactone)/hydroxyapatite composite coating on Ti6Al4V for enhanced corrosion protection. *Surf. Coat. Tech*. 245 (2014) 102-107.

[16] A. Nickheslat, M. M. Amin, H. Izanloo, A. Fatehizadeh, S. M. Mousavi, Phenol photocatalytic degradation by advanced oxidation process under ultraviolet radiation using titanium dioxide. *J. Environ. Public Health*, 2013 (2013) 1-9.

[17] G. W. Scherer, C. J. Brinker, *Sol-gel science: the physics and chemistry of sol-gel processing,* Academic Press, inc, (1990).

[18] C. J. Brinker, G. C. Frye, A. J. Hurd, C. S. Ashley, Fundamentals of sol-gel dip coating, *Thin Solid Films,* 201 (1991) 97-108.

[19] C. J. Brinker, A. Hurd, Fundamentals of sol-gel dip-coating, *J. Phys.* III 4 (7) (1994) 1231-1242.

[20] P. Yimsiri, M. R. Mackley, Spin and dip coating of light-emitting polymer solutions: Matching experiment with modelling. *Chem. Eng. Sci.* 61(11) (2006) 3496-3505.

[21] M. Gabás, N. T. Barrett, J. R. Ramos-Barrado, S. Gota, T. C. Rojas, M. C. López-Escalante, Chemical and electronic interface structure of spray pyrolysis deposited undoped and Al-doped ZnO thin films on a commercial Cz-Si solar cell substrate. *Sol. Energ. Mat. Sol.Cells.* 93(8) (2009) 1356-1365.

[22] A. Crossay, S. Buecheler, L. Kranz, J. Perrenoud, C. M. Fella, Y. E. Romanyuk, A. N. Tiwari, Spray-deposited Al-doped ZnO transparent contacts for CdTe solar cells. *Sol. Energ. Mat. Sol. Cells.*101 (2012) 283-288.

[23] D. Perednis, PhD thesis, Thin film deposition by spray pyrolysis and the application in solid oxide fuel cells, Swiss Federal Institute of Technology Zurich, (2003).

[24] P. Arnou, J.W. Bowers, J. M. Walls, Aluminium-doped zinc oxide deposited by ultrasonic spray pyrolysis for thin flm solar cell applications, 40th IEEE Photovoltaic Specialists Conference (PVSC), Denver, USA, 8-13 June, (2014) 0308-0313.

[25] C. P. Li, PhD thesis, Ultrasonic spray deposition of mesoporous, nanocrystalline tungsten oxide films for smart windows, Colorado School of Mines. Arthur Lakes Library, (2007).

[26] K. Lu, N. Manjooran, M. Radovic, E. Medvedovski, E. A. Olevsky, C. Li, G. Singh, N. Chopra, G. Pickrell, *Advances in Nanomaterials and Nanostructures*, Vol.229, A John Wiley & Sons, Inc., (2011).

[27] B. W. Mwakikunga, Progress in ultrasonic spray pyrolysis for condensed matter sciences developed from ultrasonic nebulization theories since michael faraday. *Crit. Rev. Solid State Mater. Sci.* 39 (1) (2014) 46-80.

[28] D. Perednis, L. J. Gauckler, Thin film deposition using spray pyrolysis. *J. Electroceram.*

14(2) (2005) 103-111.

[29] J. C. Viguie, J. Spitz, Chemical vapor deposition at low temperatures. *J. Electrochem. Soc*.122 (4) (1975) 585-588

[30] K. L. Chopra, S. Major, D. K. Pandya, Transparent conductors—A status review. *Thin solid films* 102(1) (1983)1-46.

[31]Choy, K. L. Chemical vapour deposition of coatings. *Prog. Mater. Sci.* 48(2) (2003) 57-170.

[32] C. M. Muiva, T. S. Sathiaraj, K. Maabong, Effect of doping concentration on the properties of aluminium doped zinc oxide thin films prepared by spray pyrolysis for transparent electrode applications. *Ceram. Int.* 37(2) (2011) 555-560.

[33] P. S. Patil, Versatility of chemical spray pyrolysis technique. *Mater. Chem. phys.* 59(3) (1999) 185-198.

[34] A. T. Wee, *Selected topics in nanoscience and nanotechnology*. World Scientific Publishing Co. Pte. Ltd. (2009).

[35] G. C. Yi, *Semiconductor Nanostructures for Optoelectronic Devices: Processing, Characterization and Applications*. Springer-Verlag Berlin Heidelberg, (2012).

[36] K. Winkelmann, B. Bhushan, *Global Perspectives of Nanoscience and Engineering Education.* Springer International Publishing Switzerland, (2016).

[37] P. Eaton, P. West, *Atomic force microscopy,* Oxford University Press, (2010).

[38] Y. Li, PhD thesis, Development of ZnO-based thin film transistors and phosphorus-doped ZnO and (Zn, Mg) O by pulsed laser deposition, University of Florida, (2006).

[39] M. M. Almotari, PhD thesis, Fabrication and Characterisation of Zinc Oxide Thin Films Singly doped With Trace amounts of Rare Earth Materials, University of Canterbury, (2013).

[40] W. R. Bowen, N. Hilal, *Atomic force microscopy in process engineering: an introduction to AFM for improved processes and products*. 1st ed., Butterworth-Heinemann, Elsevier Ltd. (2009).

[41] X. H. Ji, Q. Y. Zhang, J. Q. Xu, Y. M. Zhao, Rare-earth hexaborides nanostructures: recent advances in materials, characterization and investigations of physical properties. *Prog. Solid State Chem.* 39(2) (2011).

[42] A. Nouailhat, *An Introduction to Nanosciences and Nanotechnology*, ISTE Ltd and John Wiley & Sons, Inc., (2008).

[43] T. V. Vimalkumar, PhD thesis, Highly conductive and transparent ZnO thin film using Chemical Spray Pyrolysis technique: Effect of doping and deposition parameters, Cochin University of Science And Technology, (2011).

[44] G. N. Dar, PhD thesis, *Metal Oxide Nanostructures and Their Applications*, University of Patras Greece, (2015).

[45] D. Bimberg, *Semiconductor nanostructures*. Springer-Verlag Berlin Heidelberg, (2008).

[46] M. A. Moram, M. E. Vickers, X-ray diffraction of III-nitrides. *Rep. Prog. Phys.* 72(3) (2009) 036502.

[47] B. Fultz, J. Howe, *Transmission Electron Microscopy and Diffractometry of Materials*, Springer-Verlag Berlin Heidelberg, (2013).

[48] B.D. Cullity, S.R. Stock, *Elements of X-ray diffraction*, 3rd ed. Pearson New International Edition, (2014).

[49] O. Thomas, C. Burgess, *UV-visible spectrophotometry of water and wastewater*, Vol. 27. Elsevier, (2007).

[50] H. Morkoç, Ü. Özgür, *Zinc Oxide, Fundamentals, Materials and Device Technology*, Wiley-VCH Verlag GmbH & Co. KGaA, (2009).

[51] P. Stallinga, *Electrical Characterization of Organic Electronic Materials and Devices*. John Wiley & Sons, (2009).

[52] S. Cristoloveanu, S. Li, *Electrical characterization of silicon-on-insulator materials and devices*, Vol. 305, Springer Science & Business Media, (1995).

Chapter III. Experimental details, results and discussions

The current chapter presents and discusses the main experiments and results of the thesis. The first part describes studies regarding the synthesis and characterization of well-crystalline ZnO and ZnO:RE thin films chemically deposited from precursor solutions via facile and simple sol gel process employing commonly used laboratory chemicals. Importantly, the fabricated ZnO:RE exhibited interesting optical properties. An introduction of defects and/or impurities in the crystalline network results in symmetry breakdown and consequently different band structures that would give rise to different optical properties. As the drive to reduce production costs and the desire to develop flexible, large-area electronics continues, the need for integrating cheap substrates in the device fabrication process cannot be over emphasized. Thus the second part demonstrates the successful growth of ZnO and ZnO:Al by ultrasonic spray pyrolysis method at low temperature. A special attention was given to the global parameters to better describe the physical properties of transparent conducting oxide thin films (TCO).

III.1 ZnO Thin film derived sol gel dip coating method

Chemical methods such as sol-gel techniques can conveniently provide control of nucleation, growth and aging of particles in the solution enabling the synthesis of the required precursor particles utilizing a variety of parameters allowing control of the solid formation process [1]. Also, it does not require the use of any catalyst or toxic precursors, making it a facile and environmentally friendly method.

Among those parameters, sol aging time and concentration are important parameters that can have remarkable impact on thin films properties. Moreover, the zinc oxide thin film properties can be easily tailored by using suitable impurity material. Therefore, it is of scientific interest to fine tune the deposition parameters in order to obtain good quality coatings using a simple process. In this section, we report synthesis route to produce pure and RE doped nanocrystalline ZnO thin films. To get a better understanding of the effect of sol aging time and concentration as well as RE ion concentration on the morphological, structural and optical properties of the deposited films, they have been systematically studied using scanning electron microscopy, atomic force microscopy, X-ray diffraction, UV-visible spectroscopy and photoluminescence.

III.1.2 *Sol aging time and concentration effect*

The work reported in this section is expanded and updated material that first appeared in reference [2].

III.1.2.1 Materials

For the preparation of ZnO sol, zinc acetate dihydrate [Zn $(CH_3COO_2.2H_2O]$ and methanol (CH_3OH) were used as starting materials. The glass slides (76×26mm) for substrates were from ISO-LAB (Germany).

III.1.2.2 Films preparation and processing

All chemicals purchased from Aldrich Chemical Corporation were of analytical grade and used as received without further purification. ZnO thin films were prepared by the sol–gel method. Zinc acetate dihydrate $(Zn(CH_3COO)_2 \cdot 2H_2O)$ was dissolved in methanol with different molar concentrations varying from 0.03 to 0.1 M under magnetic stirring, at 70°C for an hour, to be mixed thoroughly. After continuous stirring, homogeneous and translucent solutions were obtained, which indicated a complete dissolution of metal salt precursor. These solutions were then divided into four equal amounts and stored in four different beakers for each concentration. The beakers were labeled as A, B, C, and D corresponding to 0.03, 0.07, 0.09 and 0.1mol/l respectively. The final solutions were kept in the dark at room temperature to prevent possible light-assisted reaction that may affect the solution. An aliquot was taken each 0, 72, 168 and 312h for the films deposition (Table 1) from each solution. The sol remains transparent and no visible changes were observed when stored in darkness at room temperature for several weeks.

Prior to film deposition, the glass substrates were thoroughly cleaned, to avoid thin film contamination, with soapy water then properly cleaned in an ultrasonic cleaner using acetone and nitric acid. Afterwards, substrates were rinsed with distilled water for several times and subsequently dried at room temperature. Film deposition was carried out in air at room temperature by the dip-coating route onto the substrate with a withdrawal speed of 5 cm/min. They have been deposited from as-prepared as well as the sols aged for long time. After each dipping process, the films were dried immediately, to evaporate the solvent and remove organic residuals, on a hot plate at 170°C for 15 min and were held in the horizontal position to avoid draining of the transferred sol, which could lead to different thicknesses in the coatings. The procedures from coating to drying were repeated several times until the film reached the desired thickness. The samples were then inserted into a furnace and annealed at 500°C for an hour in the air with a heating rate of 5°C/min in order to crystallize them and remove unwanted organic materials from the surface.

The morphologies of the synthesized samples were analyzed by field emission scanning electron microscopy (FESEM) on a JEOL JSM-7800F microscope and atomic force microscopy (AFM) on MFP-3D Asylum Research microscope. The phase structure of ZnO thin films were analyzed by X-ray diffraction (XRD) technique. The measurements were performed on a BRUKER D8 FOCUS diffractometer operating at 35 kV and 40 mA using CoKα radiation ($\lambda = 1.78897$ Å). The diffraction patterns were collected over the range 25–100° with a step size of 0.02° and a step time of 33.50 s. The optical transmission spectra were measured in the range 200–900 nm using a UNICAM UV 300 as UV–visible spectrophotometer.

Table III.1. The microstructural properties of ZnO thin films as a function of sol aging time and concentration.

Sol	C (mol/l)	Aging time (hour)	2θ (deg.)	d(002) (Å)	FWMH (deg.)	D (nm)	Lattice parameters (Å)	
							c	a
A	0.03	as-prepared	-	-	-	-	-	-
	0.03	72	-	-	-	-	-	-
	0.03	168	40.35	2.593	0.510	19.26	5.186	2.994
	0.03	312	40.13	2.607	0.413	23.77	5.214	3.010
B	0.07	as-prepared	40.20	2.602	1.070	9.18	5.205	3.005
	0.07	72	40.32	2.595	0.585	16.79	5.190	2.996
	0.07	168	40.33	2.594	0.423	23.23	5.189	2.995
	0.07	312	40.29	2.597	0.351	27.99	5.194	2.998
C	0.09	as-prepared	40.39	2.590	0.740	13.28	5.181	2.991
	0.09	72	40.29	2.597	0.398	24.68	5.194	2.998
	0.09	168	40.36	2.592	0.376	26.13	5.185	2.993
	0.09	312	40.31	2.595	0.357	27.52	5.191	2.997
D	0.1	as-prepared	40.33	2.594	0.705	13.93	5.189	2.995
	0.1	72	40.34	2.594	0.424	23.17	5.188	2.995
	0.1	168	40.39	2.590	0.300	32.76	5.181	2.991
	0.1	312	40.35	2.593	0.284	34.60	5.186	2.994

III.1.2.3 Results and discussions

III.1.2.3.1 Chemical reactions

The growth of ZnO thin films from zinc acetate dihydrate precursor using sol–gel process generally undergoes four stages, such as solvation and formation of methoxyacetate complexes, hydrolysis (by water originating from $Zn\ (Ac)_2\cdot 2H_2O$ itself), polymerization of the complexes and transformation into ZnO. The size and activity of solvent have obvious influence on the reacting progress and product. Methanol has smaller size and a more active –OH and –OCH_3 groups. It can react more easily to form a polymer precursor with a higher polymerization degree, which is required to convert sol in to gel.

The dissolution of zinc acetate dihydrate accompanies solvation of zinc and acetate ions by methanol (MeOH). Hydrated water molecules form hydrogen bonding with MeOH. The kinetics of hydrolysis and polymerization are greatly influenced by water concentrations in the solutions. The zinc ion has a solvation number of six and forms an octahedral inner coordination sphere, $[Zn\ (MeOH)_6]^{2+}$.

Thus the reaction scheme is invoked as:

$$\left[Zn\left(MeOH\right)_6\right]^{+2} + mMeOH + Ac^- \leftrightarrow \left[Zn\left(MeOH\right)_{5-m}\left(MeO\right)_m Ac\right]^{1-m} + mMeOH_2^+ + MeOH \qquad \text{(III.1)}$$

The formation of the methoxyl group is due to the enhanced acidity of the solvating MeOH causing the deprotonation by free MeOH. A reaction between the methoxyacetate complexes and water is considered. The water concentration in the solution does not exceed double of the zinc concentration because water was supplied only from the starting material. Therefore the hydrolysis reaction is expected to proceed considerably slowly. At lower water concentrations, water acts as a nucleophilic reactant. The nucleophilic substitution with a leaving group of MeOH and/or CH_3COOH leads to hydrolysis of the complexes;

$$\left[Zn\left(MeOH\right)_{5-m}\left(MeO\right)_m Ac\right]^{1-m} + (m+1)H_2O \leftrightarrow$$
$$\left[Zn\left(MeOH\right)_{5-m}\left(OH\right)_{m+1}\right]^{1-m} + mMeOH + AcH \qquad \text{(III.2)}$$

A polymerization reaction between mononuclear complexes generally occurs if at least one hydroxyl group is bounded to the metal ion. The first step of polymerization is the construction of an “ol” bridge in which a hydroxyl group is caught between the two metal ions. Writing the zinc hydroxide complex simply as Zn–OH, an olation reaction is expressed schematically by:

$$Zn-OH+HO-Zn \leftrightarrow Zn-(OH)-Zn+OH \qquad \text{(III.3)}$$

That is, “Zn (OH) Zn” bridges are formed by an olation reaction resulting in polynuclear zinc hydroxide clusters. When more than one hydroxyl group is brought to the complex, polymerization among the complexes proceeds, generating polynuclear zinc hydroxide clusters. Thus the “Zn O Zn” bonds are constructed and the complexes are finally transformed into solid ZnO [3-5] after annealing.

III.1.2.3.2 Structural characterization

The XRD spectra of the deposited ZnO films as a function of sol aging time and concentration are shown in Fig.III.1. The detailed XRD data analyses of representative films are summarized in Table III.1.

From XRD pattern, it can be seen that for the different sol concentrations, the as-prepared (without aging) films presented poor crystallinity or were nearly amorphous denoted by the weakness, or absence in some cases, of significant diffraction peaks. By increasing the sol aging time as well as concentration, narrower peaks with higher intensities are attained. The polycrystalline nature of the ZnO films clearly appears; all peaks have been indexed and were found to be in agreement with those of the hexagonal wurtzite phase of ZnO. Either peak position or peak intensity is in good agreement with the data from JCPDS card No. 00-036-1451. Moreover, no other peaks were detected, implying that the prepared nanostructured materials are pure ZnO. Also, the calculated lattice constants 'a' and 'c' of the prepared films (table III.1) were found to be close to those of pure bulk ZnO (a = 3.249 Å, c = 5.206 Å).

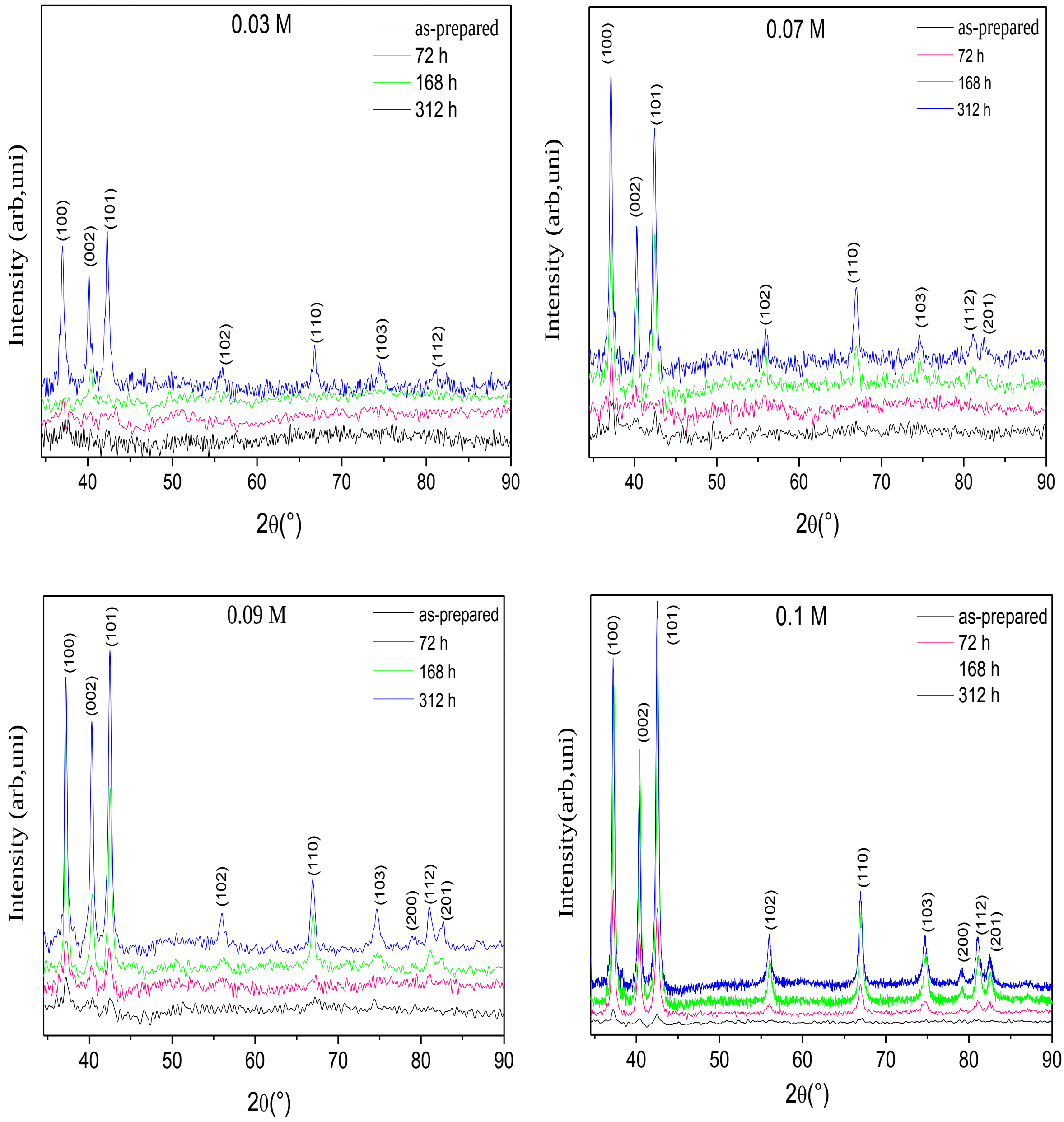

Figure III.1. *XRD pattern of ZnO thin films prepared from sols with different concentrations and aging time.*

From a general standpoint, it is evident that for the same aging time, different degrees of crystallinity could be reached regarding the sol concentration. Increasing precursor concentrations resulted in an increase of diffraction peak intensities and a faster growth rate. At a given concentration, with longer aging time, diffraction peaks became narrower with higher intensities. Meanwhile, the increasing of precursor concentration resulted in a decreased aging time being required for crystallization.

In order to better visualize differences between the prepared solutions and hence accurately determine the effect of sol concentration on the ZnO thin films, the XRD patterns of the as-prepared samples from different sol concentrations, are displayed in figure III.2.

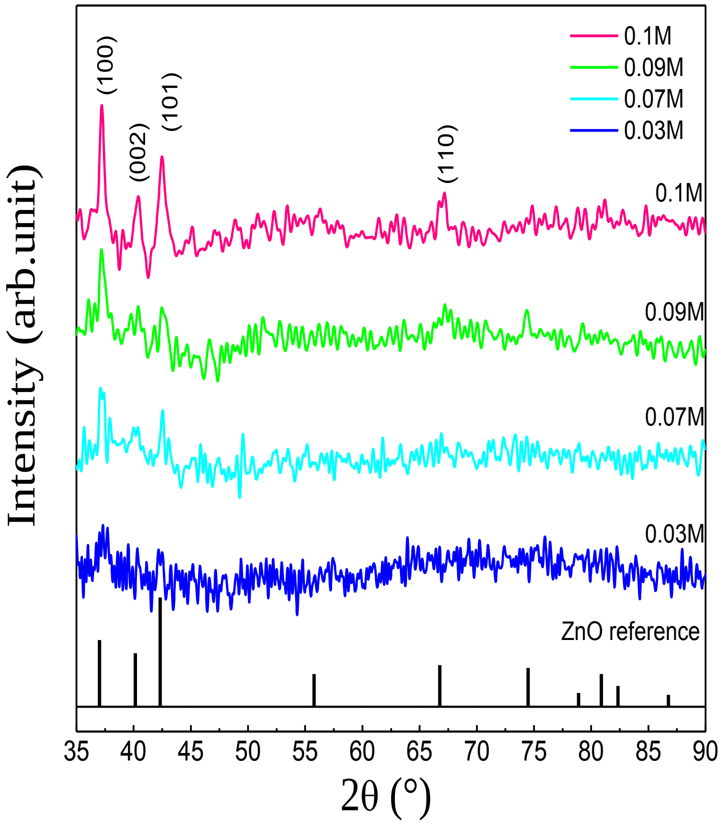

Figure III.2. *XRD patterns of ZnO thin films prepared from different sol concentration. Peak assignments (according to standard diffraction pattern JCPDS 36-1451 of hexagonal phase ZnO) are indicated next to the respective Bragg reflections.*

The films deposited with the lowest molar concentration, namely, 0.03 M, show an amorphous structure. A gradual increase in the sol concentration resulted in the appearance of diffraction peaks which, as mentioned earlier, can be easily matched with the standard database for zinc oxide with wurtzite hexagonal structure. Although weak, these peaks were associated to the (100), (002), (101), (110) planes. However, films deposited from 0.1 M sol concentration demonstrated the highest picks intensity.

An estimation of the crystallite size (table III.1) was made using the well-known Scherrer's formula (eq II.4, Chap.II). It is noticed that the crystallite size increases monotonically with increasing sol concentration, meaning that growth of ZnO thin film proceeds. Apparently, the crystallinity is improved with sol concentration which is manifested by the increase in peak intensities and decrease in the full width at half maximum (FWHM) [6]. i.e. the more the sol is concentrated, the greater is the crystallinity with random orientation. Similarly, Kyaw *et al.* [7] observed an increase in grain size with sol concentration, they suggested that amount of solutes in the sol increases by increasing sol concentration thereby increasing the probability of solutes clustering together forming larger grains.

Moreover, Xu *et al.* [8] indicated that the increase of solute per unit volume solution induces larger electrostatic interactions between the solute particles thus increasing the probability of more colloidal particles to be assembled together forming bigger particles. The bigger colloidal particles eventually lead to bigger ZnO grains. In a study concerning the effect of Zn^{2+} concentration on photocatalytic and antibacterial activity of ZnO coatings, Thongsuriwong *et al.* [9] also observed a similar result and have given more enlightenment to the underlying mechanism. In fact, through hydrolysis process, the metal complex can be transformed to hydrolyzed species. The amounts of them are controlled by the rate of hydrolysis which depends on many parameters including the precursor concentration or even the amount of solute ($Zn(CH_3COO)_2.2H_2O$). After these species coordinate together a process called oligomerization, the polymeric species can form a sol. Moreover, the degree of oligomerization or polymerization is also dependent on the concentration of precursor. Thus, a high concentration of precursor could generate large sized sol particles.

It is worthwhile to notify that for the same sol concentration, with longer aging time, diffraction peaks became narrower with higher intensities. In order to gain an in-depth insight into sol aging time effect, we will consider the sol D (0.1 M) since it exhibited good crystallinity. An enlarged view of XRD pattern of sol D under different aging time is given in Fig.III.3.

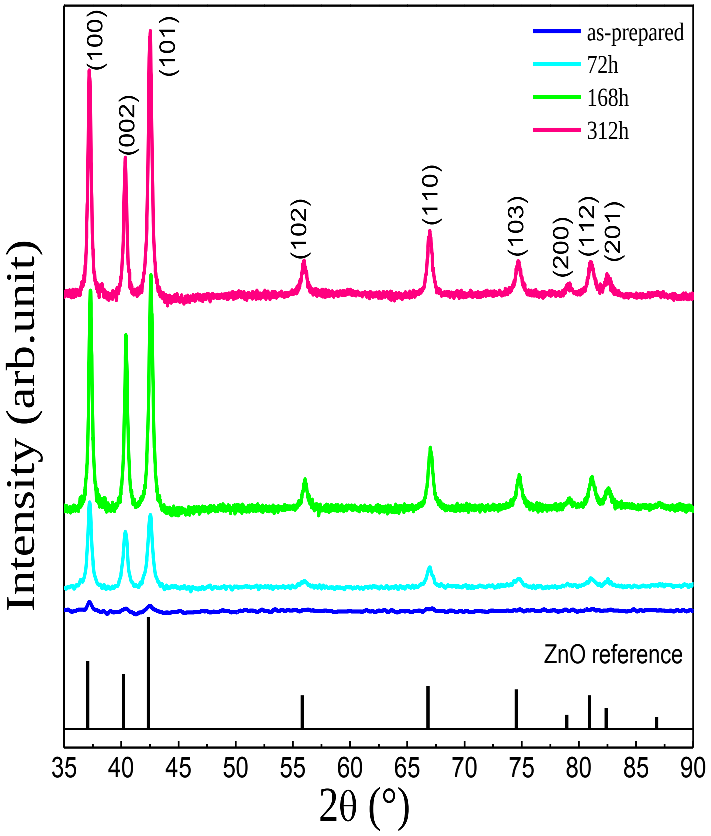

Figure III.3. *X-ray diffraction patterns of ZnO thin films prepared from sol D after different aging time.*

One can notice that thin films prepared from sol without aging show bad crystallinity which is consistent with previous report [10]. This is attributed to the stability of the sol, i.e. the as-synthesized sol is not stable enough in which the colloidal-particle sizes and distribution are non-uniform leading to a poor quality thin films.

It is clearly seen that crystallinity of the as-synthesized samples is enhanced by increasing the sol aging time, meaning that longer aging time promote more grain growth and hence narrower peaks with higher intensities. Different degrees of crystallinity could be reached regarding the aging time, i.e. the longer the sol aging time, the greater is the crystallinity with random orientation. This is demonstrated by the significant increase in crystallite size and decrease in the FWHM with the increment of sol aging time displayed in the plot of figure III.4.

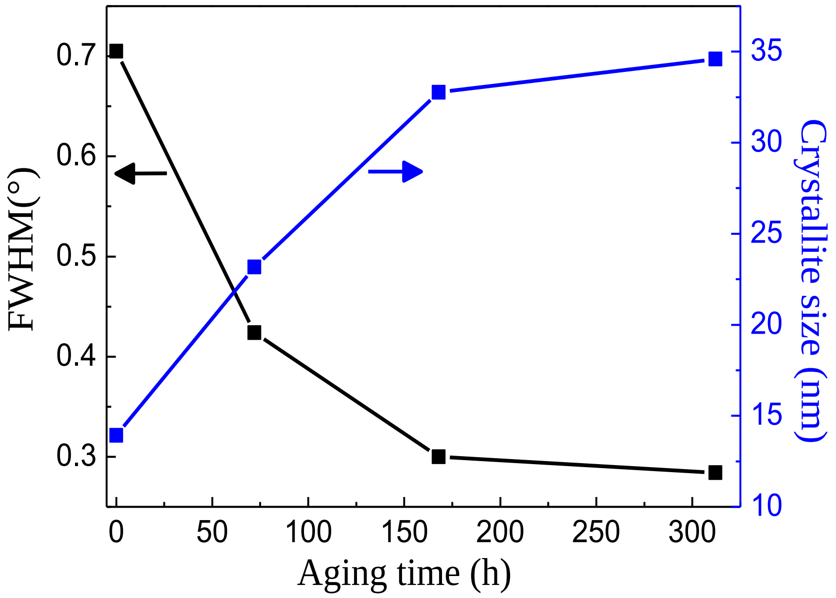

Figure III.4. *Variations of crystallite size and FWHM of ZnO thin films prepared from sol D as a function of sol aging time.*

Fatollahi and Amini [11] found a threefold increase in the intensity of (002) reflection of zinc oxide films using a 3-week-aged zinc acetate solution in comparison to the freshly prepared solution when all the other variables were kept fixed. Also, Singh *et al*. [12] synthesized ZnO nanoparticles via sol-gel route, they found that the crystallite size as well as the crystallinity of the nanoparticles increased with aging time. Ibrahim *et al.* [13] observed that by increasing the precursor aging time, an enhancement of the intensity for all diffraction peaks occurs in general. Despite the difference in precursor composition as well as the deposition route, both we and these previous reports found that sol aging time is of paramount importance in the improvement of the crystallinity. But our results are much better which is manifestly demonstrated from the peaks number and sharpness.

According to Brinker *et al.* [14], chemical reactions that cause gelation continue long after the gel point, producing strengthening, stiffening, and shrinkage of the network. In fact during aging, four processes can occur, singly or simultaneously, including polycondensation, synerisis, coarsening, and phase transformation. Polycondensation increases the thickness of interparticle necks and decreases the porosity by creating additional bridging bonds, thereby increasing the strength and stiffness of the gel network and other properties. An aged gel must develop sufficient strength to resist cracking during drying. The greater stiffness of the aged gel reduces the shrinkage during drying [15]. Scherer [16] studied the structure and properties of gels and pointed out that the network becomes more rigid by aging so that it shrinks less during drying. For that reason, it is advisable to age gels before drying to reduce the chance of racking. Also, Wright *et al***.** [17] recognized aging for improvement of material properties, and explained that shrinkage occurs because new bonds are formed where there were formerly only weak interactions between surface hydroxy and alkoxy groups. This shrinkage leads to expulsion of liquid from the pores of the gel, so that gel samples in sealed containers gradually change in appearance from homogeneous gels to transparent shrunken solid monoliths immersed in liquid. This process is known as synerisis. As for coarsening or ripening, in this process, material dissolves from the surface of large particles and deposits on the initially narrow “necks” which join particles to each other and hence the grain size increases.

As a whole, film crystallinity is enhanced by increasing the sol aging time as well as concentration, meaning that more concentrate sol with longer aging time promote more grain growth and hence narrower peaks with higher intensities.

III.1.2.3.3 Morphological analysis

It is well known that microstructure plays a crucial role in many applications, as the properties of the materials depend closely on their crystal size, morphology and orientation [18]. FE-SEM images of the as-synthesized ZnO thin films by sol–gel dip coating technique deposited from different sol concentrations are illustrated by Fig.III.5 (a–d). The variation of precursor concentration has profoundly affected the morphology. The films show uniformly distributed homogeneous granular structure without cracks overall the surface. The particles are predominantly spherical in shape and are tightly attached to each other. Lower particle size was obtained for 0.03 M inferring that lower precursor concentration produced smaller grains while a relatively uniform compact and bigger grain size is produced with high molar concentrations. This is in good agreement with previous work reported by L. Xu *et al*. [8] were it was assumed that a high molar concentration value introduces more zinc species into the films, leading the stoichiometry of the film to change [19]. Best compact layers were obtained with the most concentrated solutions. This suggests that sol concentration is playing a key role in controlling the nucleation and crystal growth of nanocrystalline zinc oxide.

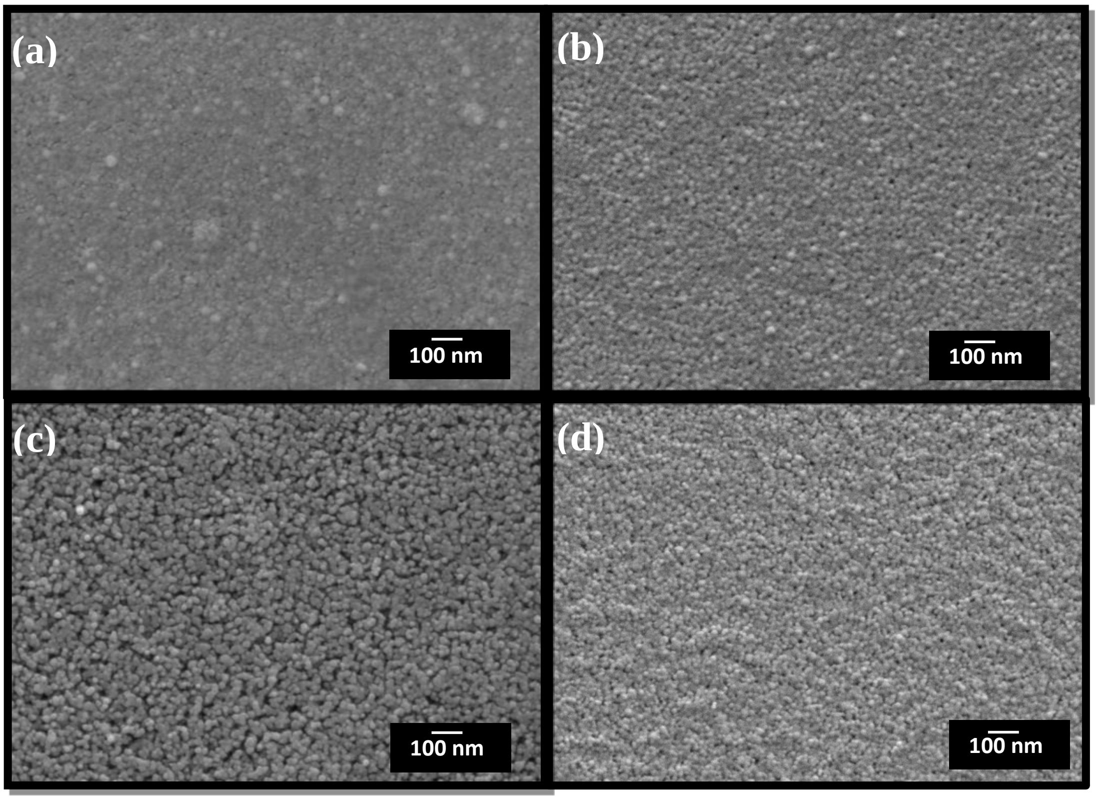

Figure III.5. *FE-SEM images of ZnO thin films derived from different precursor concentrations; (a)0.03M, (b)0.07M, (c)0.09M, (d)0.1M.*

The morphological study of the ZnO thin films obtained from 0.1M sol concentration after different aging time is also carried out. It's clear from later images (fig.III.6) that surface morphology is considerably affected by sol aging time. The as-prepared film produces the appearance of a granular structures composed of small grains that appear somehow aggregated with porosity around. After, by increasing the sol aging time, films exhibit a finer texture in which bigger particles formed by nanocrystals agglomerate that are more effectively packed, giving denser structures characterized by lower porosity. The differences in the film morphologies can be correlated with the particles shape. For sols reached an aging time as long as 168 and 312 h, the ZnO thin film is composed of vertically aligned densely packed randomly oriented nanorods with diameter in the range 43–87 nm having various lengths. The results from FE-SEM images are consistent with the observations from XRD. ZnO nanostructures have different orientations with particle size increasing as a function of aging period. The aspect ratios (length divided by width) of the nanorods ranges from 1 and 2 nm. Especially, the length of the grain depends on the sol aging time. An average value of about 155 nm was observed for the samples deposed after sol being aged 312 h, i.e. longer aging time results in higher nanorod length.

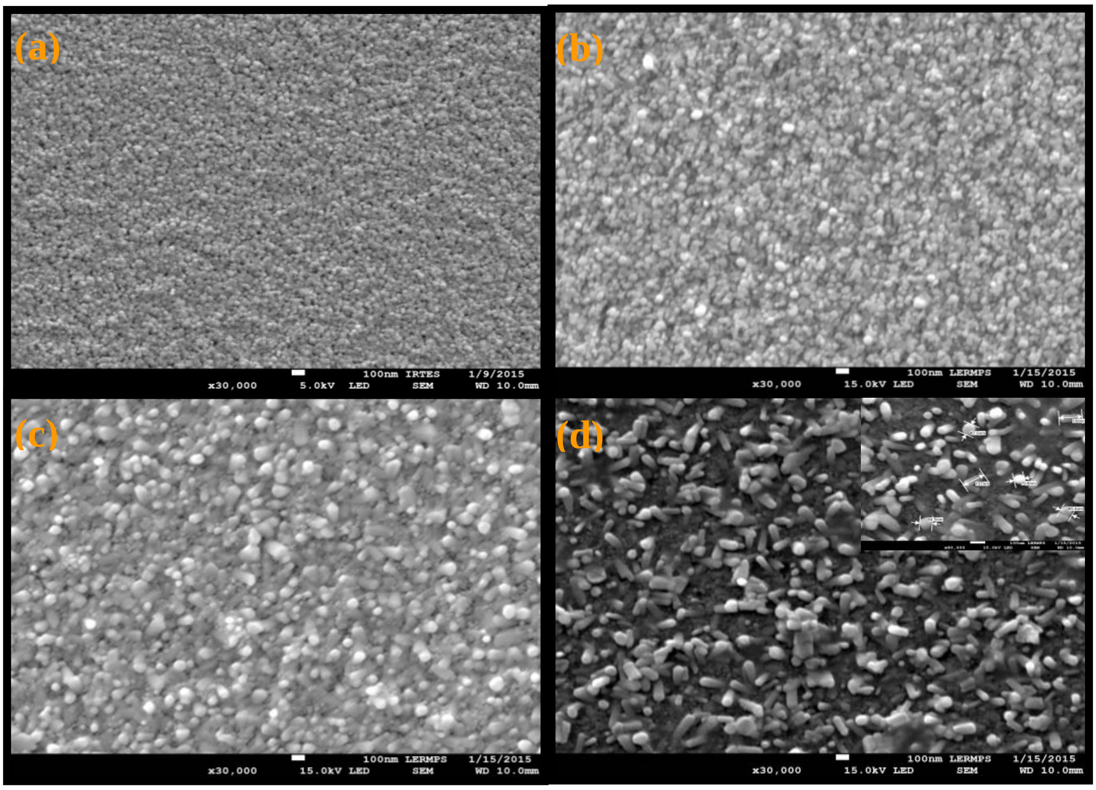

Figure III.6. *FE-SEM images of the ZnO thin films for different aging time: a) as-prepared, b) 72 h, c) 168 h, d) 312 h. The inset shows the magnified surface morphology*

In addition, the film surface morphology and surface roughness were also studied using an AFM technique. Fig.III.7 displays AFM images in tapping mode of ZnO thin films deposited from different sol aging time. It reveals that all films have a smooth surface morphology, and the cracks and pinholes were absent. The root-mean square (RMS) of average surface roughness for all samples was determined for scanning area of 5µm × 5µm. The measured roughness values were 10.67, 5.07, 5.72 and 7.33 nm corresponding to ZnO films aged for 0, 72, 168, and 312 h, respectively. From this data, it could be also found that the surface roughness of the films decreased as sol aging time increased then slightly increased for sol aged 312 h. The increase of surface roughness along with sol aging time may be attributed to the larger grain formation and more porosity of the films. Generally, by increasing the sol aging time, more uniform, compact and smoother films were obtained. This is in good agreement with the FE-SEM results. Accordingly, the quality of ZnO thin films prepared by aged sols is improved.

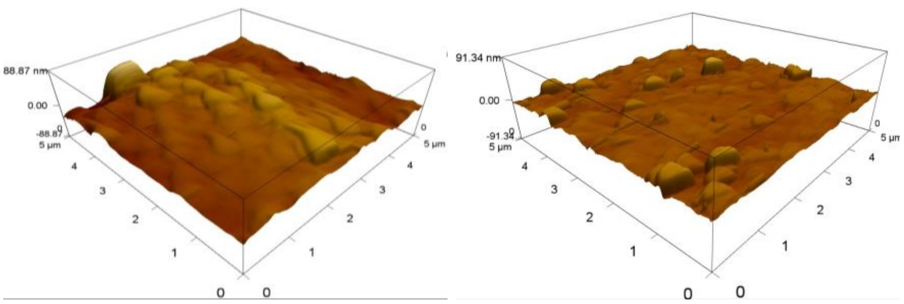
(a) RMS=10.67nm (b) RMS=5.07nm

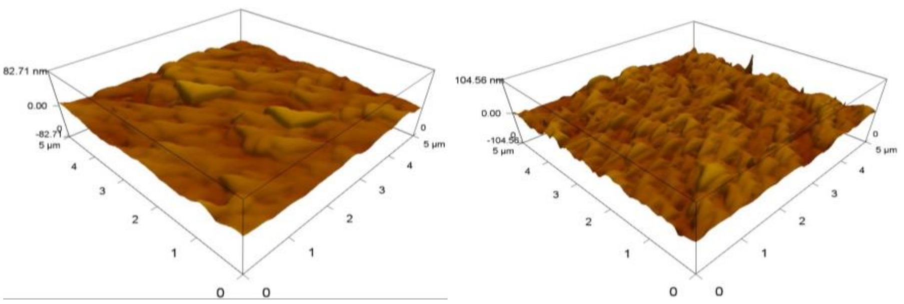
(c) RMS=5.72nm (d) RMS=7.33nm

Figure III.7. *AFM surface morphology images of the ZnO thin films after different aging time: a) as-prepared, b) 72 h, c) 168 h, d) 312 h.*

III.1.2.3.4 Optical properties

Optical properties of ZnO particles become increasingly important as the size of particles is reduced to nanoscale [20]. Study of the optical properties of the samples was based on the results obtained from UV–Vis spectroscopy. Figure III.8 shows spectral dependencies of films transmission on sol concentration in the uv-visible spectral range. It is inferred that films were transparent with an average optical transmittance exceeding 70% in the visible spectral region and present a sharp absorption edge in the UV region at wavelength ranging from 369 to 379 nm suggesting superior optical quality. What is more, transmission increases sharply in the visible region due to onset of fundamental absorption of ZnO. The sharp absorption edge directly indicates that the ZnO thin film is a direct band gap semiconductor. It also indicates that grains are more uniform and the defect density is lower in the prepared samples [8]. It is worth noticing that there was a shift in absorption edge with sol concentration which is attributed to grain growth as ascertained by XRD results.

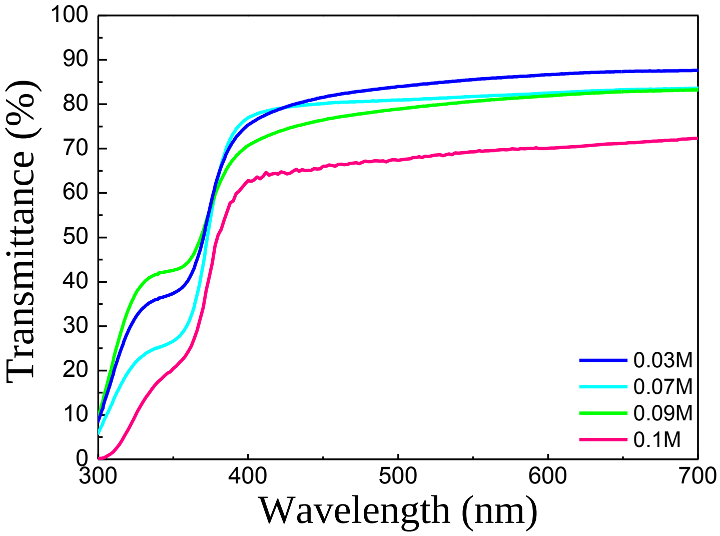

Figure III.8. *Optical transmission spectra of ZnO films deposited from different sol concentrations.*

However, when the sol concentration is more than 0.09 mol/L, the transmittance of the films decreased. Similar results were also reported by O'Brien *et al*. [21]. It was observed that increasing the zinc concentration of prepared sol–gels resulted in an increase in film thickness from 74 nm (0.03M) to 204 nm (0.1M). The transmittance of ZnO thin films is mainly affected by three factors including films thickness, surface roughness and the density of grain boundary [8]. As for the films prepared in this study, the main factor that decreases the transmittance of the ZnO thin films deposited by high concentration sol is presumably the film thickness which may be also an important factor affecting the transmittance in the visible range. Some researchers [22] observed another trend; they found that the transmittance of ZnO thin films in the visible range was gradually enhanced when the sol concentration was increased. They attributed the increased transmittance to the improvement of crystalline quality of ZnO thin films.

The direct and indirect allowed optical transitions can be evaluated by fitting a straight line in strong absorption spectral region using the Tauc relationship (eq.II.6).

A plot of $(\alpha h\nu)^2$ versus $h\nu$ is given in Fig.III.9. The energy band gap is evaluated by extrapolating the linear portion of the curves until they intercept the photon energy axis. Effect of sol concentration on energy band gap is shown in the inset of fig.III.9. Band gaps were ranging from (3.20-3.25) eV. There was a decrease in the optical band gap by increasing precursor concentration from 0.03 to 0.1 M. This result was also found for sprayed [23] and electrodeposited ZnO films [24]. Thus, regardless the deposition method, the sol concentration affects the microstructure of the film network which causes the change in the optical properties of the films.

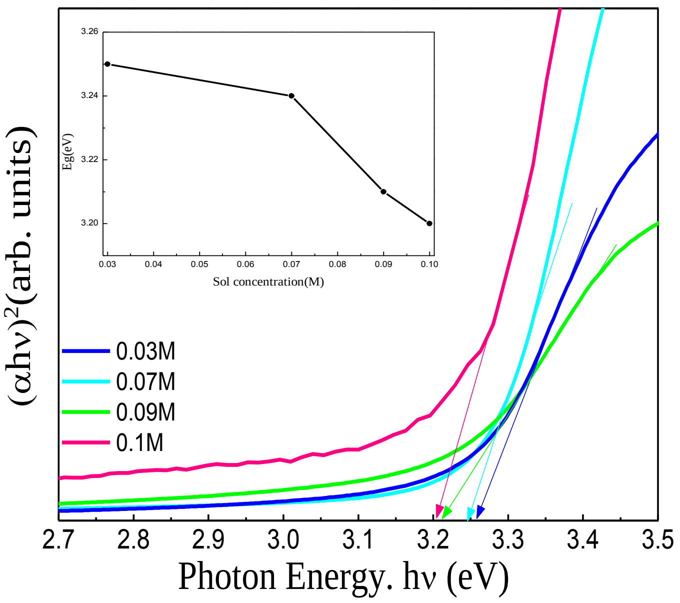

Figure III.9. *Plot of* $(\alpha h\upsilon)^2$ *versus photon energy (hυ) and linear fitting for ZnO film with different sol concentration. The inset shows the corresponding band gap variations with respect to* Zn^{2+} *amount.*

Figure III.10 depicts the optical transmission spectra of ZnO films deposited from precursor sol (D) aged for different durations recorded in the uv-visible region. The deposited films are transparent with the highest value of transmission in the range 78 % in the visible range. There has been an increase in optical transmittance. This increase is due to the decrease in surface roughness of films as confirmed by AFM images. Later the grains grow up in disordered manner resulting in scattering of light and a slight decrease in optical transmittance of the films.

As shown in Fig.III.10, the aging time, from 0 to 168 h, does not considerably affect the strong absorption property of ZnO thin films in the ultraviolet range and the fundamental absorption edges of the samples all locate at ~ 370 nm which corresponds to optical bandgap transition of ZnO. Later, it was found that further increase in aging time resulted in a small variation in absorption edges.

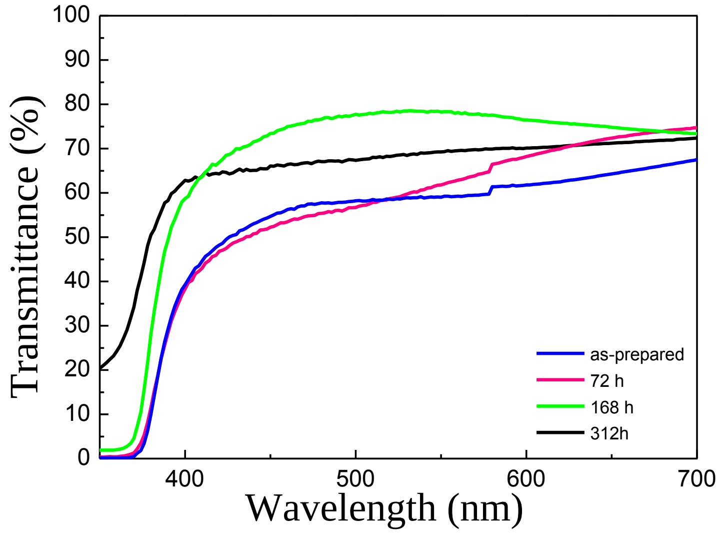

Figure III.10. *Optical transmission spectra of ZnO films for different aging time.*

Fig.III.11 shows the Tauc plots for the ZnO thin films deposited from sol being aged for different time. It's observed that an increase in optical energy gap from 3.19 eV to 3.25 eV occurred when the sol aging time varied between 0 and 312 h, respectively. We presumably attribute the variation of optical Eg with sol aging time to the improvement in the crystalline quality of the films, already proved by XRD results.

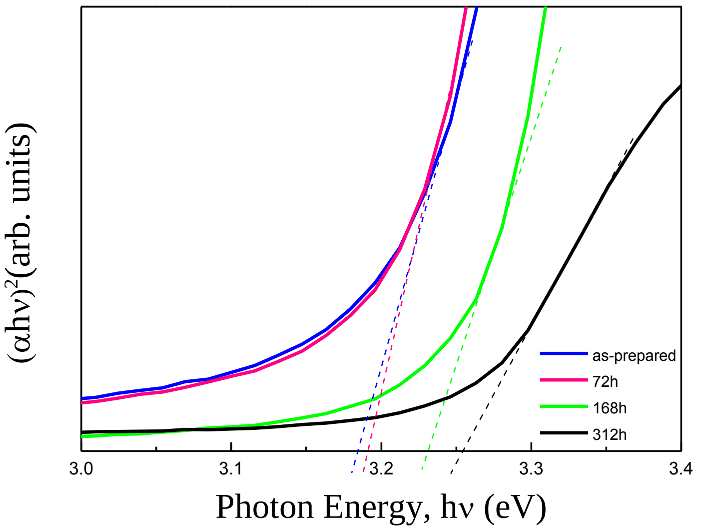

Figure III.11. *Plot of $(\alpha h\upsilon)^2$ vs. photon energy ($h\upsilon$) of ZnO film with different sol aging time.*

III.1.2.4 Conclusion

We reported an experimental study on the synthesis and characterization of nano-structured pure ZnO thin films via sol–gel dip coating method on glass substrates. The main goal of this part was to find the optimal deposition conditions. The crystalline structure, surface morphologies and optical transmittances of the sol–gel derived ZnO thin films depended greatly on Zn^{2+} molarities and sol aging time. XRD measurements have revealed that all thin films are polycrystalline ZnO single-phase with a wurtzite hexagonal structure and displayed a random orientation. The crystallinity enhanced as the sol concentration and aging time increases. Crack-free films were obtained in all cases. FE-SEM micrographs have shown that the grain size tend to increase with increasing sol concentration and revealed that thin films prepared from aged sol were relatively smoother with minimum surface roughness and the heavily aged samples exhibit nanorods morphology. The UV–Vis spectroscopy analyses have shown that all the thin films were transparent in the visible region. Moreover, the optical transparency of films was significantly enhanced by aging the solution for longer time. Interestingly, sol concentration of 0.1 M aged for 72-168 h was found to be optimal to achieve smooth surface morphology, good crystallinity and optical transmittance which were attributed to an ideal stability of solution. These observations provided a useful guideline for the process control purposes and led us to the conclusion that the selection of the sol concentration and aging time are key factors for obtaining good quality ZnO thin film via the solution route. The next part will be devoted to the study of the rare earth doped zinc oxide thin films.

III.1.3 Rare earth doping effect

The present work mainly aims on clarifying the influence of rare earth elements on the microstructure development and optical properties of the ZnO thin film.

III.1.3.1 Materials

For the preparation of ZnO sol, the following materials were used: zinc acetate dehydrate, methanol, Neodymium acetate and Praseodymium nitrate. The glass slides (76×26mm) for substrates of ZnO films were from ISO-LAB (Germany). Distilled water was used to rinse substrates. All chemicals were of analytical grade, obtained from commercial sources.

III.1.3.2 Films preparation and processing

Undoped and RE–doped zinc oxide transparent thin films were synthesized by sol gel and deposited by dip coating. In a typical synthesis process, zinc acetate dihydrate [$Zn(CH_3COO)_2.2H_2O$] was added to methanol and stirred at 70°C for an hour to yield a clear and homogeneous solution which served as coating sol after aging at room temperature. Doping was achieved by adding Neodymium acetate or Praseodymium nitrate to the solution in variable amounts (0-7at.%).

Prior to the deposition, the glass substrates were ultrasonically cleaned in acetone, alcohol and distilled water for 15 min respectively, and subsequently dried in air stream. Thin films were deposited on glass substrate by dip coating technique at room temperature and withdrawn at a speed of 5 cm/min. The films were dried at 170°C for 15 min after each successive coating. The coating procedure was repeated several times to obtain desired film thickness. Finally, all the samples were annealed in a furnace at 500 °C for 1 hour under ambient atmosphere in order to obtain the ZnO films.

The morphological, structural, and optical properties of the investigated thin films were analyzed to determine the influence of the dopant content. The morphology and cross sectional images of the samples was inspected using a scanning electron microscope (Carl Zeiss AURIGA CrossBeam workstation) at an accelerating voltage of 5 kv, equipped with X-MAX 150 Energy dispersive X-ray spectrometer (EDS) detector to analyze the elements concentration profiles of the films. The crystalline structures of the films were analyzed by X-ray diffractometer (XRD) employing a PANalytical X’pert PRO diffractometer with a Cu Kα source (λ = 1.54060 Å). The optical properties were measured by a UV–vis–NIR double beam spectrophotometer (UV-1800 PC, Shimadzu). The room temperature PL spectra was measured using a PerkinElmer LS 55 Luminescence spectrometer equipped with a high energy pulsed Xenon source for excitation.

III.1.3.3 Results and discussions

III.1.3.3.1Morphological analysis

The surface morphology and composition of the thin films were determined by scanning electron microscopy equipped with EDX analysis. The SEM image of undoped ZnO film is shown in Figure III.12. The image of pure ZnO revealed that films are composed of nanosized grains with low residual porosity. The cross-sectional image confirmed that film were less uniform exhibiting granular nature and allowed us to estimate the film thickness (209nm). Moreover, the EDX indicated that films are purely composed of zinc and oxygen, although there are some other elements, such as Si, Na, C, and Ca, which are attributed to the substrate constituents.

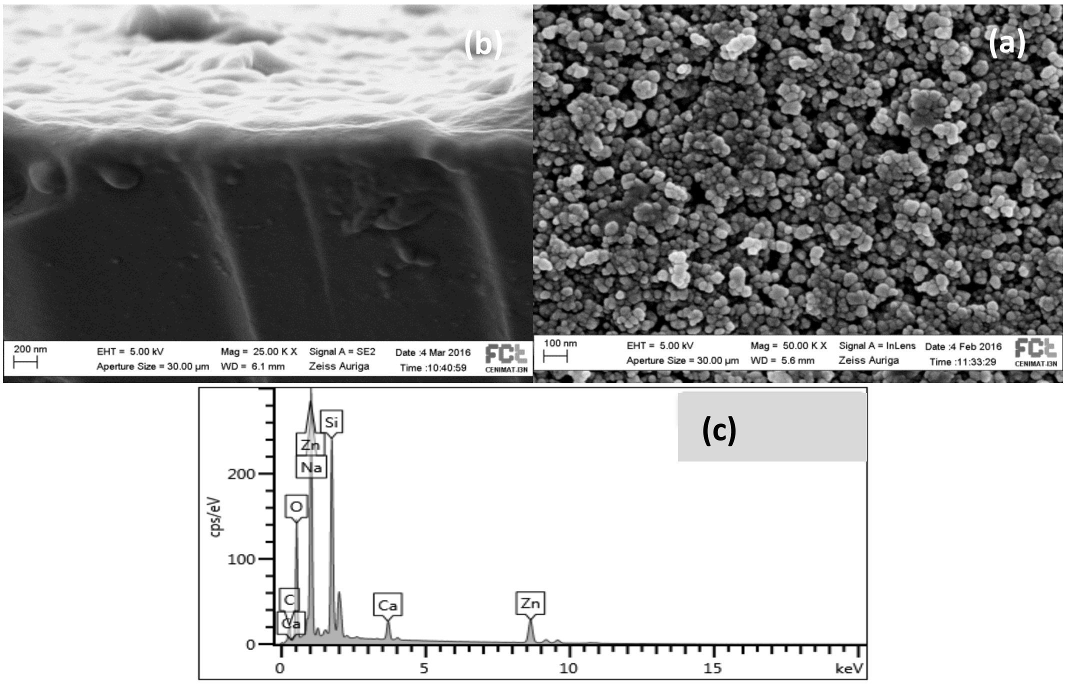

Figure III.12.*Pure ZnO surface morphology (a) with the corresponding cross sectional image (b) and elemental composition (c).*

Fig.III.13 show Nd and Pr doped ZnO thin film prepared under different doping content. It is obvious that the effect of Nd and Pr doping on morphology is noteworthy. All films have appeared to be formed by rounded shape ZnO nanoparticles uniformly distributed on the film surface. These images reveal that films with low dopant concentrations exhibit slight porosity and are covered with irregularly shaped grains showing well-defined boundaries.

It is interesting to note that 1 at.% Pr or Nd doped ZnO films are relatively smooth, homogeneous and uniform with denser morphology without visible voids and defects overall the surface. While films obtained with doping higher than 3% for both Pr and Nd were inhomogeneous with high density of clusters randomly distributed on the film surface. The grains become hardly distinguishable as the RE ion concentrations increased with many obvious voids found. Apparently, there is a lower probability of rearrangement of the arriving material as the dopant content increases thus the inhomogeneity increases inducing the formation of small heaps and clusters. The disorder increases by introducing more impurities in the host ZnO which is in agreement with XRD results (next section) where crystallinity tends to degrade with increasing RE content. Also the 7 at.% Nd doped ZnO shows a wrinkle network with spherical nanoparticles whereas the 7 at.% Pr doped samples show agglomerate into large islands.

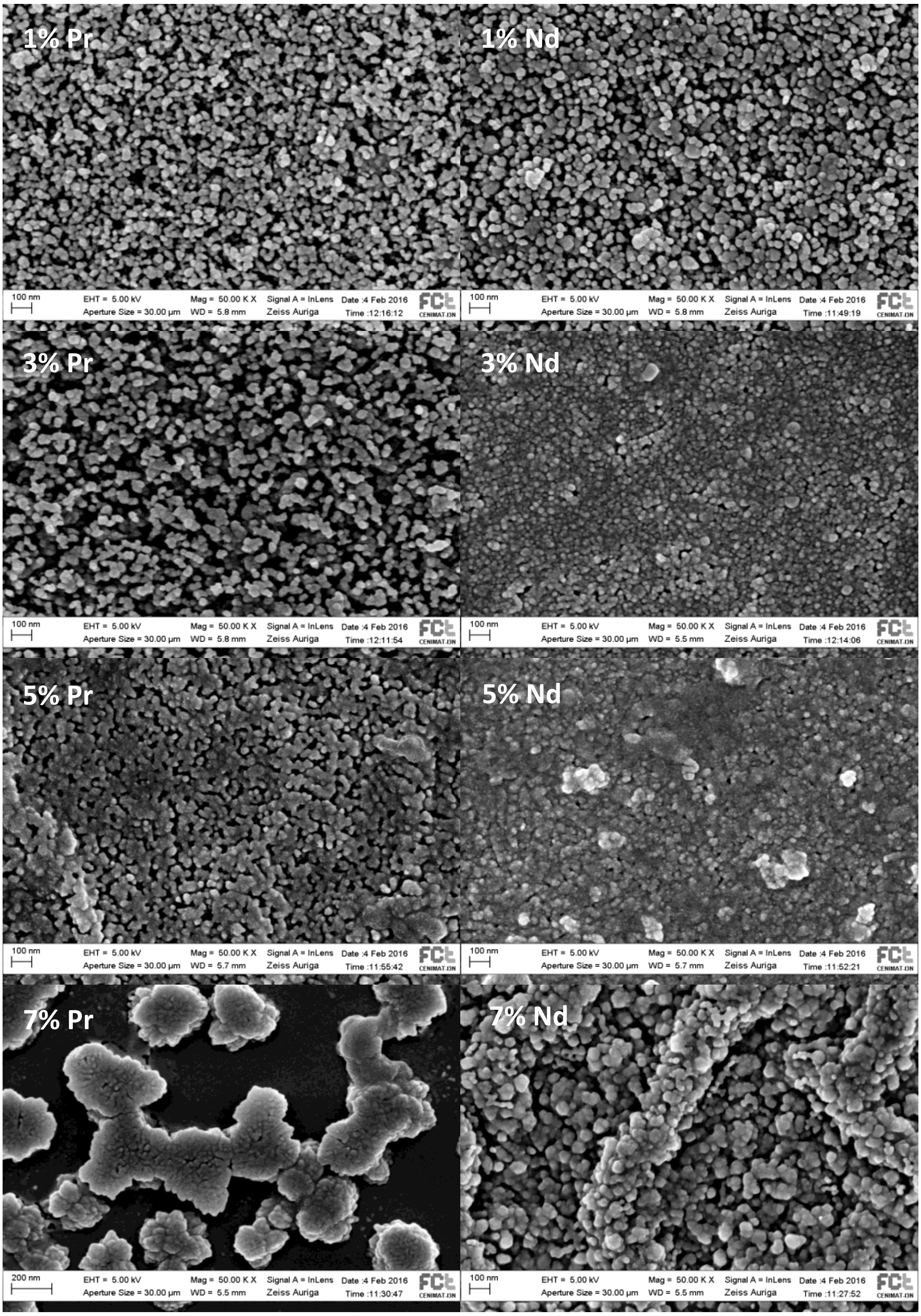

Figure III.13. SEM images of RE-doped ZnO.

The EDX analysis was performed to confirm the presence of Nd or Pr in ZnO thin films. Results were collected from several parts of the doped films. Fig. III.14 shows the EDX spectra of the doped ZnO films. It reveals that the films consist of Zn, O and Nd or Pr which confirms the substitution of dopants in ZnO. The EDX spectra of the doped samples show the presence of some elements that does not appear in the diffractograms which are related to the substrate components and substrate peaks. From this elemental analysis, it was also found that the amount of incorporated Nd^{3+} and Pr^{3+} ions increases concomitantly with increasing their respective RE^{3+} precursor concentration added to ZnO sol.

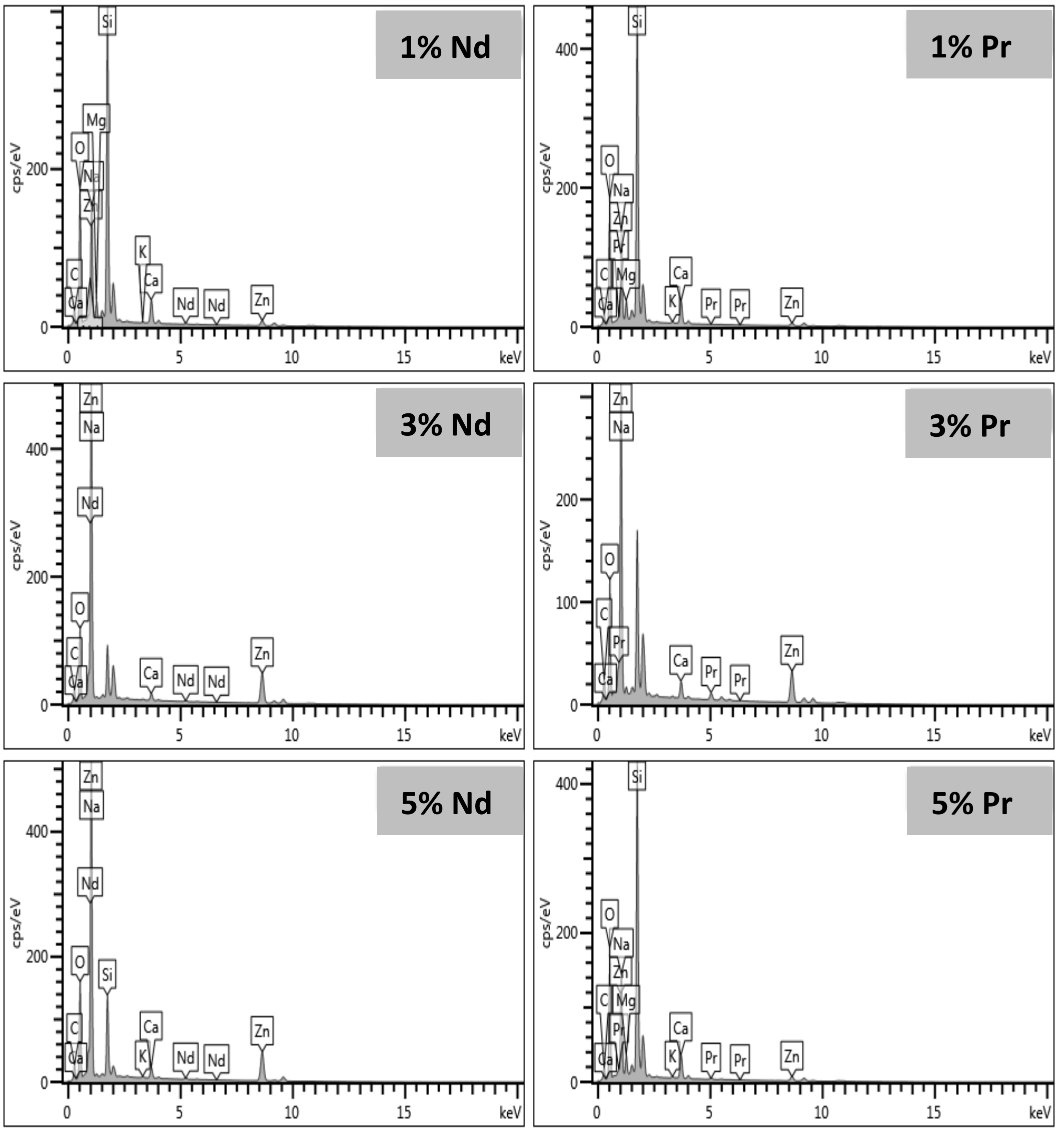

Figure III.14.*EDX spectra of the selected set of RE doped ZnO samples.*

III.1.3.3.2 Structural characterization

Figures III (15-16) depict the XRD patterns of ZnO films modified with two different rare earth ions. The ZnO average crystallites size calculated according to Scherrer's formula (eq.II.4) and lattice parameters along the growth direction (002) are reported in Table III (2-3) for the prepared samples.

The diffraction peaks in all the films are indexed to the hexagonal wurtzite structure of ZnO and the data are in agreement with JCPDS card (JCPDS 01-070-8070). The intensity of the diffraction peaks relative to the background signal demonstrates high purity and good crystallinity of the synthesized samples. Although the peak intensities and positions slightly changed in few degrees after the ion modification, rare earth oxide diffraction peaks are not observed from the diffractograms. It may be attributed to their low loading amount and high dispersity of the guest species in the host oxide matrix [25,26].

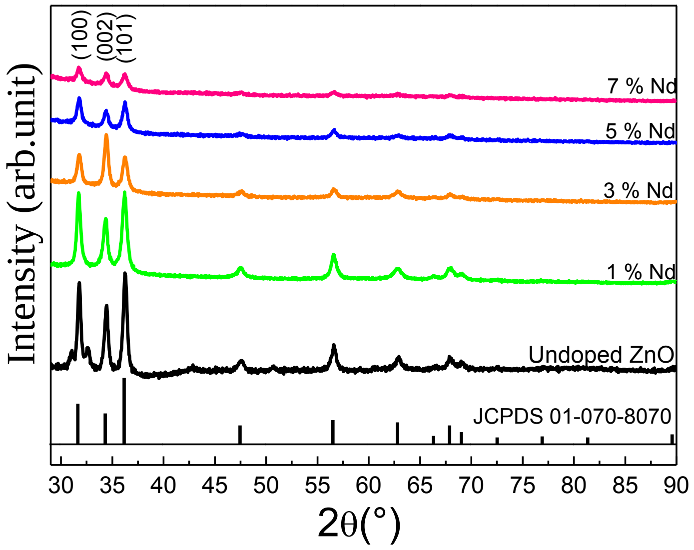

Figure III.15. *XRD pattern of undoped ZnO and ZnO:Nd under different dopant content.*

It is clear from the XRD patterns (III.15) that ZnO and ZnO:Nd films were of polycrystalline nature with three main reflection peaks at 31.7°(100), 34.4°(002) and 36.2°(101). Also, it was noted that the FWHM increases with increasing Nd concentration and this implies decrease in the crystalline quality [27].

The incorporation of 1 at.% Nd doping displayed good crystalline quality thin film, however, by increasing Nd doping concentration above 1at.%, the intensity of the peaks drops gradually. This result is in good agreement with SEM results. It means that increasing the Nd content beyond a certain level (1at.% in this study) can restrain the crystal growth of ZnO. This may be due to the formation of Nd–O–Zn on the surface of the doped samples, which hinders the growth of crystal grains. F. Xian *et al*. [28] also found that 1% Nd doped ZnO thin film has the best crystalline quality.

At the same time, one can observe a slight shift in the (002) peak position toward lower angles for the 1at.% Nd doped films. This further indicates that dopants had been incorporated into ZnO films making the ZnO lattice expands along the c-axis when Nd atoms enter the matrix and substitute into the Zn^{2+} sites. Such an expansion is quite reasonable and can be qualitatively understood considering difference between the size of the ions involved in the doping process; the ionic radius of Nd^{3+} (0.99 Å) is much larger than that of Zn^{2+} (0.74 Å), which creates lattice strain and consequently increases the lattice parameter [29].

Table III.2. Lattice parameters, crystallites size and peak width of ZnO:Nd samples.

Sample	FWHM (002)	2θ (°)	D (nm)	d (Å)	c (Å)	a (Å)
ZnO	0.409	34.42	20.32	2.602	5.204	3.004
1at.%Nd	0.463	34.35	17.95	2.607	5.215	3.010
3at.%Nd	0.446	34.41	18.63	2.603	5.206	3.005
5at.%Nd	0.447	34.40	18.42	2.603	5.207	3.006
7at.%Nd	0.435	34.41	19.11	2.603	5.206	3.005

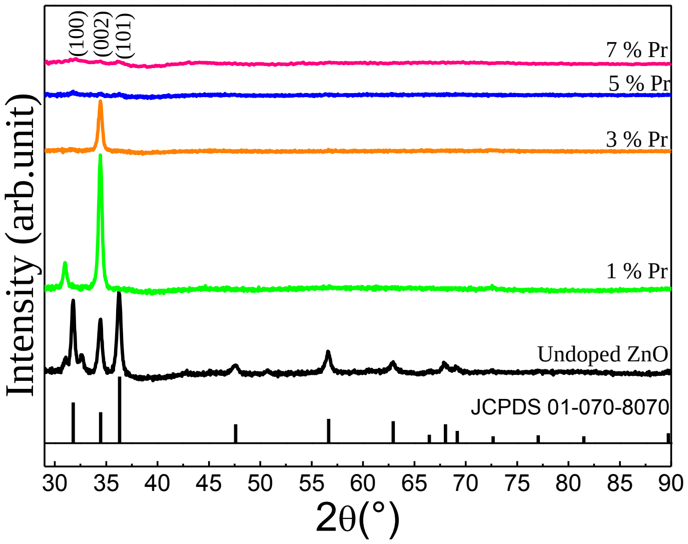

***Figure III.16.** XRD pattern of undoped ZnO and ZnO:Pr under different dopant content.*

As for the XRD pattern (Fig.III.16) of ZnO and ZnO:Pr, it is obvious that crystallinity was considerably enhanced by introducing praseodymium into the ZnO matrix. No diffraction peaks from Pr_2O_3 or other impurities are found in any of the samples within the detection limit. Particularly, samples doped with 1 at.% Pr exhibits high crystalline quality compared to the undoped with decreased average crystallite size. This trend is in agreement with the literature [30,31]. Moreover, the 1at.% Pr films exhibited preferred orientation along the (002) lattice plane, which suggests that the nanoparticles are quasi-aligned along the *c*-axis oriented perpendicularly to the substrate surface. Balestrieri and co-workers [32] also deposited ZnO:Pr thin films by magnetron reactive sputtering and obtained films with a strong texture along the (002) direction. Basically, films grow to minimize the surface free energy. If the surface free energy of a plane is lower than that of other planes, the films grow with the plane of lower surface free energy. In the case of ZnO crystal, the surface energy density of the (002) orientation is the lowest. Grains with lower surface energy will become larger as the film grows. Then the growth orientation develops into one crystallographic direction of the lowest surface energy. This means that (002) texture of the film may easily form. The *c*-axis orientation can also be understood by the “survival of the fastest” model proposed by *Drift*. According to this model, nucleations with various orientations can be formed at the initial stage of the deposition and each nucleus competes to grow but only nuclei having the fastest growth rate can survive, leading to a *c*-axis orientation [33]. The high crystallinity of 1at.% Pr also suggests that the Pr doping is uniform and does not introduce extensive defects [34].

The 1at.% Pr doped ZnO film shows an enhancement in intensity compared to that of the (3-7) at.% Pr doped ZnO films which show a reduction in intensity with the appearance of several medium to weak peaks indicating the polycrystalline nature of the film which is consistent with previous reported study[35].

From the above results, it can be concluded that a proper RE-doping concentration can greatly improve the crystalline quality of ZnO thin films.

Table III.3. Lattice parameters, crystallites size and peak width of ZnO:Pr samples.

Sample	FWHM (002)	2θ (°)	D (nm)	d (Å)	c (Å)	a (Å)
ZnO	0.409	34.42	20.32	2.602	5.204	3.004
1 at.%Pr	0.422	34.43	19.70	2.601	5.203	3.003
3 at.%Pr	0.404	34.43	20.57	2.601	5.203	3.003

III.1.3.3.3 Optical properties

The optical transmission spectra of undoped and RE doped ZnO films recorded in the wavelength range of 300–900 nm are shown in Fig.III. (17-18). The synthesized films show high transmittance with an average value of 92 % and 96 % for Nd-ZnO and Pr-ZnO, respectively in the visible region. The slight reduction in transparency of the (5-7) at.% RE doped films compared to that of the 1 at.% and 3 at.% RE doped films is an indication of the decline in the crystallinity of the films as already evidenced from the XRD and SEM analyses. Almost all the RE doped films showed an improved transmittance as compared to the undoped ZnO films which is consistent with previous report [35].

The absorbance spectra of pure and RE doped ZnO films are shown in the insets of Fig.III.(17-18). It is worth mentioning that absorption peaks for both Nd-doped and Pr-doped samples have shown blue shift relative to the bulk exciton absorption (386 nm). Similar observation has been reported elsewhere [36].

On the other hand, it was noticed that when the RE^{3+} concentration was further increased to (5-7) at.%, the absorption band edge shifted towards higher wavelengths (red-shift).

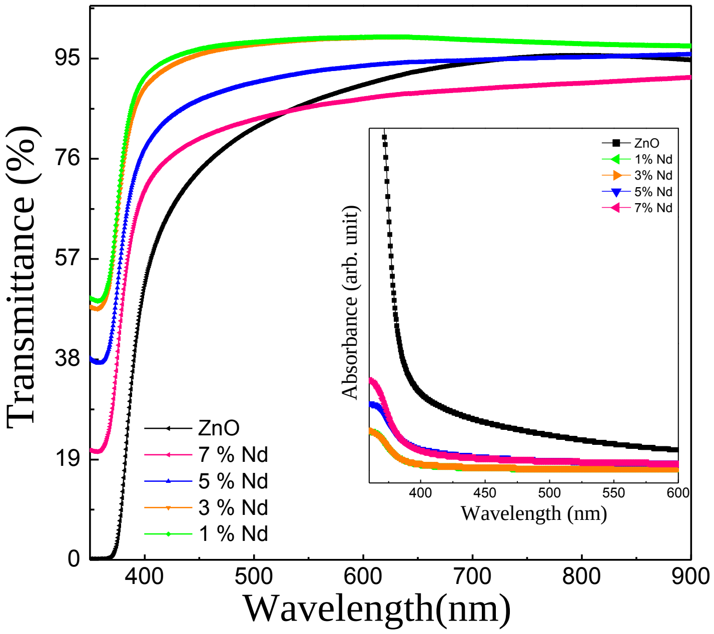

Figure III.17. *Transmittance spectra of the ZnO and Nd-doped ZnO thin films for different Nd concentrations. The inset shows the corresponding absorbance spectra.*

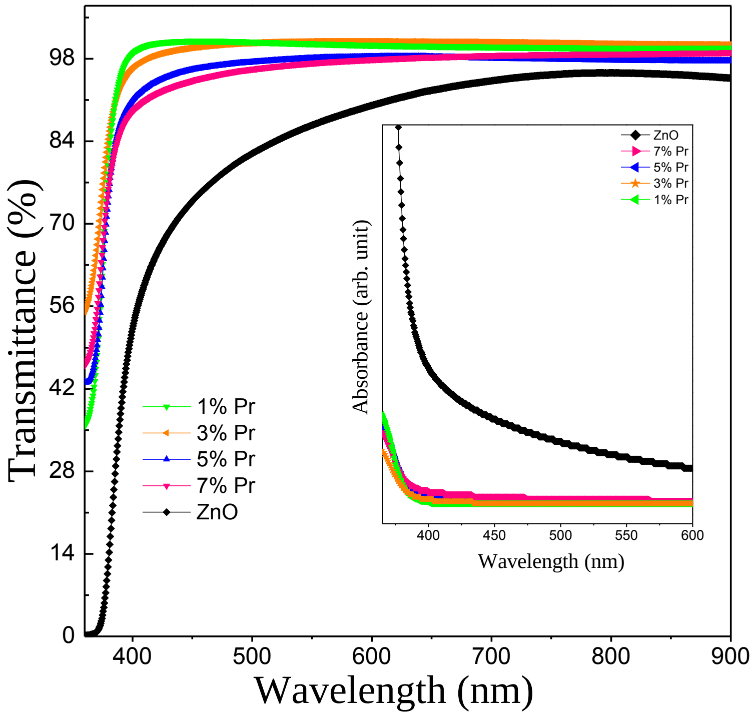

Figure III.18. *Transmittance spectra of the ZnO and Pr-doped ZnO thin films for different Pr concentrations. The inset shows the corresponding absorbance spectra.*

By constructing the Tauc plots, the band gap energies (Eg) of undoped and RE^{3+} doped ZnO samples were then determined (Fig.III.19-20).

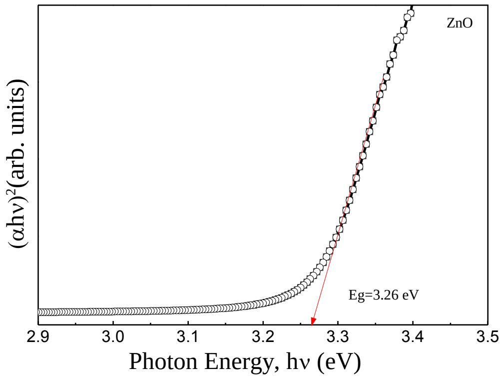

Figure III.19. *Tauc plot of the undoped ZnO.*

The optical band gap energy of ZnO film was about 3.26 eV while it was in the range of (3.27-3.24) eV for Nd doped ZnO films and of (3.28-3.26) eV for Pr doped ZnO. It is observed that the band gap energy of ZnO films increases for 1at.% Pr and (1-3) at.% Nd doping concentration but it shows a reduction in heavily doped film (5-7) at.%. In principal, the band gap energy of the ZnO film is found to be influenced by different factors such as the crystalline quality of the film, grain size, strain, dopant and defects [35]. As seen from the XRD data, there was a small change in the particle size with doping concentration which is not significant to affect the band gap of ZnO films as compared to the change in absorption band after RE substitution. The size effects are known to negligibly influence the band structure of ZnO nanoparticles for diameter greater than 7 nm as suggested by experimental and theoretical studies on ZnO [37].

This shift in energy band gap with doping concentration may be attributed to the incorporation of dopant atoms. This is expected in doped semiconductors and can be understood on the basis of Burstein‑Moss (BM) effect [38]. ZnO is naturally n-type material in which Fermi level will be inside the conduction band when it is heavily doped. The absorption edge in this case should exhibit blue shift because the filled states would block thermal or optical excitations as suggested by Burstein [37]. In this case, the observed variation of band gap energy with RE doping can be attributed to the combined effect of the BM effect and defects in the films.

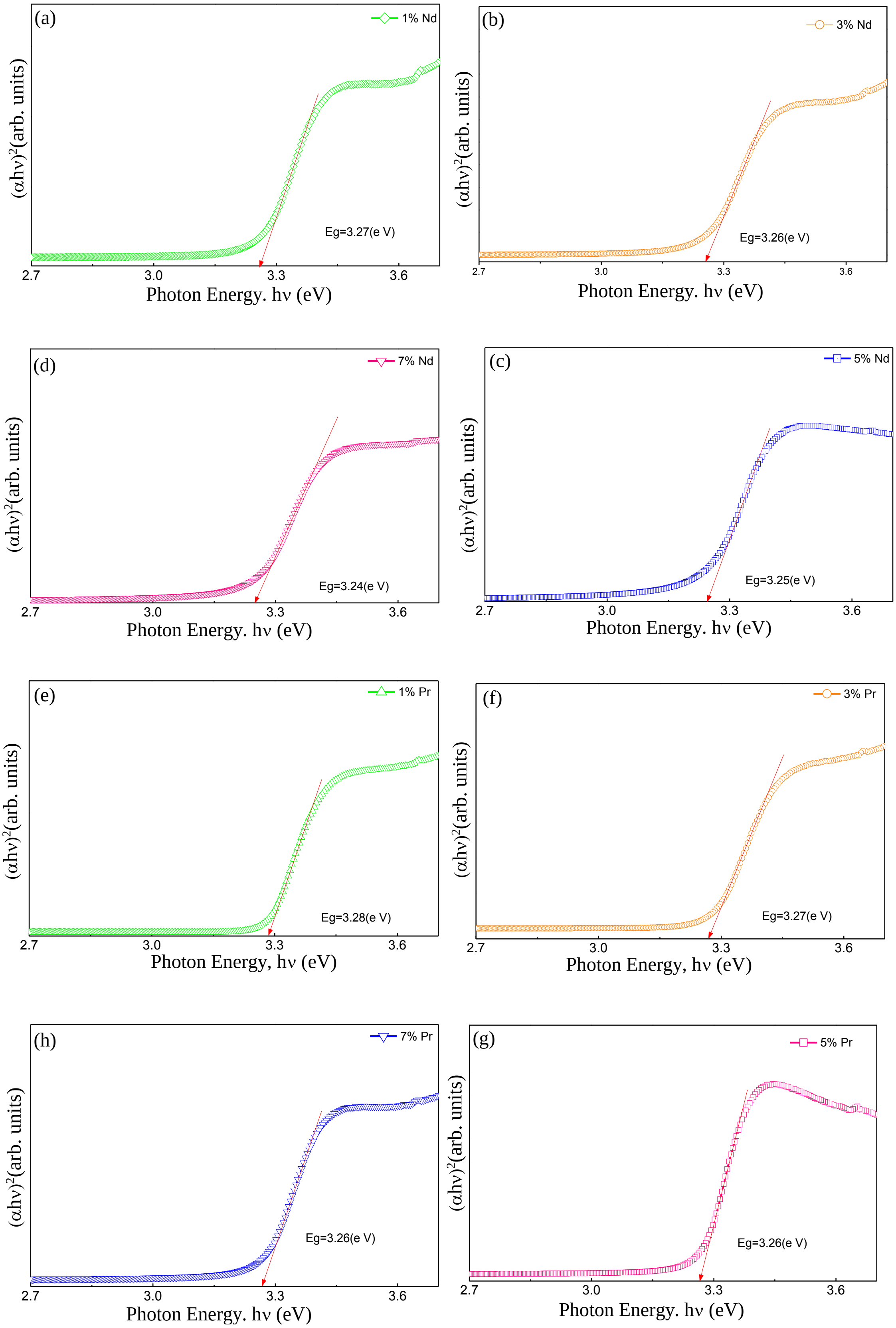

***Figure III.20**. Tauc plots of Nd doped ZnO (a-d) and Pr doped ZnO (e-h).*

III.1.3.3.4 Photoluminescence

In order to study the influence of Nd and Pr doping on the optical properties of the ZnO films, PL measurements have also been carried out. PL spectra were recorded using pulsed Xenon (325 nm) as the light source. Figure III.21 shows the typical spectra for the room temperature photoluminescence of ZnO that were doped with different RE elements.

Photoluminescence measurements of the material show an enhanced emission with increasing impurity doping when compared to pure zinc oxide films, which have feeble emission in similar wavelength region, with the same typical emission spectrum. Typically, the PL spectra of ZnO, in addition to UV emission exhibit also one or more emission bands in the visible spectral region which originate from defect emissions due to recombination of free excitons [39,40]. The investigated samples revealed improvement of visible luminescence intensity, namely with (1-3) at.% RE^{3+} doping concentrations upon excitation of host ZnO into band gap. The doping induced enhancement of visible luminescence intensities of films which may be attributed to more defects generated due to RE^{3+} ions incorporation in the ZnO lattice and energy transfer from ZnO defect states to the guest RE^{3+} ions [41]. A continuous decrease in the emission intensity of the (5-7) at.% RE doped thin films indicates that the decrease in crystalline quality affects the photoluminescence efficiency which is consistent with XRD results. It can be attributed to the weakness of energy transfer from the host to rare earth ions originating from aggregation of rare earth ions on the grain boundaries due to the limitation of solubility and weak interaction between carriers and doping ions [42]. It is well known [43] that structural defects, such as dislocations and grain boundaries, can trap photogenerated carriers into a nonradiative recombination process before the near-band-edge and deep-level radiative recombination occur. This nonradiative relaxation process decreases the PL intensity. Because the (1-3) at.% RE doped ZnO films have a much-improved crystallinity and thus a reduced concentration of nonradiative recombination centers, photoluminescence are noticeably enhanced. Therefore, from these combined results it is very likely that energy transfer from host ZnO defect levels to RE^{3+} is responsible for the enhanced visible luminescence of well crystallized films.

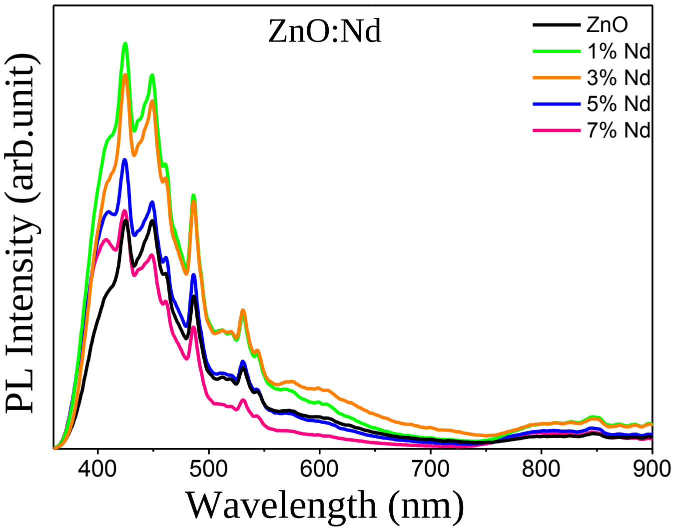

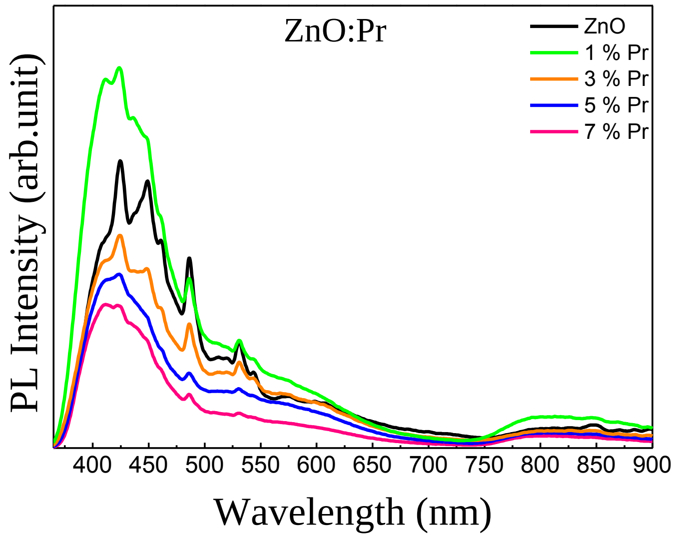

Figure III.21.*Photoluminescence emission spectra of Nd and Pr doped ZnO samples excited at 325nm.*

All of the prepared films showed multiple emissions peaks in the visible spectral region with no emission observed in the UV region. The emission spectra of Nd^{3+} doped ZnO consist of the seven main lines at 407 nm (3.04 eV), 423 nm (2.93 eV), 448 nm (2.76 eV), 460 nm (2.69 eV), 486 nm (2.55 eV), 531 nm (2.33 eV) and 543 nm (2.28 eV). In case of Pr^{3+}doped ZnO films, emission peaks are observed at 409 nm (3.03 eV), 423 nm (2.93 eV), 448 nm (2.76 eV), 460 nm (2.69 eV), 486 nm (2.55 eV), 531 nm (2.33 eV), and 543nm (2.28 eV) which correspond to violet, blue and green emission. Although the origin of the visible luminescence is controversial and has not been conclusively established, there have been a number of hypotheses proposed for each emission band [39]. In fact, these bands are related to specific point defects, either intrinsic or extrinsic [44]. Some researchers speculated that visible emissions come from the electron–hole recombination at a deep level in the band gap caused by intrinsic point defects and surface defects, e.g., oxygen vacancies, zinc interstitials, and the incorporation of hydroxyl groups in the crystal lattice during solution growth [45]. For instance, the emission peak observed at 407 nm may be attributed to the electron transition energy from conduction band to the V_{Zn} [46]. The blue emission peaks arise from interstitial zinc (Zn_i) and oxygen defects. The defect-related green emission (GE) band centered at ~535 nm could be correlated with the green luminescence which has been notably identified as interesting for field emission display (FED). This is classically assigned to the presence of oxygen vacancies and is then very sensitive to the preparation method of the oxide. It has often been ascribed to radiative recombination of photogenerated holes with electrons induced by the oxygen vacancies [47,48,43].

It should be noted that most of the room temperature PL studies of ZnO nanostructures focus on the origin of defect emission or the ratio of UV-to-visible emission. However, position of the near-band-edge emission at room temperature can vary significantly due to variations in relative contributions which will be different for different growth conditions. In addition to the origin of visible emission bands, ratio of UV-to-visible emission is sometimes used as an indication of sample quality. However, it should be noted that as excitation intensity increases, UV-to-visible emission intensity ratio also increases. Thus, high intensity of UV emission at room temperature is not a sufficient proof of good crystalline quality of the sample, i.e. low defect density in the samples, and no valid comparison can be made in terms of sample quality based on PL measurements made under widely different conditions [39]. A material with high defect concentration has a stronger emission for the 550 nm band while usually the exciton band to band is very weak due to quenching by defects. Also by varying the deposition parameters one can produce films with intense UV emission or with intense defect emission [44].

Therefore the RE-doped ZnO films were also excited at relatively elevated excitation wavelength (350 nm) and fig.III.22 show the obtained results. Effectively, excitation at 350 nm resulted in a greatly enhanced PL intensity, but the trend is homologous between the Nd and Pr doped ZnO emissions spectra produced at low excitation wavelength (325 nm) except the appearance of some new emission peaks namely at 359 nm (3.45 eV). The weak emission at 359 nm is a result of the near-band-edge exciton recombination (electron from conduction band with hole from valence band) [49,36,43].

Moreover, it can be seen that with Nd doping concentration increases, the emission intensity gradually increases. The possible reason is that, with the Nd doping concentration increases, the oxygen vacancies in ZnO thin films is greatly increased, thus the opportunity of electron transition from the energy level of oxygen vacancies to the valence band is increased [28]. Concerning doping of the Pr ions into the ZnO lattice, it has been found to result in the increase in emission intensity. This is in line with previous studies [35,47] which ascribed it to the fact that when Pr^{3+} replaces Zn^{2+}, oxygen defects are usually generated to keep the charge neutrality. The increase in the visible emission is therefore correlated well with the successful substitution of Pr atoms into Zn sites in the ZnO lattice as already proved by the EDX.

This result indicates that the band gap structure of the ZnO films can be tailored significantly when Pr^{3+} or Nd^{3+} ions are doped into the ZnO lattice, which may change the luminescent process of the host materials. Based on the aforementioned studies, transfer of energy from the host to rare-earth ions in the case of rare-earth-ion-doped semiconductors often result in strong suppression and/or modification of the host luminescence. In fact, such modification can be taken to be an evidence for energy transfer from the host to the rare earth ions.

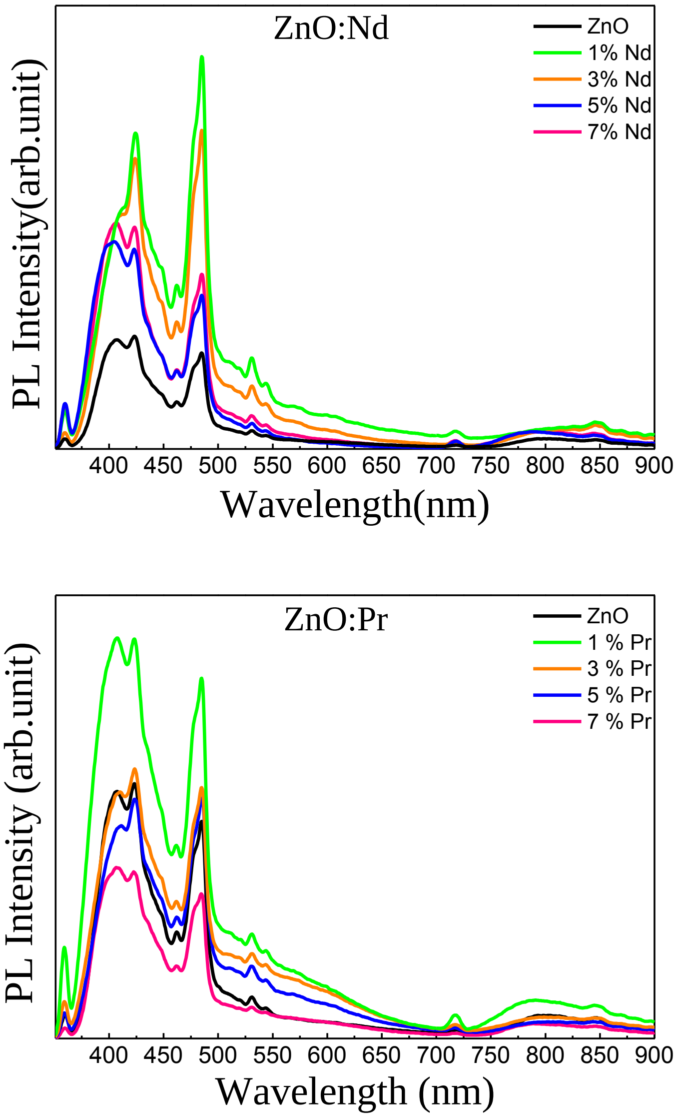

Figure III.22*.Photoluminescence emission spectra of Nd and Pr doped ZnO samples excited at 350 nm.*

III.1.3.4 Conclusion

In summary, a simple sol gel method was employed for preparing RE doped ZnO films and the prepared ZnO samples have been characterized using microstructural and optical measurements. All films have the expected wurtzite structure with a strong texture along the (002) direction in case of Pr doped ZnO samples. Neither secondary phase nor RE oxide peaks have been observed in the detection limit of the X-ray diffraction (XRD) technique. There was an enhancement in the transmittance and photoluminescence emission with the increment of RE dopants in the ZnO matrix.

To achieve effective light emission in doped ZnO, it is of paramount importance that the appropriate energy transfer process is established and a high percentage of the engineered defects can effectively participate in this process.

Overall, the present study suggests that via defect engineering, rare-earth-doped ZnO thin films are promising and have the potential to give efficient multicolor emissions that may find applications in optoelectronic and display devices.

III.2 ZnO thin film prepared by ultrasonic spray pyrolysis

Zinc oxide (ZnO) based TCOs are emerging as a replacement to ITO for opto-electronic applications [50,51]. In this regard, aluminium-doped ZnO (AZO) thin films are considered more promising materials due to their superior electrical and optical properties thus attractive for the illuminated transparent contact of photovoltaic devices [52-55]. Besides, the film deposition via low temperature methods, as investigated in this work, is crucial to allow patterning on flexible substrates, due to the instability of common flexible materials (e.g. polyimide, plastics, paper) at high temperatures [56]. In this section, ZnO and AZO films are prepared by spray pyrolysis, in air, at 300°C and an investigation of the main roles of the dopant concentration and the annealing atmosphere on the properties of undoped and Al-doped ZnO is presented.

The work in this section is based on a paper under consideration for publication [57].

III.2.1 Films preparation and processing

For the synthesis, all chemicals were of analytical grade purchased from Sigma-Aldrich and used as received without any further purification. The (0.29 M) coating solution was prepared by dissolving zinc acetate dihydrate [Zn $(CH_3COO)_2.2H_2O$] in methanol and few drops of acetic acid were added. Aluminium doping was achieved by varying the atomic ratio of aluminium to zinc in the range of 0–1 atomic ratio percents (at,%). Hereafter, the ZnO films will be referred to as: ZnO, AZO25, AZO50, AZO75 and AZO1 corresponding respectively to undoped ZnO, 0.25at.%Al, 0.50at.%Al, 0.75at.%Al and 1at.%Al. The solution was stirred at room temperature for 30 min to yield a lucent and homogeneous mixture which served as the coating solution. The solutions were stable and homogeneous; no particulates or precipitates were visible to the eye and their appearance remained unchanged for several weeks. ZnO and Al-doped ZnO films were deposited on glass substrates (25×75×1 mm Fisherfinest brand, Premium Microscope Slides, USA) via the ultrasonic spray pyrolysis technique. Using ultrasonic cleaning, the substrates were successively rinsed in acetone, isopropyl alcohol, and Mili-Q water and dried by pressurized air. Then, they were transferred to the spray pyrolysis chamber. The deposition was carried out using a Sono-Teks Exacta Coat system with an ultrasonic spray nozzle. The carrier gas used in all the experiments was air, which was supplied by an air compressor. The air produced by the compressor was first filtered and then connected to the glass spray-gun (atomizer), which was positioned at a distance of 18 cm above the substrate heated at a temperature of 300 °C. The whole assembly was kept in an enclosure connected to an exhaust. Using a solution flow rate of 3 mL/min, air carrier gas pressure of 5.4 bar, the droplets were deposited on the substrate through a funnel moving on x–y directions with a scan velocity of 70 mm/s to achieve a good homogeneity.

Following the film deposition, a rapid thermal annealing post-process was performed using an RTA furnace (Annealsys, AS-One100), for 25 min at 350°C under two different atmospheres: forming gas (5% H_2 and 95% N_2) or vacuum. Both heating and cooling rates were 10°C/s. Forming gas annealing was performed under atmospheric pressure while the chamber pressure was less than 7×10^{-5}Pa during vacuum anneal.

III.2.2 Characterizations

The surface morphology and cross-sectional images of the thin films were examined using a Scanning electron microscope (Carl Zeiss AURIGA CrossBeam workstation) at an accelerating voltage ranging from 2 to 5 kv, equipped with X-MAX 150 Energy dispersive X-ray spectrometer (EDS) detector to analyze the elements concentration profiles of the films. The crystallographic analysis of the samples was assessed by X-ray diffraction (XRD) employing a PANalytical X'Pert PRO MPD X-ray diffractometer fitted with an X'Celerator detector. Diffraction data were acquired by exposing samples to Cu-K_α X-ray radiation, which has a characteristic wavelength (λ) of 1.54060 Å. X-rays were generated from a Cu anode supplied with a voltage of 45 kV and current of 40 mA. The data were collected over a 2θ range of 10–89° with a step size of 0.03°. The optical transmission spectra were determined by ultraviolet–visible–near infrared spectrophotometry using a double-beam Perkin-Elmer Fourier transform Lambda 950 equipment. Spectra were taken over a wavelength range of 290 to 2000 nm in transmission mode. The electric study was carried out by Hall Effect measurements using Vander Pauw geometry through a BioRad HL5500PC system.

III.2.3Results and discussions

III.2.3.1 Morphological analysis

The surface morphologies of the as-grown and post-annealed undoped and Al-doped ZnO thin films were examined by SEM. Fig.III.23 depicts surface images of three representative films; ZnO, AZO50 and AZO1 and the corresponding cross-sectional micrographs. Evidently, the film morphology is strongly influenced by the Al content and the subsequent heat treatment. The surface morphologies also reveal a noticeable transformation for the AZO films grown on glass substrates with varying dopant concentration and RTA atmosphere. ZnO and AZO50 films exhibited similar grain shape and appeared smoother when annealed in forming gas. The films are composed of closely packed granular plate-like features as can be seen from the figure and the microstructure is found to be continuous and dense. As stated earlier, all of the sprayed films have been grown in methanol with zinc acetate as zinc precursor which, according to Arca *et al*. [58], produces smooth and good quality layer in contrast to other zinc precursors such as zinc chloride that led to rough discontinued layers, either in combination with organic solvents, water or a mixture of them. This is related to different coproducts that are formed during the pyrolytic decomposition of the different precursors so less grain boundaries and hence a higher conductance are expected.

A particular structure was observed in the SEM images for films annealed in vacuum; films were composed of rounded grains. These SEM images show that the surface morphology of the films was strongly dependent on the concentration of the dopant. Importantly in case of AZO50, the film has a more compact structure consists mainly of closely packed crystallites with a few small voids which exhibited sharper and more well developed edge grains without noticeable interfacial voids. Meanwhile, the distance between grain boundaries increased and the thickness of the films decreased. In contrast, further increase in the dopant content, AZO1, resulted in a progressive damage of the surface where the connectivity between the grains is poor, representing a less crystallized film as revealed by XRD analysis. It consists of bigger grains which are probably formed by coalescence or agglomeration of several small grains, this process of coalescence causes major grain growth but also results in micro-cracks and some large voids that are irregularly shaped and randomly distributed which can be observed in SEM images. Consequently, the observed degradation of the samples compactness can be considered as the main factor causing the observed increase in resistivity of the AZO thin films with aluminium content greater than 0.5%Al (will be discussed in the following sub-sections). Although the observed surface damage, it should be noted that the grain size of the thin films annealed in forming gas are bigger compared with those annealed in vacuum, which agrees with the XRD results. This indicates that RTA could promote grain growth and the coalescence process. An increase in Al concentration in the system showed a change in film microstructure confirmed by the SEM micrographs.

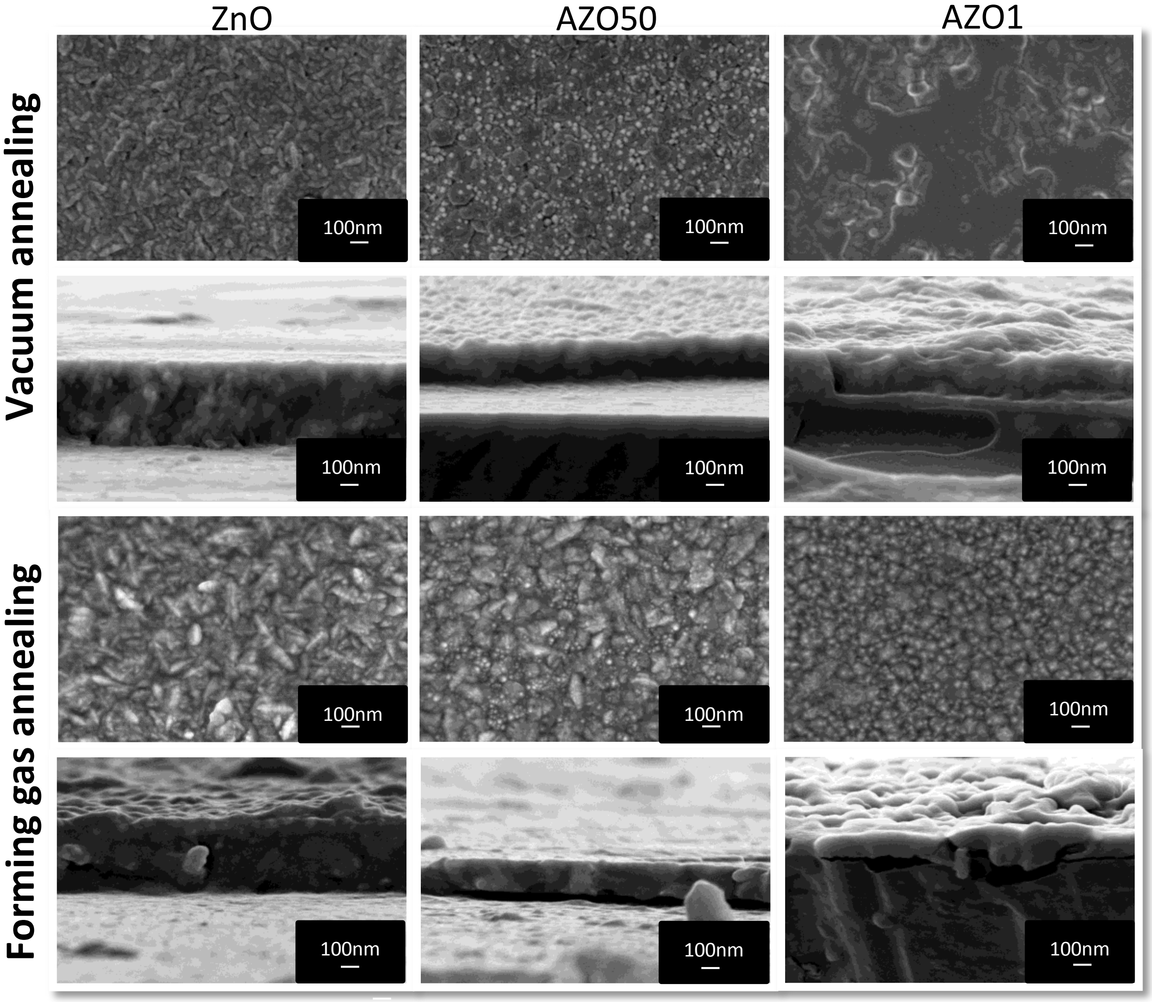

Figure III.23. *Surface morphology and the corresponding cross sectional images of ZnO and AZO films with different Al content annealed in vacuum or forming gas at 350°C.*

III.2.3.2 Structural properties

The crystal structures of the undoped and Al-doped ZnO sprayed films with different dopant concentrations obtained after RTA under forming gas or vacuum ambient at 350°C were investigated by X-ray diffraction which yielded an insight into the crystalline state and crystal orientation. As shown in Figure III.24 (a and b), the deposited films were found to change with Al doping. Almost all of the films exhibited a strong peak at 2θ near 34.43° and weak peaks at 31.43° and 36.26° which could be assigned, respectively, to the (002), (100) and (101), lattice planes of the zinc oxide wurtzite structure (JCPDS No. 01-070-8070), this indicates that the films are polycrystalline and have a strong and dominating preferred orientation along the c-axis perpendicular to the substrate surface. In fact, preferred orientation effects are common in zinc oxide films, and the crystallites tend to pack in the c-direction along the (002) plane, the most energetically stable crystal plane in zinc oxide, which is known to be the result of self-ordering effect caused by the minimization of the crystal surface free energy of each plane as well as by the interaction between the deposit material and the substrate surface. This tendency strongly increases with an increase in cohesive energy of the film to the substrate. Basically, the distribution of grain orientations is affected by all the processes that affect grain size and is also strongly affected by processing techniques and conditions. The grain orientation distribution evolves and can be controlled during film formation and subsequent processing. If surface energy minimization contributes to the driving force for grain boundary motion at the surface of the film, the crystallographic texture of the grains at the surface of the film will evolve as grains with high energy surfaces are eliminated or occluded during thickening [59-62]. Moreover, ordered c-axis orientation of ZnO crystallites perpendicular to the substrate surface is desirable for applications where crystallographic anisotropy is a prerequisite [63]. Also, it is interesting to note that no obvious secondary phases, such as Zn, Al, Al_2O_3, $ZnAl_2O_4$, were detected suggesting that thin films were pure. The plot in Fig.III.24(c) demonstrates that the intensity of the (002) peak increases with the increase of Al content up to 0.5 % and then gradually decreases when exceeding this value which suggest that the crystallinity of the samples was improved obviously with the increase of Al content. The improvement of crystallinity proved that increasing the Al content from (0-0.5) % has a positive effect on the microstructure and crystal quality. When the Al doping is lower (<0.5 at%), with increasing Al doping, the lattice deformation tended to maintain at a certain level. Probably, the reason is that the films allow all the Al atoms substitute the Zn sites with lower free energy and little stresses (No phase corresponding to the dopants is found from the XRD patterns). Conversely, when the Al content is continuously increased over 0.5 %, the intensity of (002) peak decreased markedly. This behavior indicates that an excess increase in the doping concentration deteriorates the crystallinity of films, owing to the Al dopant concentration exceeding the saturation stage and the influence of stresses arising from the difference in ion size between zinc and the dopant.

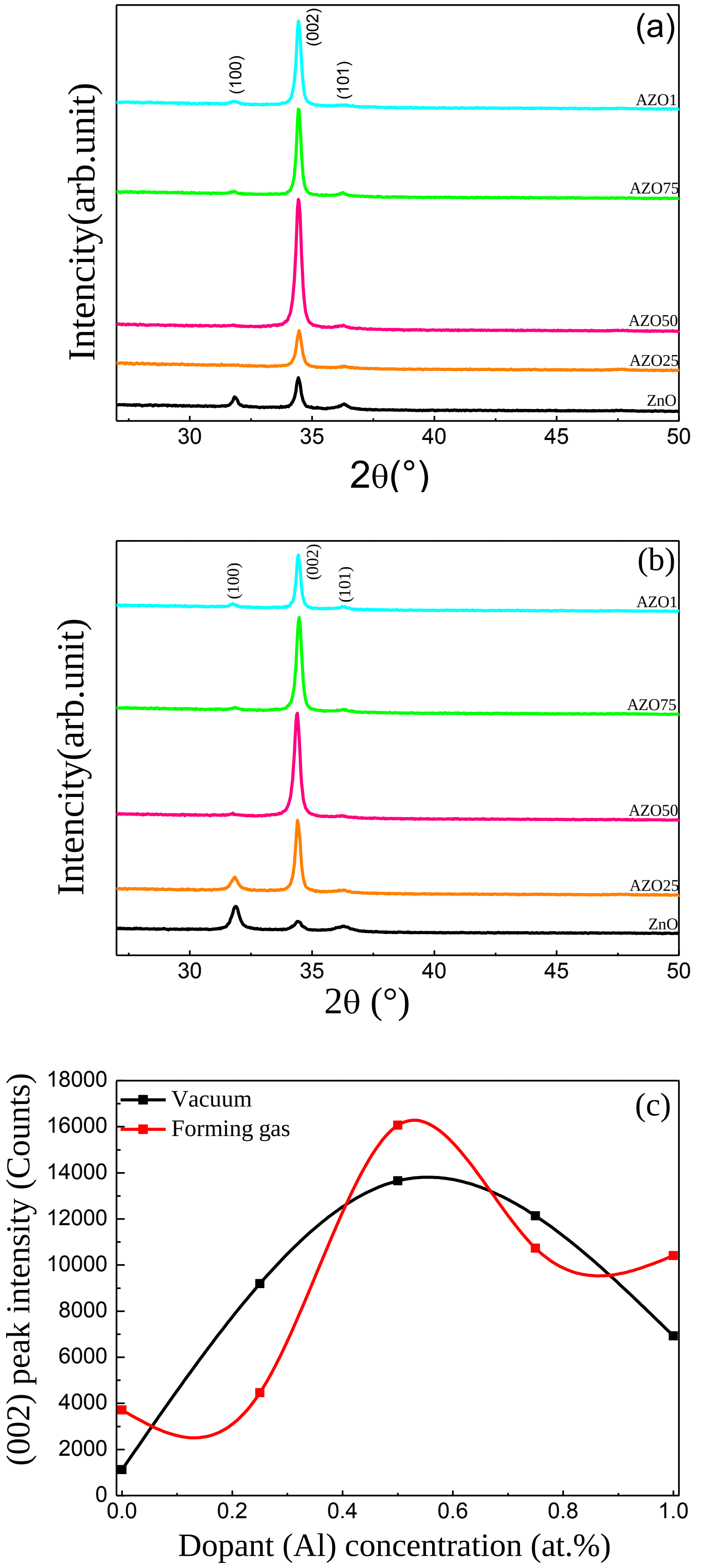

Figure III.24. *XRD patterns of the sprayed samples annealed in a) Forming gas or b) vacuum and c) the (002) peak intensity variation as a function of doping level.*

Most Al atoms do not replace the positions of Zn atoms, they may occupy the interstitial positions and segregates to the non-crystalline region in grain boundaries for high doping concentrations. The increased number of grain boundary defects caused by the excess Al-atoms lead to the severe lattice deformation. Based on these observations, the evolution of XRD patterns suggest that Al^{3+} could dissolve in ZnO crystal lattices uniformly and the structural characteristics change after the saturation of adsorbed and diffused Al^{3+} in the ZnO lattice [64-66].

The average crystallite size calculated using Scherrer's equation was about 31.25 nm for vacuum annealed samples and 33.07 nm in case of forming gas annealed samples. It is observed that upon Al doping the particle size of ZnO reduces significantly and uniformity of particle also gets enhanced as seen from SEM images. This trend has been pointed out [67,33] and is ascribed to the fact that the dopant Al tends to create more nucleation centers during the deposition process resulting thus in small crystallite sizes.

III.2.3.3 Electrical properties

The electrical characterization was carried out in order to evaluate the potential use of the ZnO thin films as TCO. Hall effect measurements were conducted on the formed ZnO and AZO films by using the van der Pauw technique at room temperature to determine the electrical properties of the films as a function of at.% Al and the post deposition rapid thermal anneal under vacuum or forming gas. The dependences of the electrical resistivity (ρ), carrier concentration (n) and Hall mobility (μ) on Al content are illustrated in Fig.III.25.

The electrical properties of these films were found to be very sensitive to the processing conditions. These studies showed that the produced ZnO films were of n-type character. Comparison of the resistivity values with the average resistivity of undoped ZnO in Figure III.25 illustrates that a substantial decrease of several orders of magnitude can be achieved. The extent of the decrease depended on the amount of A1 incorporated and the anneal atmosphere as well with the biggest change observed for the undoped film as might be expected since it had the largest resistivity (1.51 Ω cm). After performing the RTA treatment at 350°C, it was found that the resistivities of ZnO thin films annealed in vacuum or forming gas reduced steadily to 0.94 Ω cm and 0.54 Ω cm, respectively. Interestingly, the pure ZnO also exhibits low resistivity, which is believed to be controlled by intrinsic defects such as zinc interstitials and/or oxygen vacancies which act as n-type donors [68]. It has been postulated that the electronic properties of seemingly undoped zinc oxide films could be due to hydrogen incorporation (or unintentional doping of hydrogen) into the zinc oxide lattice from the precursors but possibly due to the nature of the alcohol used as methanol could well be a source of in situ hydrogen. The mechanism for this is the propensity of hydrogen to bond to oxygen and thus be incorporated into the crystal structure [59]. Obviously, the RTA treatment can effectively increase the crystallinity of the film which leads to a reduction in electrical resistivity.

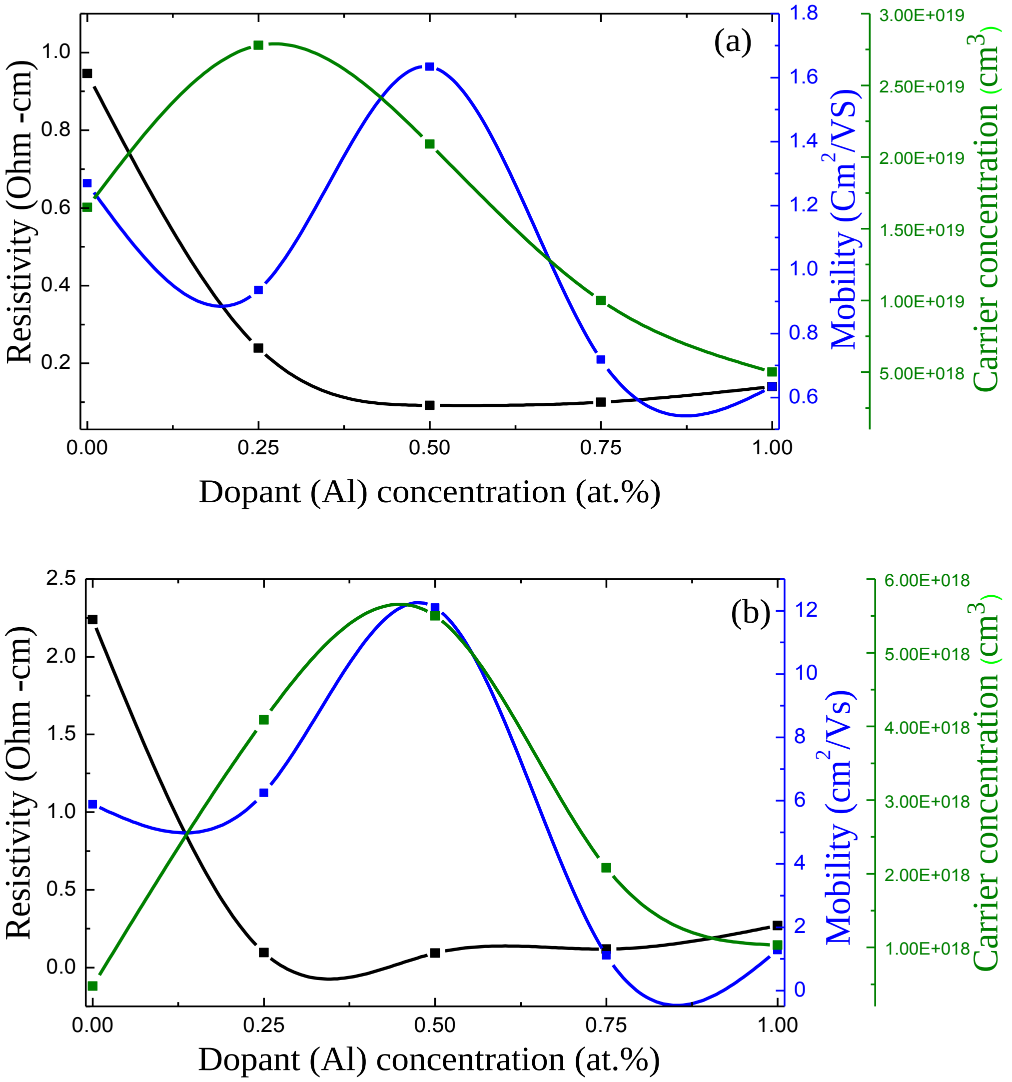

Figure III.25.*The electrical properties dependence on Al concentration of the thin films annealed at 350°C in: a) vacuum and b) forming gas.*

Introducing Aluminium into the zinc oxide structure produced films with a considerable decrease in the resistivity with lowest resistivity value of 0.14 Ω cm and 0.09 Ω cm obtained at an AZO composition of 0.5 at.% Al for vacuum and forming gas annealed films, respectively. Ohyama *et al.* [69] also reported that better electrical and optical properties with strongly c-axis preferred orientation had been obtained in 0.5 at. % aluminium doped ZnO thin films prepared on silica glass substrates via the sol–gel method heated in reducing atmosphere.

In general, the behavior of the resistivity is related both to charge carrier density and Hall mobility. The electrical resistivity of Al-doped ZnO films is inversely proportional to the prevalence of the (002) orientation of film and the increase of grain size, which was influenced by the annealing. It decreased due to the increase in crystallization and orientation of the crystalline structure of the films because the charge carrier mobility is larger with the alignment of the orientation of the crystals. In addition to the effect of orientation, the increase in grain-packing density as shown by SEM micrographs could also contribute to the decrease in resistivity [70]. Thus, highly crystalline films with smoother surface morphology would lead to less carrier scattering, higher mobilities and therefore, improved conductivity [54].

However, an increase in the resistivity at higher dopant concentration, above 0.5 at. % Al, occurred. In fact, Al atoms might produce more educts on grain boundary and separate out Al_2O_3, which would result in the decrease of carrier mobility. Furthermore, the higher doping concentration would lead to smaller crystallite size, which increased the grain boundaries, hence, increased the amount of scattering centers that reduce the carrier mobility and probably offsets the increment in carrier concentration. In addition, increasing the dopant atoms may cause clustering or segregation of dopant species at the grain boundaries which do not contribute free electrons and hence the carrier concentration decreases and consequently the resistivity increases [66,70]. To understand the origin of electrical conduction, defect chemistry should be considered. The defect chemical reaction for the dissolution of Al_2O_3 in ZnO is described as follows:

$$Al_2O_3 \xrightarrow{2ZnO} 2Al_{Zn}^{\bullet} + 2O_0^{\times} + \frac{1}{2}O_{2(g)} + 2e^{'} \qquad \text{(III.4)}$$

The decrease in the resistivity in the case of doped films is due to the increase in carrier concentrations supplied from the substitution of Al, ionized into Al^{3+}, by Zn in the ZnO matrix thus substitution of one Al_2O_3 in ZnO crystal releases two electrons as free carriers. The resistivity of AZO should decrease with the increase in Al dopant concentration before the ionized impurity scattering effect becomes significant. In this case, the conductivity is not governed by a high concentration of intrinsic defects (Zn^+ or Zn^o and associated oxygen vacancies) but by extrinsic donors on substitutional sites (Al^{3+} in Zn^{2+} site) with a higher thermal stability than intrinsic donor type defects. The relative increase of carrier concentration (free electrons, eV) indicates that the aluminium doping atoms are effectively incorporated substitutionally at zinc sites in ZnO lattice [71]. These results corroborate well with the blue shifting of the optical band gap as observed from the $(\alpha\ h\nu)^2$ versus $h\nu$ plot which will be seen next.

On the other hand, the independence of resistivity on the dopant content (at.%Al above 0.5) may be interpreted by the trapping effect of grain boundaries. If oxygen released by dissolution of Al into ZnO is not diffused fast enough into the atmosphere, the oxygen gas will combine with oxygen vacancies and electrons to form oxygen lattice ions. The Al ions located at grain boundaries will become inactive, i.e., no free electrons are released. Also, the formation of Al–O bonds from Al ion and adsorbed oxygen at the grain boundaries will impede the motion of carriers, thereby reducing their mobility. The net defect chemical reactions, which occur at grain boundaries, can be described as:

$$Al_2O_3 + V_0^{\bullet\bullet} \xrightarrow{2ZnO} 2Al_{Zn}^{\bullet} + 3O_0^{\times} \qquad \text{(III.5)}$$

In addition, the segregation of grain boundary defects tends to affect the redistribution of free carriers donated by ionized Al in grains. Sequentially, charged grain boundary built an energy barrier limiting the carrier transport in AZO films [72,73].

As can be seen, the electrical properties of the sprayed thin films were not that conclusive. Rather poorer electrical properties of ZnO:Al films are mainly due to depletion regions formed by the adsorption of negatively charged species on grain boundary surfaces creating a potential barrier and acting as trapping sites for carriers and therefore decreasing free-carrier concentration and Hall mobility [74]. It is believed that removal of depletion regions surfaces and formation of shallow donors contribute to the enhanced films conductivity [75].

Again, another group of samples was annealed under exactly the same aforementioned conditions but this time at a relatively elevated temperature set at 450 °C. Results are displayed in Fig.III.26. Apparently, the trend is analogous in both atmospheres and the resistivity values of the deposited films are visibly lower than those obtained by annealing at 350°C. The greatest change occurred for 0.5 at. % Al films annealed in forming gas with a minimum resistivity value of 0.004 Ω cm. These exhibited high mobility 49.5 $cm^2/(V\ s)$ and charge carriers numbers $1.04 \times 10^{20}\ cm^{-3}$. One can notice that the annealing in forming gas resulted in a very high decrease in resistivity of the films by increasing the carrier concentration and Hall mobility.

Essentially, the different electric transport behavior within a grain and across a boundary of thin film was proposed to result from the different oxygen content between the grain and the boundary. It is known that annealing the sample in a reducing atmosphere at high temperatures would increase the concentration of the oxygen vacancies which have important impacts on the electronic properties of ZnO; the ionization of the oxygen vacancies will create the conducting electrons [76,77]:

$$O_0 \Leftrightarrow V_0 + \frac{1}{2}O_2 \tag{III.6}$$

$$V_0 \Leftrightarrow V_0^{'} + e \tag{III.7}$$

$$V_0^{'} \Leftrightarrow V_0^{''} + e \tag{III.8}$$

It is well established that the vacancies are thermodynamically stable defects, i.e., under certain conditions, a certain number of vacancies exist in the crystal to attain the minimum energy of the system. The equilibrium concentration of the vacancies can be determined according to the thermodynamic calculation:

$$C_0 = \exp(-\Delta E_V / kT + \Delta S_V / k) = A\exp(-\Delta E_V / kT) \tag{III.9}$$

where C_0, T, and ΔE_V are the equilibrium concentration, temperature, and vacancy formation energy, respectively. It can be seen that the decrease in ΔE_V and the increase in T will lead to exponential increase in vacancy equilibrium concentration. Consequently, the higher the annealing temperature, the larger the concentration of oxygen vacancies in AZO films. Obviously, the process of oxygen desorption at the grain boundary includes two steps: desorption of oxygen and the ensuing diffusion of oxygen into atmosphere. Therefore, the density of trap states can be effectively reduced, leading to a better conductivity than that by the first anneal treatment.

Vacuum annealing was carried out to improve the film properties. In general, the popular viewpoint about the effect of vacuum annealing is to increase the concentration of oxygen vacancies and to remove the chemisorbed oxygen on the surface and at the grain boundary which consequently improves the conductivity [78].

Also, to the well-known role of rapid anneal in the activation of Al doping, anneal under N_2H_2 atmosphere allows hydrogen atoms to reduce this potential barrier by oxygen desorption, known as passivation of grain boundary surfaces (passivates the Vo defects to form Vo–H complex), which enhances both carrier concentration and mobility [79]. Thus, when the samples were annealed in vacuum at 450°C it is possible to obtain higher vacancy concentration. As a result, the anneal in reducing atmosphere could produce decreases as well as improvements in distribution in the amount and activity of oxygen reaching the substrate surface.

But, when Al doping goes beyond 0.5 at %, regardless the anneal temperature or atmosphere, the electrical properties declined which is attributed to degradation of crystalline quality by excess aluminium. In other word, at higher doping concentrations, the disorder produced in the lattice increases the efficiency of scattering mechanism such as phonon scattering and ionized impurity scattering which in turn cause an increase in resistivity. In fact, small amounts of aluminium introduce large numbers of free electrons in the doped films, and the conductivity therefore increases. Further increase of Al concentration does not further increase the conductivity. This can be explained by the formation of nonconductive Al oxide from the extra Al atoms and the achievement of equilibrium between the Al atoms contributing conduction electrons and those producing aluminium oxide [80].

Based on the above discussions, the charge carriers in the studied AZO films include free electrons generated by Al doping and oxygen vacancies formed during the post-deposition process. It is deduced that the oxygen desorption after annealing in reducing atmosphere or vacuum helps remove the trapping centers (defects such as grain boundaries, unpassivated regions or scratches/cracks) and releases trapped electrons, resulting in higher electron mobility and concentration.

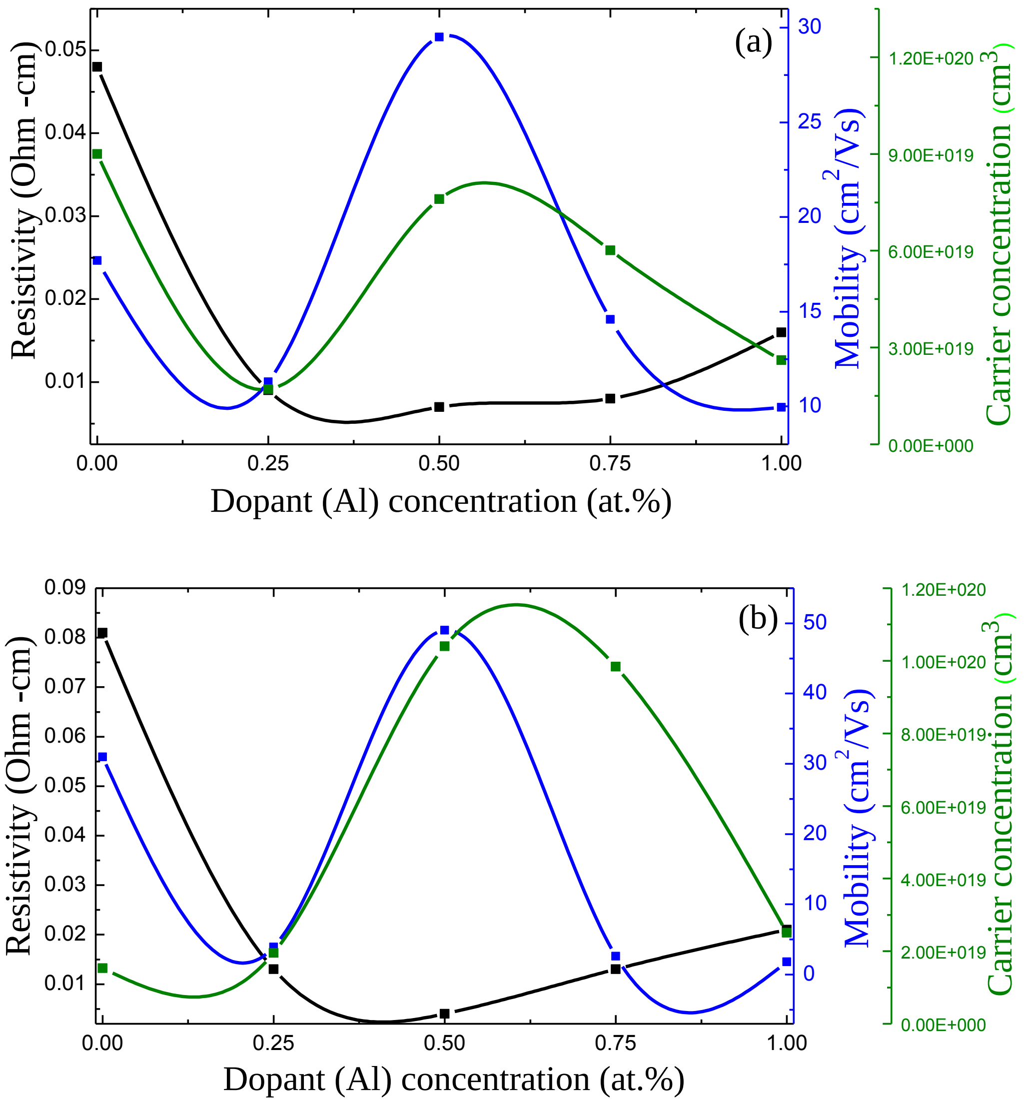

Figure III.26. *The electrical properties dependence on Al concentration of the thin films annealed at 450°C in: a) vacuum and b) forming gas.*

III.2.3.4 Optical properties

The optical transmittance spectra of ZnO and ZnO:Al thin films deposited by ultrasonic spray pyrolysis annealed in vacuum or forming gas at 350 C° for 25 min were measured at room temperature by a double-beam spectrophotometer in the wavelength range of 250–1500 nm and the resulting spectra are presented in Fig.III.27. All the films displayed prominent interference effects caused by the multiple reflections at the three interfaces. Regardless the annealing atmosphere both the undoped ZnO and AZO film shows a transparency of more than 87% across the spectral range 400–700 nm which meets the requirement of the TCO applications.

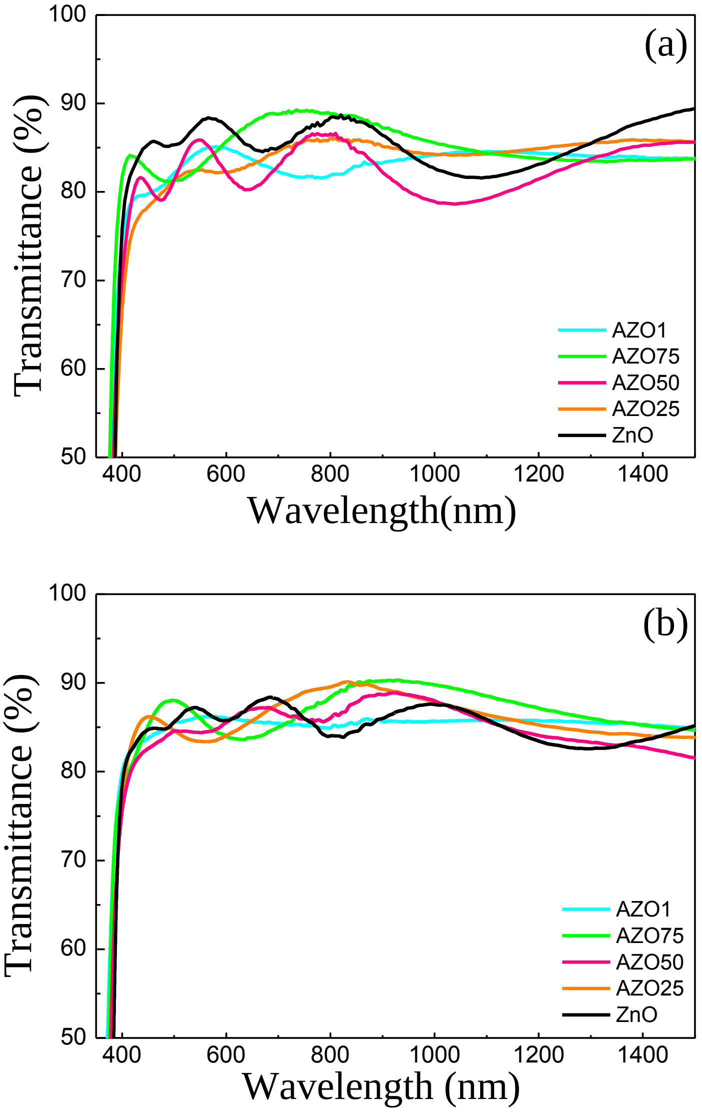

Figure III.27. *Optical transmittance spectra of the sprayed thin films annealed in (a) vacuum and (b) forming gas with various Al doping.*

This enhancement in the optical quality can be attributed to the improvement of the thin film stoichiometry by local rearrangement of the atoms [79]. However, further increasing the dopant concentration did not result in additional improvement of the transmittance and it decreased slightly to ~81% for 1at. %Al. The optical transmittance of a film is known [73] to strongly depend on its surface morphology and density. This change in transmittance by annealing may be mainly attributed to more density or compactness of the film with varying annealing atmosphere.

In the UV light region, it is noteworthy that the short wavelength cut-off in transmittance has also a clear shift towards the short wavelength range i.e. a high energy (blueshift) after doping. The blueshift results from the motion of Fermi level into the conduction band due to an increase in the electron concentration from Al dopant, well known as the BM effect [38], as already mentioned in the last study. These optical properties related to bandgap energy of the ZnO:Al films have good correlation with their electrical properties shown in previous section that demonstrated such an increase of carrier concentration with doping. In general, changes in the gap energy of ZnO thin films have been related to variations in the mean crystallite size, the internal stress and/or the free carrier concentration. It is known that for highly n-doped materials displacement of the band gap energy is mainly due to gap widening effect resulting from an increase of the carrier concentration owing to a blocking of the lowest states of the conduction band by excess electrons [81].

The optical band gap were determined for the thin film by using the Tauc plots of the functional dependence of $(\alpha \times h\nu)^2$ against the photon energy ($h\nu$) depicted in Fig.III.28. In this case variation in the optical band gap occurred depending on the Al concentration. It was observed that the optical band gap of vacuum annealed AZO thin films varied from 3.23 to 3.31 eV, while in case of forming gas annealed samples, it changed from 3.23 to 3.32 eV, for Al doping varying from 0 to 1 at.%, respectively. Similar trend was found previously [80].

It's natural to notice such increase in band gap with increment in at.% Al provided that Al_2O_3 band gap is 8.7 eV. This is in close agreement with the XRD results providing indication that Al^{3+} ions substitutionally occupy the Zn^{2+} sites and perturb the properties of pure ZnO. This effect has been well characterized for AZO films. Since ZnO thin film is naturally n-type, addition of donor Al^{3+} ions raises the Fermi level of AZO films into the conduction band making the films completely degenerate and hence the absorption edge shifts to energies higher than the actual band gap of the material [54, 82]. It can be seen that the value of Eg decreases for 1 at.% Al due to the decrease of carrier density shown in electrical study. The trend in variation of Eg with Al doping was consistent with that observed for the carrier concentration. But when the films were annealed in forming gas, hydrogen in the films may play a role in the extraction of oxygen and cause a large amount of V_O and/or Zn_i defects, which resulted in a slight decrease in average transmittance in the visible region.

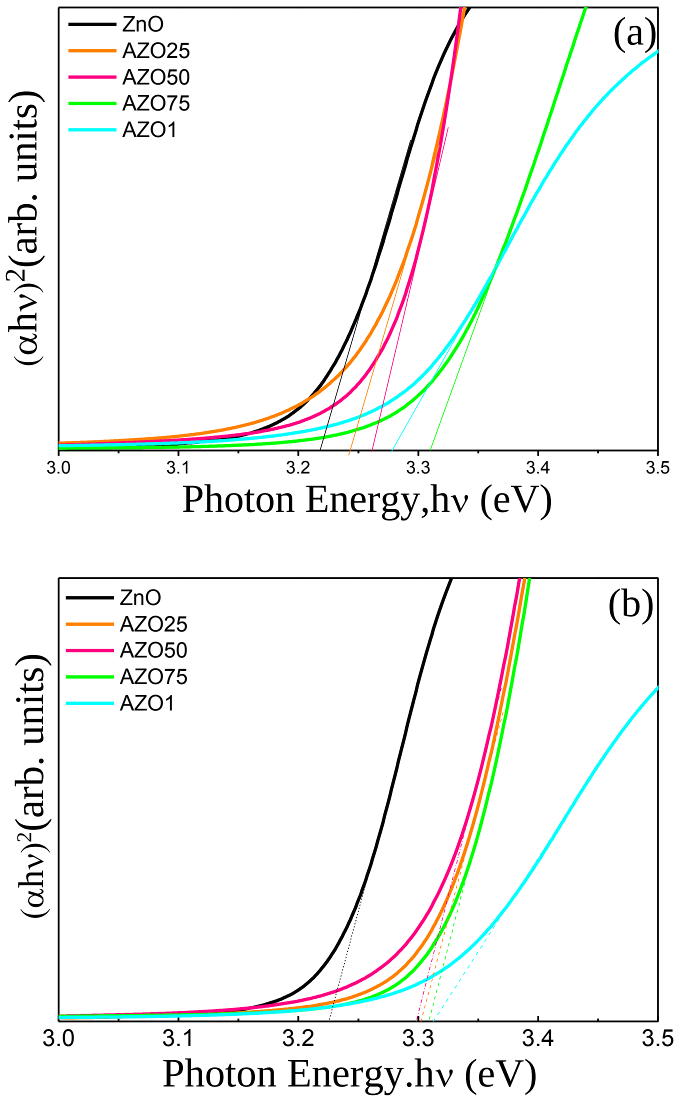

Figure III.28. *Plot of the (αhν)^2 vs. photon energy plot of the doped Al:ZnO film heat treated in a) vacuum and b) forming gas.*

Therefore, value of Eg becomes higher or lower in respect to increased or decreased carrier concentration after annealing due to the BM effect. Lin *et al*. [83] also observed that optical transmission in the visible region decreases substantially for heavily doped ZnO:Al films annealed in reducing atmosphere. These results essentially agree with the analysis results of the shift of the optical absorption edge.

In order to evaluate the transparent conductive properties of AZO films, the figure of merit (ϕ_{TC}) of the films should be examined. The figure of merit provides a useful tool for comparing the performance of transparent conductive coatings when their electrical sheet resistance and optical transmission are known. It can be defined as:

$$\phi_{TC} = T^{10} / R_s \tag{III.10}$$

where T and R_s are the average transmittance in the visible region and sheet resistance, respectively [84]. This is used to predict the transparent electrode properties of a candidate material from its fundamental parameters. The higher FoM indicates that the films possess high transmittance and low resistivity simultaneously. It can be seen that the average transmittance in the visible region was similar but the sheet resistance showed a trend of first decrease then increase with Al doping. According to the definition of ϕ_{TC} above, the value of ϕ_{TC} calculated for the AZO50 films is determined to be 1.3×10^{-2} and 2.1×10^{-2} Ω^{-1} for films annealed in vacuum and forming gas, respectively. As a whole, higher values of ϕ_{TC} could be obtained for the AZO films at Al content of 0.5 at.% as expected since it presents the lowest resistivity values and a good transmittance which makes them potential candidates for TCO applications.

III.2.4 Conclusion

In summary, ZnO and Al-doped ZnO were ultrasonically sprayed on glass substrates whilst varying the operational parameters. This method was shown to be effective and simple for the deposition of highly transparent thin film and allowed for facile incorporation of dopant species at relatively low temperature and short time. Control over the surface morphology, crystallinity, the carrier mobility, charge-carrier density, resistivity and transmission of the films have shown to be highly dependent upon dopant introduction as well as the RTA atmosphere using this technique. The electrical properties were improved, evidenced by a clear decrease in resistivity value due to both doping activation and grain boundary surface passivation and optimum conditions were defined to be 0.5 at.% of Al which exhibited highly crystalline properties and optical transparency of 87% combined with low resistivity. Such properties make AZO well suited for the realization of many optoelectronic applications including transparent conductive oxides in display devices and solar cells.

Because the development of a more environmentally friendly low-temperature process is required for the film growth on a heat-sensitive substrate, such as those (e.g. plastics, paper, fabrics) envisaged for flexible solar cell platforms or other bendable electronic applications, more effort to reduce substrate temperature and to control the RTA time and/or temperature will be necessary for future studies.

III.3 References

[1] L. Wang, M. Muhammed, Synthesis of zinc oxide nanoparticles with controlled morphology. *J. Mater. Chem*. 9(11) (1999) 2871-2878.

[2] S. Marouf, A. Beniaiche, H. Guessas, A. Azizi, Morphological, Structural and Optical Properties of ZnO Thin Films Deposited by Dip Coating Method. *Mater. Res*. Ahead of print, (2016).

[3] E. Hosono, S. Fujihara, T. Kimura, H. Imai, Non-Basic Solution Routes to Prepare ZnO Nanoparticles. *J. Sol-Gel Sci. Technol.* 29(2) (2004)71-79.

[4] S. Rani, P. Suri, P. K. Shishodia, R. M. Mehra, Synthesis of nanocrystalline ZnO powder via sol–gel route for dye-sensitized solar cells. *Sol. Energ. Mat. Sol. Cells.* 92 (12) (2008)1639-1645.

[5] E. Hosono, S. Fujihara, T. Kimura, H. Imai. Growth of layered basic zinc acetate in methanolic solutions and its pyrolytic transformation into porous zinc oxide films. *J. Colloid Interface Sci*. 272(2) (2004) 391-398.

[6] C. Y. Chee, K. Nadarajah, M. K. Siddiqui, Y. Wong, Optical and structural characterization of solution processed zinc oxide nanorods via hydrothermal method. *Ceram. Int.* 40(7) (2014) 9997-10004.

[7] A. K. K. Kyaw, X. W. Sun, C. Y. Jiang, G. Q. Lo, D. W. Zhao, D. L. Kwong, An inverted organic solar cell employing a sol-gel derived ZnO electron selective layer and thermal evaporated MoO_3 hole selective layer. *Appl. Phys. Lett.* 93(22) (2008) 221107.

[8] L. Xu, G. Zheng, J. Miao, F. Xian, Dependence of structural and optical properties of sol–gel derived ZnO thin films on sol concentration. *Appl. Surf. Sci.* 258(19) (2012) 7760-7765.

[9] K. Thongsuriwong, P. Amornpitoksuk, S. Suwanboon, Structure, morphology, photocatalytic and antibacterial activities of ZnO thin films prepared by sol–gel dip-coating method. *Adv. Powder Technol.* 24(1) (2013) 275-280.

[10] Y. Li, L. Xu, Li. X, X. Shen, A. Wang, Effect of aging time of ZnO sol on the structural and optical properties of ZnO thin films prepared by sol–gel method. *Appl. Surf. Sci*. 256(14) (2010) 4543-4547.

[11] V. Fathollahi, M. M. Amini. Sol–gel preparation of highly oriented gallium-doped zinc oxide thin films. *Mater. Lett*. 50(4) (2001) 235-239.

[12] N. Singh, Dhruvashi, D. Kaur, R. M. Mehra, A. Kapoor, Effect of Ageing in Structural Properties of ZnO Nanoparticles with pH Variation for Application in Solar Cells. *Open. Renew. Energ. J*. 5 (2012) 15-18.

[13] N. B. Ibrahim, S. M. Al-Shomar, S. H. Ahmad. Effect of aging time on the optical, structural and photoluminescence properties of nanocrystalline ZnO films prepared by a sol–gel method. *Appl. Surf. Sci*. 283 (2013) 599-602.

[14] C. J. Brinker, G. W. Scherer, *Sol-gel science; the physics and chemistry of sol-gel processing*. Cambridge: Academic Press; 1990.

[15] L. L. Hench, J. K. West, The sol-gel process. *Chem. Rev*. 90(1) (1990) 33-72.

[16] Scherer, G. W, Structure and properties of gels. *Cement Concrete Res*. 29(8) (1999) 1149-1157.

[17] J. D. Wright, N. A. Sommerdijk, *Sol-Gel Materials: Chemistry and Applications*. (Vol.4). Amsterdam: Gordon and Breach Science, (2000).

[18] A. M. Peiró, P. Ravirajan, K. Govender, D. S. Boyle, P. O'Brien, D. D. Bradley, J. Nelson, J. R. Durrant, Hybrid polymer/metal oxide solar cells based on ZnO columnar structures. *J. Mater. Chem*.16 (2006) 2088–2096.

[19]J. Rodriguez-Baez, A. Maldonado, G. Torres-Delgado, R. Castanedo-Pérez, M. D. L. L. Olvera, Influence of the molar concentration and substrate temperature on fluorine-doped zinc oxide thin films chemically sprayed. *Mater. Lett*. 60(13) (2006) 1594-1598.

[20] N. Goswami, D. K. Sharma, Structural and optical properties of unannealed and annealed ZnO nanoparticles prepared by a chemical precipitation technique. *Physica E Low Dimens. Syst. Nanostruct.* 42(5) (2010) 1675-1682.

[21] S. O'Brien, L. H. K. Koh, G. M. Crean, ZnO thin films prepared by a single step sol–gel process. *Thin Solid Films* 516(7) (2008)1391-1395.

[22] S.A. Kamaruddin, K.Y. Chan, H.K. Yow, M.Z. Sahdan, H. Saim, D. Knipp, Zinc oxide films prepared by sol–gel spin coating technique. *Appl. Phys. A Mater. Sci. Process.*104 (1) (2011) 263-268.

[23] M. Baneto, A. Enesca, Y. Lare, K. Jondo, K. Napo, A. Duta, Effect of precursor concentration on structural, morphological and opto-electric properties of ZnO thin films prepared by spray pyrolysis, *Ceram. Int.* 40 (6) (2014) 8397–8404.

[24] L. Mentar, O. Baka, M. R. Khelladi, A. Azizi, S. Velumani, G. Schmerber, A. Dinia, *J Mater Sci: Mater Electron* 26 (2015) 1217–1224.

[25] L. Lu, R. Li, T. Peng, K. Fan, K. Dai, Effects of rare earth ion modifications on the photoelectrochemical properties of ZnO-based dye-sensitized solar cells. *Renew. Energ.* 36(12) (2011) 3386-3393.

[26] L. Armelao, F. Heigl, A. Jürgensen, R. I. R. Blyth, T. Regier, X. T. Zhou, T. K. Sham, X-ray excited optical luminescence studies of ZnO and Eu-doped ZnO nanostructures. *J. Phys. Chem. C* 111(28) (2007)10194-10200.

[27] M. Subramanian, P. Thakur, S. Gautam, K. H. Chae, M. Tanemura, T. Hihara, S. Vijayalakshmi, T. Soga, S. S. Kim, K. Asokan, R. Jayavel, Investigations on the structural, optical and electronic properties of Nd doped ZnO thin films. *J. Phys. D: Appl. Phys.* 42 (10) (2009) 105410.

[28] F. Xian, X. Li, Effect of Nd doping level on optical and structural properties of ZnO: Nd thin films synthesized by the sol–gel route. *Opt. Laser Technol.* 45 (2013) 508-512.

[29] G. Gottardi, R. Pandiyan, V. Micheli, G. Pepponi, S. Gennaro, R. Bartali, N. Laidani, Effect of Nd^{3+} incorporation on the microstructure and chemical structure of RF sputtered ZnO thin films. *Mater. Sci. Eng. B* 178 (9) (2013) 609-616.

[30] M. H. Wang, Z. Y. Zhao, T. T. Liu, Synthesis of Pr-doped ZnO nanoparticles by sol–gel method and varistor properties study. *J. Alloys Compd.* 621(2015) 220-224.

[31] D. Xu, K. He, R. H. Yu, Y. Tong, J. P. Qi, X. J. Sun, Y. T. Yang, H. X. Xu, H. M. Yuan, J. Ma, Microstructure and electrical properties of praseodymium oxide doped Bi2O3 based ZnO varistor films. *Mater. Technol.* 30 (2015) A24-A28.

[32] M. Balestrieri, M. Gallart, M. Ziegler, P. Bazylewski, G. Ferblantier, G. Schmerber, G. S. Chang, P. Gilliot, D. Muller, A. Slaoui, S. Colis, A. Dinia, Luminescent Properties and Energy Transfer in Pr^{3+} Doped and Pr^{3+}-Yb^{3+} Co-doped ZnO Thin Films. *J. Phys. Chem. C* 118 (25) (2014)13775-13780.

[33] R. B. H. Tahar, Structural and electrical properties of aluminum-doped zinc oxide films prepared by sol–gel process. *J. Eur. Ceram. Soc.* 25(14) (2005) 3301-3306.

[34] D. Wang, G. Xing, M. Gao, L. Yang, J. Yang, T. Wu, Defects-mediated energy transfer in red-light-emitting Eu-doped ZnO nanowire arrays. *J. Phys. Chem. C* 115 (46) (2011) 22729-22735.

[35] R. S. Sreedharan, R. Vinodkumar, I. Navas, R. Prabhu, V. M. Pillai, Influence of Pr Doping on the Structural, Morphological, Optical, Luminescent and Non-linear Optical Properties of RF-Sputtered ZnO Films. *J.O.M.* 68(1) (2016) 341-350.

[36] G. L. Kabongo, G. H. Mhlongo, T. Malwela, B. M. Mothudi, K. T. Hillie, M. S. Dhlamini, Microstructural and photoluminescence properties of sol–gel derived Tb 3+ doped ZnO nanocrystals. *J. Alloys Compd. 591* (2014)156-163.

[37] S. Sharma, R. Vyas, N. Sharma, V. Singh, A. Singh, V. Kataria, B. K. Gupta, Y.K. Vijay, Highly efficient green light harvesting from Mg doped ZnO nanoparticles: Structural and optical studies, *J. Alloys Compd*. 552 (2013) 208‑212.

[38] E. Burstein, Phys. Rev. 93 (1954) 632.

[39] A. B. Djurišić, A. M. C. Ng, X. Y. Chen, ZnO nanostructures for optoelectronics: material properties and device applications. *Prog. Quant. Electron.* 34(4) (2010)191-259.

[40] A. Mahroug, S. Boudjadar, S. Hamrit, L. Guerbous, Structural, optical and photocurrent properties of undoped and Al-doped ZnO thin films deposited by sol–gel spin coating technique, *Mater. Lett.* 134 (2014) 248–251.

[41] A. Layek, S. Banerjee, B. Manna, A. Chowdhury, Synthesis of rare-earth doped ZnO nanorods and their defect–dopant correlated enhanced visible-orange luminescence. *RSC Adv.* 6(42) (2016) 35892-35900.

[42] F. Gu, S. F. Wang, M. K. Lü, G. J. Zhou, D. Xu, D. R. Yuan, Structure evaluation and highly enhanced luminescence of Dy^{3+}-doped ZnO nanocrystals by Li^{+} doping via combustion method. *Langmuir* 20(9) (2004) 3528-3531.

[43] J. L. Zhao, X. M. Li, S. Zhang, C. Yang, X. D. Gao, W. D. Yu, Highly (002)-oriented ZnO film grown by ultrasonic spray pyrolysis on ZnO-seeded Si (100) substrate. *J. mater. res.* 21(09) (2006) 2185-2190.

[44] E. Matei, M. Enculescu, I. Enculescu, Single bath electrodeposition of samarium oxide/zinc oxide nanostructured films with intense, broad luminescence. *Electrochim. Acta* 95 (2013)170-178.

[45] S. Xu, Z. L. Wang, One-dimensional ZnO nanostructures: solution growth and functional properties. *Nano Res.* 4(11) (2011)1013-1098.

[46] D. Behera, B. S. Acharya, Nano-star formation in Al-doped ZnO thin film deposited by dip-dry method and its characterization using atomic force microscopy, electron probe microscopy, photoluminescence and laser Raman spectroscopy. *J. lumin.* 128 (10) (2008) 1577-1586.

[47] P. Ilanchezhiyan, G. M. Kumar, M. Subramanian, R. Jayavel, Effect of Pr doping on the structural and optical properties of ZnO nanorods. *Mater. Sci. Eng. B* 175(3) (2010) 238-242.

[48] T. Pauporte, F. Pelle, B. Viana, P. Aschehoug, Luminescence of nanostructured Eu^{3+}/ZnO mixed films prepared by electrodeposition. *J. Phys. Chem. C* 111(42) (2007) 15427-15432.

[49] D. Wang, Q. Chen, G. Xing, J. Yi, S. Rahman Bakaul, J. Ding, J. Wang, T. Wu, Robust room-temperature ferromagnetism with giant anisotropy in Nd-doped ZnO nanowire arrays. *Nano let.* 12 (8) (2012) 3994-4000.

[50] A. Lyubchyk, A. Vicente, P. U. Alves, B. Catela, B. Soule, T. Mateus, M. J. Mendes, H. Águas, E. Fortunato, R. Martins, Influence of post-deposition annealing on electrical and optical properties of ZnO-based TCOs deposited at room temperature, *Phys. Status Solidi A* 213 (2016) 2317–2328.

[51] A. Lyubchyk, A. Vicente, B. Soule, P. U. Alves, T. Mateus, M. J. Mendes, H. Águas, E. Fortunato, R. Martins, Mapping the electrical properties of ZnO-based transparent conductive oxides grown at room temperature and improved by controlled postdeposition annealing, *Adv. Electron. Mater.* 2 (2016) 1500287.

[52] Y. Wang, X. Zhang, Q. Huang, C. Wei, Y. Zhao, Room temperature deposition of highly conductive and transparent hydrogen and tungsten co-doped ZnO films for thin film solar cells applications, Sol. Energ. Mat. Sol. Cells 110 (2013) 94–97.

[53] P. K. Nayak, J. Yang, J. Kim, S. Chung, J. Jeong, C. Lee, Y. Hong, Spin-coated Ga-doped ZnO transparent conducting thin films for organic light-emitting diodes, *J. Phys. D: Appl. Phys.* 42 (2009) 035102.

[54] P. Banerjee, W. J. Lee, K. R. Bae, S. B. Lee, G. W. Rubloff, Structural, electrical, and optical properties of atomic layer deposition Al-doped ZnO films, *J. Appl. Phys.* 108 (2010) 043504.

[55] H. Tong, Z. Deng, Z. Liu, C. Huang, J. Huang, H. Lan, C. Wang, Y. Cao, Effects of post-annealing on structural, optical and electrical properties of Al-doped ZnO thin films, *Appl. Surf. Sci.* 257 (2011) 4906–4911.

[56] H. Águas, T. Mateus, A. Vicente, D. Gaspar, M. J. Mendes, W. A. Schmidt, L. Pereira, E. Fortunato, R. Martins, Thin film silicon photovoltaic cells on paper for flexible indoor applications. *Adv. Funct. Mater. 25*(23) (2015) 3592-3598.

[57]S. Marouf, A. Beniaiche, K. Kardarian, M. J. Mendes, O. Sanchez-Sobrado, H. Águas, E. Fortunato, R. Martins, Low-Temperature Spray-coating of high-performing ZnO:Al films for transparent electronics, Manuscript under consideration for publication,(2017),

[58] E. Arca, K. Fleischer, I. V. Shvets, *J. Phys. Chem. C* 113 (2009) 21074–21081.

[59] D. S. Bhachu, G. Sankar, I.P. Parkin, Aerosol assisted chemical vapor deposition of transparent conductive zinc oxide films, *Chem. Mater.* 24 (2012) 4704–4710.

[60] C. V. Thompson, *Annu. Rev. Mater. Sci.* 30 (2000) 159–90.

[61] Bailin Zhu, Kun Lü, Jun Wang, Taotao Li, Jun Wu, Dawen Zeng, Changsheng Xie, *J. Vac. Sci. Technol. A* 31 (6) 061513 (2013).

[62] X. Jiang, C. L. Jia, B. Szyszka, *Appl. Phys. Lett.* 80 (2002) 3090.

[63] Nicola R. S. Farley, Christopher R. Staddon, Lixia Zhao, Kevin W. Edmonds, Bryan L. Gallagher, Duncan H. Gregory, *J. Mater. Chem.* 14 (2004) 1087-1092.

[64] Z. Lu, J. Zhou, A. Wang, N. Wang, X. Yang, Synthesis of aluminium-doped ZnO nanocrystals with controllable morphology and enhanced electrical conductivity, *J. Mater. Chem.* 21 (2011) 4161–4167.

[65] Shou-Yi Kuo, Wei-Chun Chen, Fang-I Lai, Chin-Pao Cheng, Hao-Chung Kuo, Shing-Chung Wang, Wen-Feng Hsieh, *J. Cryst. Growth.* 287 (2006) 78–84.

[66] Hua Wang, Mu-hui Xu, Ji-wen Xu, Ming-fang Ren, Ling Yang, *J Mater Sci: Mater Electron* 21 (2010) 589–594.

[67] S. S. Badadhe, I. S. Mulla, Effect of aluminium doping on structural and gas sensing properties of zinc oxide thin films deposited by spray pyrolysis. *Sens. Actuator B-Chem.* 156(2) (2011) 943-948.

[68] P. K. Nayak, J. Yang, J. Kim, S. Chung, J. Jeong, C. Lee, Y. Hong, Spin-coated Ga-doped ZnO transparent conducting thin films for organic light-emitting diodes, *J. Phys. D: Appl. Phys.* 42 (2009) 035102.

[69] M. Ohyama, H. Kozuka, T. Yoko, Sol–gel preparation of transparent and conductive aluminum-doped zinc oxide films with highly preferential crystal orientation. *J. Am. Ceram. Soc.* 81(1998) 1622-1632.

[70] V. Musat, B. Teixeira, E. Fortunato, R.C.C. Monteiro, *Thin Solid Films* 502 (2006) 219 – 222.

[71] N. Jabena Begum, R. Mohan, K. Ravichandran, *Superlattice Microst*. 53 (2013) 89–98.

[72] J. P. Lin, J. M. Wu, The effect of annealing processes on electronic properties of sol-gel derived Al-doped ZnO films, Appl. Phys. Lett. 92 (2008)134103.

[73] W. Yang, Z. Wu, Z. Liu, A. Pang, Y. L. Tu, Z. C. Feng, Room temperature deposition of Al-doped ZnO films on quartz substrates by radio-frequency magnetron sputtering and effects of thermal annealing, *Thin Solid Films* 519 (2010) 31–36.

[74] B. Y. Oh, M. C. Jeong, D. S. Kim, W. Lee, J. M. Myoung, Post-annealing of Al-doped ZnO films in hydrogen atmosphere, *J. Cryst. Growth.* 281 (2005) 475–480.

[75] H. P. Chang, F. H. Wang, J. C. Chao, C. C. Huang, H. W. Liu, Effects of thickness and annealing on the properties of Ti-doped ZnO films by radio frequency magnetron sputtering, *Curr. Appl. Phys*. 11 (2011) S185-S190.

[76] C. C. Wang, L. W. Zhang, Oxygen-vacancy-related dielectric anomaly in $CaCu_3Ti_4O_{12}$: post-sintering annealing studies. *Phys. Rev. B* 74 (2006) 024106.

[77] J. Wang, Z. Wang, B. Huang, Y. Ma, Y. Liu, X. Qin, X. Zhang, Y. Dai, Oxygen vacancy induced band-gap narrowing and enhanced visible light photocatalytic activity of ZnO, *ACS Appl. Mater. Inter.* 4 (2012) 4024−4030.

[78] M. Zhu, H. Huang, J. Gong, C. Sun, X. Jiang, Role of oxygen desorption during vacuum annealing in the improvement of electrical properties of aluminum doped zinc oxide films synthesized by sol gel method, *J. Appl. Phys.* 102 (2007) 043106.

[79] B. Ayachi, T. Aviles, J. P. Vilcot, C. Sion, *Appl. Surf. Sci*. 366 (2016) 53–58.

[80] J. Benny, P.K. Manoj, V.K. Vaidyan, *Ceram. Int.* 32 (2006) 487–493.

[81] C. Guillén, J. Herrero, *Vacuum* 84 (2010) 924–929.

[82] M. C. Jun, S. U. Park, J. H. Koh, Comparative studies of Al-doped ZnO and Ga-doped ZnO transparent conducting oxide thin films, *Nanoscale Res. Lett.* 7 (2012)1–6.

[83] S. S. Lin, J. L. Huang, P. Šajgalik, The properties of heavily Al-doped ZnO films before and after annealing in the different atmosphere, *Surf. Coat. Tech.* 185 (2004) 254– 263.

[84] G. Haacke, *J. Appl. Phys.* 47(1976) 4086.

General conclusions

In this research work two groups of ZnO thin films doped with trace amounts of rare earth (RE) or Al were produced by sol gel dip coating and ultrasonic spray pyrolysis, respectively. Main aim herein was the fabrication of very low cost and eco-friendly thin films that may be suitable for solar cells or flat panel displays using easily available materials.

Our results show that the different ZnO nanostructure properties are very sensitive to growth conditions. We reported, firstly, an experimental study on the synthesis and characterization of nanostructured undoped ZnO thin films via sol–gel dip coating method on glass substrates. The crystalline structure, surface morphologies and optical transmittance of the sol–gel derived ZnO thin films depended greatly on Zn^{2+} molarities and sol aging time. Interestingly, sol concentration of 0.1 M aged for 72-168 h was found to be optimal to achieve smooth surface morphology, good crystallinity and optical transmittance which were attributed to an ideal stability of solution. These observations provided useful guidelines for the process control purposes and demonstrated that the selection of the sol concentration and aging time are key factors for obtaining good quality ZnO thin film via the solution route. These optimized conditions were then used for further studies on the preparation of RE doped ZnO thin films.

It was found that a proper amount of RE dopant is significantly crucial for obtaining a high degree of densification. The structural and morphological investigations showed that the transmittance and photoluminescence emission enhanced with the increment of RE dopants in the ZnO matrix. To achieve effective light emission in doped ZnO, it can also be envisaged, that an appropriate energy transfer process is established and a high percentage of the engineered defects can effectively participate in this process. This suggests that rare-earth-doped ZnO thin films are promising and have the potential to give efficient multicolor emissions that may find applications in optoelectronic and display devices. Therefore, the sol–gel dip coating method was proved to be well adapted to the elaboration of thin films for photonic applications and suitable for cost-effective fabrication studies in areas of oxide research.

Secondly, ZnO and Al-doped ZnO were ultrasonically sprayed on glass substrates whilst varying the operational parameters. This method was shown to be effective and simple for the deposition of highly transparent and less resistive thin film and allowed for facile incorporation of dopant species at relatively low temperature and short time. Such properties make the developed spray-deposited AZO well suited for the realization of many optoelectronic applications including transparent conductive oxides in display devices and solar cells. The findings also open the way for future studies aimed at developing environmentally friendly low-temperature processes compatible with heat-sensitive substrates envisaged for flexible solar cell platforms or other bendable electronic applications.

I hope this text is helpful to you, the reader, after all, that is the aim of this work.

Résumé

Au cours de la dernière décennie, des progrès profonds ont été réalisés dans le domaine des nanotechnologies. Ceci a motivé le développement des nanomatériaux et des différentes techniques de leur élaboration. Les couches minces nanostructurées d'oxyde métalliques, continuent à susciter une attention considérable du point de vue fondamental et application, principalement en raison de leurs propriétés très exploitées. Une considération particulière a été portée sur l'oxyde de zinc qui est un semi-conducteur de type n possédant d'excellentes propriétés qui lui confèrent la possibilité d'être exploité dans de nombreux domaines intéressant et pertinent tel que l'optoélectronique.

C'est dans cette direction que s'inscrit ce travail de thèse qui consiste à élaborer et caractériser des films d'oxyde de zinc pures et dopées dans le but d'améliorer les propriétés structurales, optiques et électriques de ZnO. Les couches minces ont été déposées sur verre par voie chimique.

Les caractérisations effectuées sur les couches dopées Nd et Pr révèlent que ces dopants modifient les propriétés optiques du ZnO en augmentant le gap optique et améliorant la transmittance et la photoluminescence ce qui peut être utile pour la technologie d'affichage.

La caractérisation des couches minces de ZnO dopées Al a montré que le dopage par Al affecte les propriétés structurales, morphologiques et électriques du ZnO. Al s'avère donc prometteur en raison que les couches minces obtenues ont une bonne transmittance couplée à une faible résistivité ce qui est très intéressant pour l'optoélectronique. En particulier, nous avons démontré la possibilité de déposer des films de AZO a basse température ce qui est convenable pour les substrats sensibles aux hautes températures tels que ceux envisagés aux cellules solaires et les produits électroniques flexibles.

Abstract

Over the last decade, profound progress has been made in the field of nanotechnology. This has motivated the development of nanomaterials and the different techniques of their elaboration. The nanostructured thin films of metal oxide continue to receive considerable attention from both fundamental point of view and application, mainly because of their highly exploited properties. Of particular interest is zinc oxide an n type semiconductor that exhibits excellent properties which makes it useful in many interesting and relevant fields such as optoelectronics.

Consequently, the present work consists of the synthesis and the characterization of pure and doped ZnO thin films in order to improve its structural, optical and electrical properties. The films were deposited on glass substrates by wet chemical methods.

The characterizations of Nd and Pr doped ZnO thin films shows that these dopants are able to modify optical properties of ZnO films by increasing the band gap and enhancing the transmittance and photoluminescence intensity which makes this film suitable for instance to be used in displays technology.

The characterization of Al doped ZnO thin films showed that doping with Al affects the structural, morphological and electrical properties of ZnO. Al is thus promising dopant since the films present high optical transmittance combined with low resistivity which constitutes an interesting alternative for optoelectronic applications. In particular we demonstrated the possibility of depositing Al doped ZnO thin films at low temperature which is compatible with heat-sensitive substrates, such as those envisaged for flexible solar cell or other bendable electronic applications.